All-Optical Cs Magnetometry System for a Neutron Electric Dipole Moment Experiment

by

Wolfgang Klassen

A thesis submitted to the Faculty of Graduate Studies of
The University of Manitoba
in partial fulfillment of the requirements of the degree of

MASTER OF SCIENCE

Department of Physics and Astronomy
University of Manitoba
Winnipeg

Abstract

High-precision low-energy experiments are one of the best ways we have of probing physics beyond the standard model (BSM). One BSM prediction is a small but non-zero electric dipole moment for the neutron (nEDM). This quantity means that the neutron breaks a fundamental symmetry of nature, the symmetry between particles and their anti-particles. This symmetry is known as Charge-Parity (CP) symmetry, and finding a new system that violates it could help explain (among other things) the matter-antimatter asymmetry in the early universe.

The electric dipole moment (EDM) of any particle is very sensitive to electric and magnetic fields. In order to measure the neutron EDM (nEDM) to our desired precision, the magnetic field present in the experiment must be known with a statistical precision of 10 fT over the nEDM measurement period (one Ramsey cycle). In addition, any gradients up to a third order polynomial field expansion must also be identified, as they contribute to systematic uncertainty.

I develop the theoretical framework describing magnetic fields in the TRIUMF Ultra Cold Advanced Neutron (TUCAN) nEDM experiment, prescribe a method by which scalar field measurements can be used to extract systematic magnetic field dependant effects, and build a proof of concept optical magnetometer meeting the above requirements.

Thesis Supervisor: Jeffery W. Martin
Title: Professor

Thesis Supervisor: Russell Mammei
Title: Assistant Professor

Acknowledgments

Thanks to my parents, who gave me a love of science and curiosity, and taught me that I could make anything I wanted to with enough hot glue and cardboard. Thanks to Lillian, who has patiently waited for this dang thing to be done. Thanks to professor Martin for giving me a job as an undergrad, that turned out OK I guess. He has been a constant inspiration to become a better scientist, and this thesis could not have happened without his guidance. Thanks to professor Mammei for being endlessly optimistic and encouraging, and for being as excited as I am with just about everything. Thanks to Dave Ostapchuk, the lab tech without whom the UofW labs would not be the fantastic work environment they are. Thanks to professor Chris Bidinosti for his help with the spherical harmonic functions. Thanks to professor Jason Fiege for providing his nQube software and support for it. Thanks to Moushumi, Mike, Maedeh, Shomi, Sean, and any other students that I have worked with for being amazing colleagues, and for helping me out in the lab when I needed. Thanks to the admin staff at both the UofM and the UofW for helping me deal with the most stressful and confusing part of academia: paperwork.

Contents

List of Figures

List of Tables

Glossary

B magnetic field magnitude. 4

E electric field magnitude. 4

$G_{l,m}$ gradient coefficients, labelled by ℓ, m just as the spherical harmonics. 12

H height of an nEDM precession chamber. 14

I_0 total intensity of probe beam. 56

I_x intensity of x linearly polarized light in probe beam. 56

I_y intensity of y linearly polarized light in probe beam. 56

R radius of an nEDM precession chamber. 14

T_x transformation matrix between position and field space in x field polynomials. 12

T_y transformation matrix between position and field space in y field polynomials. 12

T_z transformation matrix between position and field space in z field polynomials. 12

T_{Ramsey} duration of a single Ramsey cycle. 5

Φ magnetic scalar potential. 10

$\Phi_{l,m}$ basis of polynomials for the magnetic scalar potential. 11

$\Pi_{\hat{e_i},l,m}$ basis of polynomials for the magnetic field in the $\hat{e_i}$ direction. 11

$\vec{B_0}$ vector of measurements of the true field in the nEDM experiment. 13

$\vec{B_x}$ list of magnetic field measurements in the x direction. 12

$\vec{B_y}$ list of magnetic field measurements in the y direction. 12

$\vec{B_z}$ list of magnetic field measurements in the z direction. 12

$\vec{J_f}$ free current. 10

$\vec{g}$ tuple of gradient terms. 12

γ gyromagnetic ratio. 14

γ_{Hg} gyromagnetic ratio of mercury. 14

$\hbar$ reduced Planck's constant. 5

S spin vector. 3

d electric dipole moment vector. 3

μ magnetic moment magnitude. 4

μ_0 magnetic permeability of free space. 10

ν_n neutron precession frequency. 4

$\nu_{\uparrow\downarrow}$ neutron precession frequency in anti-parallel field configuration. 5

$\nu_{\uparrow\uparrow}$ neutron precession frequency in parallel field configuration. 4

ω angular precession frequency. 5

$\overrightarrow{B_{mod}}$ vector of measurements of the modulus of the magnetic field. 13

θ angle of rotation of polarization of probe beam. 56

d_{Hg}^{false} the mercury contribution to the false EDM. 14

d_n neutron electric dipole moment magnitude. 4

d_{False} false EDM signal due to spurious frequency shift. 14

d_{fit} value for d_{false} recovered by the simulated fit routine. 16

d_{sim} value for d_{false} calculated from the exactly defined simulation values. 16

h Planck's constant. 4

h_1 height of bottom precession chamber above z=0 plane. 15

h_2 height of top of chamber above z=0 plane. 15

$\boldsymbol{\mu}$ magnetic moment vector. 3

B magnetic field vector. 3

E electric field vector. 3

c speed of light in a vacuum. 14

Acronyms

AM amplitude modulation. 49

AOM acousto-optic modulator. 58

ASD Allan standard deviation. 76

AWG arbitrary waveform generator. 65

BSM beyond the standard model. 1

C charge conjugation symmetry. 1

CP combined C&P symmetries. 2

CPT combined C,P,&T symmetries. 1

DAVLL dichroic atomic vapour laser lock. 55

DFB distributed feedback. 54

DMM digital multimeter. 64

EDM electric dipole moment. 3

FID free induction decay. 50

FOS forced oscillation scan. 74

GRIN gradient index (lens). 80

MM multimode. 87

MSR magnetically shielded room. 7

nEDM neutron electric dipole moment. 1

NMOR non-linear magneto-optical rotation. 35

P parity inversion symmetry. 1

PBS polarizing beam splitter. 87

PM polarization maintaining. 87

PS power supply. 55

RF radio frequency. 5

SCM superconducting magnet. 5

SM standard model. 2

T time reversal symmetry. 1

TUCAN TRIUMF Ultra Cold Advanced Neutron. 5

UCN Ultra Cold Neutrons. 5

Chapter 1

Introduction

A precise measurement of the neutron electric dipole moment (nEDM) is motivated by physics beyond the standard model (BSM). The current best measurement has the upper bound equal to $3 \times 10^{-26}\ e \cdot \text{cm}$ (90% C.L.) [27].

This chapter discusses the motivation for measuring the nEDM, as well as the measurement technique. This motivates a discussion of the systematic effects of magnetic fields on the experiment, and the need to measure and control them precisely.

1.1 EDMs and symmetry breaking

A symmetry is a feature of a system that remains invariant under a transformation. In particular a symmetry is a good symmetry of nature if the Hamiltonian describing the system does not change under the action of the symmetry. A symmetry is discrete if it describes non-continuous changes in a system. There are three primary discrete symmetry transformations in particle physics: charge conjugation symmetry (C), parity inversion symmetry (P), and time reversal symmetry (T). All of these symmetries are broken individually by nature in some way, but the combined CPT symmetry is believed to be an exact symmetry of nature.

C symmetry is the symmetry of fundamental charges, such as electroweak or flavour charges. This is the statement that physical processes should play out identically if all charges in a system were reversed. P symmetry is the symmetry of handedness, physical processes should be identical in a mirrored system. T symmetry is the symmetry of time, at the fundamental level microscopic processes should be completely reversible, barring emergent ensemble effects such as entropy.

C symmetry is broken maximally by the weak nuclear force. A left-handed neutrino which interacts in the standard model (SM) under charge conjugation becomes a left-handed antineutrino which does not interact. These scenarios are distinguishable experimentally. However, this symmetry is restored under an additional parity inversion, turning a non interacting left-handed antiparticle into an interacting right-handed one. Thus the combined CP symmetry is preserved in this case. CP symmetry can also be thought of as the distinction between matter and anti-matter.

In fact, while C and P symmetries are broken fundamentally through the construction of the theory of electroweak interactions, CP was thought to be a good symmetry of nature until Fitch and Cronin observed the asymmetric decay of kaon particles [9]. This is a result of the existence of a complex phase in the matrix describing quark mixing, the Cabibbo-Kobayashi-Maskawa (CKM) matrix [24]. Since CPT symmetry is a true symmetry of nature, CP violation is equivalent to T symmetry breaking, as reversing time will restore the full CPT symmetry.

This remains the only confirmed source of CP symmetry breaking in the standard model, and it is very small. Therefore, any new sources of CP symmetry breaking are more than likely some kind of new physics. In particular the strong sector analogue of the quark mixing matrix phase angle is constrained to be vanishingly small [20] by nEDM measurements (see the strong CP problem [22]), meaning new sources of CP symmetry violation in this sector can't be due to the existing model of strong interactions. Since current SM contributions to

CP violation are so small, permanent electric dipole moment (EDM) searches are considered background-free probes of BSM physics [35].

The motivations for expecting to find new sources of CP violation come in two broad categories: explaining something we see (baryon asymmetry) and explaining something we don't see (flavor diagonal CP violation).

The uniformity of the cosmic microwave background motivates modern inflationary models, which imply the universe started in a very uniform symmetric state. The current asymmetry we see between matter and anti-matter in the universe therefore requires the Sakharov conditions [32] be met in the early universe:

- C and CP symmetry violation
- Reactions out of thermal equilibrium
- Baryon number violation

The current SM CP violation is not enough to explain the asymmetry.

To see why EDMs are intimately connected to CP violation, take an example particle with both electric dipole moment $\mathbf{d}=d\,\frac{\mathbf{S}}{S}$ and magnetic moment $\boldsymbol{\mu}=\mu\,\frac{\mathbf{S}}{S}$, where $\mathbf{S}$ is the spin of the particle. In the presence of both a magnetic field $\mathbf{B}$ and electric field $\mathbf{E}$, the classical Hamiltonian is:

$$H = -\mu\mathbf{B}\cdot\frac{\mathbf{S}}{S} - d\mathbf{E}\cdot\frac{\mathbf{S}}{S}. \tag{1.1}$$

The results of a time reversal operation can be understood by examining the symmetries of $\mathbf{E}, \mathbf{B}$, and $\mathbf{S}$. Both $\mathbf{B}$ and $\mathbf{S}$ are odd under time reversal. If $\mathbf{B}$ were the result of a current loop, reversing time would reverse the current and $\mathbf{B}$ will also reverse. Reversing time would also cause direction of spin to change, so the full term must be even under time reversal.

In the second term $\mathbf{S}$ is still odd under time reversal, but an electric field is the result of a static configuration of charges, so $\mathbf{E}$ will not change direction under time reversal. This

combination of terms must be odd under time reversal.

Under a time reversal operation, T(H), the Hamiltonian is:

$$\mathrm{T}(H) = -\mu \mathbf{B} \cdot \frac{\mathbf{S}}{S} + d\mathbf{E} \cdot \frac{\mathbf{S}}{S}. \tag{1.2}$$

The dipole term d is proportional to the change under T (and therefore CP) reversal, so it is an indication of CP violation.

1.2 nEDM measurement principles

The measurement of the nEDM takes direct advantage of the difference between equations 1.1 & 1.2. The Hamiltonian describing a neutron in an external electromagnetic field gives the total energy of the system, and can be written

$$H = h\nu_n, \tag{1.3}$$

where h is Planck's constant, and ν_n is the precession frequency of the neutron. By measuring this frequency while the neutron is in different electromagnetic field configurations, the EDM can be measured. Equation 1.1 is the Hamiltonian for arbitrary fields, but we can examine some specific scenarios. If we say that the externally applied electric and magnetic fields are *parallel*, the equation is

$$h\nu_{\uparrow\uparrow} = 2\mu_n B + 2d_n E, \tag{1.4}$$

analogous to equation 1.1 in form. $\nu_{\uparrow\uparrow}$ is the precession frequency in the parallel field configuration, B & E are the magnitudes of the fields, μ is the magnitude of the magnetic moment, and d_n is the magnitude of the EDM. Relative signs of expressions are accounted

for by construction. If the fields are *anti-parallel*, the equation is

$$h\nu_{\uparrow\downarrow} = 2\mu_n B - 2d_n E, \tag{1.5}$$

analogous to equation 1.2 in form. $\nu_{\uparrow\downarrow}$ is the precession frequency in the anti-parallel field configuration. If the magnitudes of **B** & **E** are the same in these two measurements, we can solve for our desired d_n:

$$d_n = \frac{h(\nu_{\uparrow\uparrow} - \nu_{\uparrow\downarrow})}{4E} = \frac{\hbar(\omega_{\uparrow\uparrow} - \omega_{\uparrow\downarrow})}{4E}, \tag{1.6}$$

where $\hbar = \dfrac{h}{2\pi}$ and $\omega = 2\pi\nu$. A precise measurement of d_n is predicated on very fine control of **B**. Confirming a non-zero value for d_n would indicate a new source of CP symmetry violation and BSM physics.

In order to measure the change in precession frequency, we use Ramsey's method of separated oscillatory fields, a precise method of measuring frequency. In order to hold neutrons in carefully controlled electric and magnetic fields, we use neutrons with such low kinetic energy that they are totally reflected from physical surfaces, and can be guided and held in specially coated and polished guides and chambers. These are called Ultra Cold Neutrons (UCN), produced at the TRIUMF Ultra Cold Advanced Neutron (TUCAN) source, at TRIUMF in Vancouver, BC, Canada.

In Ramsey's method, UCN are first polarized parallel to **B**, by passing through a very large (∼4 T) magnetic field created by a superconducting magnet (SCM). They are then subjected to a precise radio frequency (RF) electro-magnetic pulse perpendicular to **B** which rotates their spins until they are also perpendicular to **B**. This pulse is at the Larmor precession frequency of the neutrons, so if it is timed such that it lasts for $\pi/2$ radians of the neutrons precession, the neutron spin is left exactly in the perpendicular plane of **B**.

The neutrons then precess freely in the magnetic field lines for a time T_{Ramsey}. At the end of the Ramsey cycle, a coherent RF pulse of the same duration is applied again, and

the number of polarized UCN in each state (spin-up/spin-down) is measured. This is done by counting the number of neutrons which successfully pass through a thin magnetized film, which can only be navigated by one polarization state (either up or down, respectively). When the second RF pulse is applied, the populations are directly related to the accrued phase of the UCN relative to the RF clock. It is also directly related to the exact time between the pulses, and the frequency of spin precession.

If the second RF pulse occurs as the UCN have completed exactly an integer number of precessions, the pulse will reverse nearly all the spins, and the UCN will be in the spin-down state after the Ramsey cycle. As the timing of the pulse is scanned from run to run, less and less of the UCN will be successfully spin-flipped by the RF pulse, until a minimum happens at exactly a half-integer number of precessions. Figure 1-1 shows this resonance as a function of T_{Ramsey}. The vertical axis is the number of neutrons detected in the spin state being measured, so this curve is the negative of the probability distribution.

Rather than scan the entire resonance, four points in the resonance are selected near the steepest (and therefore most sensitive) parts of the curve. By performing a Ramsey cycle at these four values of T_{Ramsey} the central frequency can be deduced. Conducting the experiment for both parallel and anti-parallel $\mathbf{B}$ & $\mathbf{E}$ configurations, a precise measurement of the phase shift due to the electric field can be made via equation 1.6.

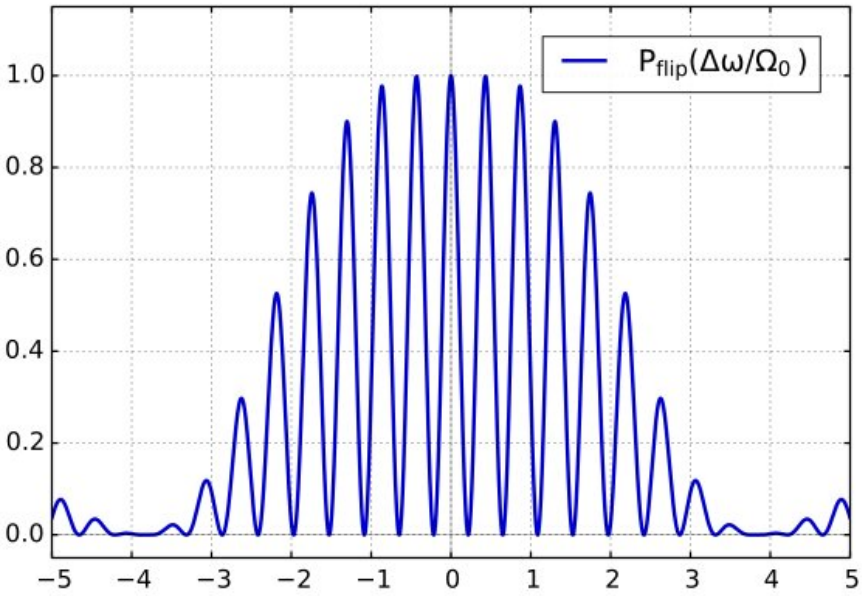

Figure 1-1: An experimental Ramsey fringe pattern. The horizontal axis is shown in Hz, centred around the resonance. Mplwp ramsey fringes monochromatic.svg by Geek3 is licensed under CC BY (https://creativecommons.org/licenses/by/3.0)

1.3 False EDMs and the TUCAN nEDM experiment

In the TUCAN nEDM experiment, the Ramsey cycle will be carried out in a pair of precession chambers located in a magnetically shielded room (MSR). The electrode that provides the electric field is located between the chambers, so that the electric field is equal in magnitude but opposite in polarity in the two chambers. The two chambers are surrounded by a solenoid providing a uniform magnetic field along the positive z axis, providing parallel **B** & **E** fields in one chamber and anti-parallel in the other, allowing for simultaneous measurements of the two configurations. If the magnetic field in the two chambers changes over the course of a Ramsey cycle, this will result in a frequency shift in the UCN. In order to monitor the magnetic field as the experiment is run, the RAL/SUSSEX/ILL nEDM measurement [27] [7] introduced the use of a cohabiting magnetometer, or comagnetometer. TUCAN will use this technique also. The comagnetometer is a polarized atomic species (^{199}Hg in this case)

introduced into the two precession chambers along with the UCN, which then precesses in the magnetic field according to its gyromagnetic ratio. Unlike the neutrons, the comagnetometer species can be interrogated by polarized light to monitor the strength of the magnetic field. Any changes in the field can therefore be corrected. This technique is conceptually similar to the magnetometry system I develop in this work.

While the comagnetometer solves the problem of the magnetic field drifting over time, it introduces a systematic error. If the magnetic field in the chamber is non-uniform, in general a trapped particle will develop a frequency shift (see section 2.1.3). Any frequency shift correlated with E-reversal would mimic an EDM result. If these shifts are the result of some systematic effect we call these signals false EDMs. This means both the neutrons and the ^{199}Hg develop a false EDM that must be accounted for. Since the comagnetometry system is blind to this effect, a new magnetometry subsystem must be developed that can measure and correct for magnetic field dependant effects, such as the frequency shift highlighted here.

In order to develop such a system, a way of characterizing the magnetic fields in the region of our experiments must be developed. In the following chapter a field decomposition is performed using the same prescription given in reference [3]. This leads to a natural way of extracting the relevant magnetic field information using measurements of the field surrounding the region of interest. This chapter also determines the operating requirements of the optical magnetometers required for such a system. The operating principles of optical magnetometry are described in the third chapter. In the final chapters a proof of concept optical magnetometer is built and demonstrated to meet the requirements of such a system. Commercial integration/production is discussed in the conclusion.

Chapter 2

Magnetic field characterization

2.1 Field decomposition

In order to characterize the gradients that contribute to systematic effects in the nEDM experiment, we perform a multipole decomposition of the magnetic scalar potential using a basis of spherical harmonic functions. This section details the process of decomposing the magnetic field into this basis, then prescribes a method by which the strength of each multipole can be obtained from magnetic field measurements. The relative contributions of these multipoles to a systematic error is calculated. I also discuss simulating these fields and simulating the response of magnetometers, in an effort to place requirements on the final system.

2.1.1 Harmonic decomposition

The basic equations of magnetostatics [19] in vacuum are

$$\vec{\nabla} \times \mathbf{B} = \mu_0 \overrightarrow{J_f}, \tag{2.1}$$

$$\vec{\nabla} \cdot \mathbf{B} = 0. \tag{2.2}$$

Where $\mathbf{B}$ is the magnetic field, μ_0 is the vacuum permeability, and $\vec{J_f}$ is any free current in the space. In the absence of magnetic materials or currents (which we have by construction), equation (2.1) becomes $\vec{\nabla} \times \mathbf{B} = 0$, allowing us to express the vector magnetic induction $\mathbf{B}$ as the gradient of a magnetic scalar potential:

$$\mathbf{B} = -\vec{\nabla}\Phi. \tag{2.3}$$

Where Φ is the magnetic scalar potential. Using equation (2.2), Φ now satisfies Laplace's equation:

$$\nabla^2 \Phi = 0. \tag{2.4}$$

In spherical coordinates, Laplace's equation has a solution [33] in the form

$$\Phi = \sum_{l,m} [A_{l,m} r^l + B_{l,m} r^{-(l+1)}][C_{l,m} \cos(m\phi) + D_{l,m} \sin(m\phi)][E_{l,m} P_l^m(\cos\theta) + F_{l,m} Q_l^m(\cos\theta)], \tag{2.5}$$

where P_l^m and Q_l^m are the associated Legendre polynomials of the first and second kind. Since $r^{-(l+1)}$ diverges at $r = 0$ we set $B_{l,m} = 0$. The Legendre polynomials of the second kind diverge when $\cos\theta = 1$, so we set $F_{l,m} = 0$. The remaining constants are collected in $C_{l,m}$, and are chosen to have convenient properties for the z derivatives of these functions. See Appendix A for details, and a list of functions.

The basis, first presented in reference [3], is defined as follows:

$$\Phi_{l,m} = C_{l,m}(\phi) r^l P_l^{|m|}(\cos\theta) \tag{2.6}$$

with

$$\begin{aligned} C_{l,m}(\phi) &= \frac{(l-1)!(-2)^{|m|}}{(l+|m|)!}\cos(m\phi) && \text{for } \ m \geq 0 \\ &= \frac{(l-1)!(-2)^{|m|}}{(l+|m|)!}\sin(|m|\phi) && \text{for } \ m < 0. \end{aligned} \tag{2.7}$$

Where $\Phi_{l,m}$ are the basis functions. Using equation (2.3) the basis functions of the magnetic field, $\Pi_{\hat{e_i},l,m}$, can be written:

$$\Pi_{\hat{e_i},l,m} = -\partial_{\hat{e_i}} \Phi_{l+1,m}. \tag{2.8}$$

A full list of these functions is presented in the appendix. Note the change in index from $l+1$ to l, meaning $G_{1,2}$ is a sensible gradient term, despite having $m > l$. In this notation, l always refers to the order of the polynomial in $\Pi_{\hat{e_i},l,m}$. The magnetic field at a single position can then be written:

$$\mathbf{B}(\vec{r}) = \sum_{l,m} G_{l,m} \begin{pmatrix} \Pi_{x,l,m}(\vec{r}) \cdot \hat{i} \\ \Pi_{y,l,m}(\vec{r}) \cdot \hat{j} \\ \Pi_{z,l,m}(\vec{r}) \cdot \hat{k} \end{pmatrix} \tag{2.9}$$

or in multiple locations, indexed by n:

$$\begin{bmatrix} B_x(x_1,y_1,z_1) \\ \vdots \\ B_y(x_1,y_1,z_1) \\ \vdots \\ B_z(x_1,y_1,z_1) \\ \vdots \\ B_z(x_n,y_n,z_n) \end{bmatrix} = \begin{bmatrix} 0 & 0 & 1 & y_1 & 0 & \frac{-1}{2}x_1 & z_1 & x_1 & 2x_1y_1 & 2y_1z_1\cdots \\ \vdots & \vdots & \vdots & \vdots & \vdots & \vdots & \vdots & \vdots & \vdots & \ddots \\ 1 & 0 & 0 & x_1 & z_1 & \frac{-1}{2}y_1 & 0 & -y_1 & x_1^2-y_1^2 & 2x_1z_1\cdots \\ \vdots & \vdots & \vdots & \vdots & \vdots & \vdots & \vdots & \vdots & \vdots & \ddots \\ 0 & 1 & 0 & 0 & y_1 & z_1 & x_1 & 0 & 0 & 2x_1y_1\cdots \\ \vdots & \vdots & \vdots & \vdots & \vdots & \vdots & \vdots & \vdots & \vdots & \ddots \\ 0 & 1 & 0 & 0 & y_n & z_n & x_n & 0 & 0 & 2x_ny_n\cdots \end{bmatrix} \cdot \begin{bmatrix} G_{0-1} \\ G_{00} \\ G_{01} \\ G_{1-2} \\ G_{1-1} \\ G_{10} \\ G_{11} \\ G_{12} \\ G_{2-2} \\ G_{2-1} \\ \vdots \end{bmatrix} \tag{2.10}$$

$$\begin{bmatrix} \vec{B}_x \\ \vec{B}_y \\ \vec{B}_z \end{bmatrix} = \begin{bmatrix} T_x \\ T_y \\ T_z \end{bmatrix} \cdot \begin{bmatrix} \vec{g} \end{bmatrix}. \tag{2.11}$$

The $G_{l,m}$ are called the gradient terms, since they describe the contribution of a mode to the overall field.

Equation (2.11) is the start of the working equation. $\vec{B}_x$, $\vec{B}_y$, and $\vec{B}_z$ are lists of magnetic field measurements along the x, y, and z directions at the various locations indexed by n. T_x, T_y, and T_z are transformation matrices that have as entries the polynomial basis functions evaluated at the positions associated with each measurement in $\vec{B}_x$, $\vec{B}_y$, and $\vec{B}_z$. $\vec{g}$ is referred to as the gradient vector from now on, as it is a list of the gradient terms. The magnetic field and the positions of each magnetometer are measurable. As long as the transformation matrices are of sufficient rank to be inverted, the gradient terms can be calculated.

2.1.2 Refining the working equation

The Cs magnetometers are scalar instruments in their current configuration, they only report the field magnitude. However, by construction the nEDM magnetic field is oriented along the z axis. Taking only the z component of equation (2.11):

$$\vec{B_0} \approx \vec{B_z} = T_z \cdot \vec{g}. \tag{2.12}$$

Where $\vec{B_0}$ is the actual field in the experiment. This equation contains most of the magnetic field information in the system, since $\vec{B_0}$ is mostly in the z direction. In general, there can be more measurements than there are gradient terms, so T_z can be a non-square matrix. By performing a Moore-Penrose pseudoinversion (using the built-in pinv.m function in MATLAB: Copyright 1984-2015 The MathWorks, Inc.), the gradient vector can be extracted from this list of field measurements. This is equivalent to finding a least-squares fit [29] to the system of linear equations in equation (2.12).

$$\vec{g} = pinv(T_z) \cdot \vec{B_z}. \tag{2.13}$$

B_z isn't what is measured by the magnetometers, so we replace $\vec{B_z}$ in our working equation by $\overrightarrow{B_{mod}}$, a tuple of field magnitude measurements B_{mod}:

$$\vec{g} \approx pinv(T_z) \cdot \overrightarrow{B_{mod}}, \tag{2.14}$$

keeping in mind that $\overrightarrow{B_{mod}}$ is *not* the modulus of some B vector, rather a vector of B_{mod} values. The working equation is now an approximation that correctly ignores transverse fields.

2.1.3 Comagnetometer d_{false} as a function of gradient terms

In general, a charged particle trapped in a magnetic gradient will develop a frequency shift proportional to **E** in its precession. In a frequency measurement such as the nEDM experiment, this mimics an EDM signal. Since this signal is not caused by a real EDM, we call signals like this a *false EDM*, d_{False}. This kind of signal is the most basic kind of gradient dependant systematic effect, and I will be focusing on this quantity to evaluate efficacy of this system. The false EDM signal of the ^{199}Hg in our trap is given in reference [30] as:

$$d_{\text{false}} = -\frac{\hbar\gamma^2}{2c^2}\left\langle xB_x + yB_y \right\rangle, \tag{2.15}$$

where the brackets indicate an average over the containing volume. $\hbar$ is the reduced Planck's constant, c is the speed of light, and γ is the gyromagnetic ratio of the trapped particle. d_{false} is the quantity I wish to determine accurately with this system. This can be written in terms of the scalar potential field:

$$d_{\text{false}} = -\frac{\hbar\gamma^2}{2c^2}\left\langle x\frac{\partial\Phi}{\partial x} + y\frac{\partial\Phi}{\partial y} \right\rangle. \tag{2.16}$$

Since the precession frequency of the mercury is used to measure the magnetic field experienced by the neutrons, any frequency shift in the mercury translates to the neutrons false EDM by the ratio of their gyromagnetic ratios. Identifying that $x\partial_x + y\partial_y = \rho\partial_\rho$:

$$d_{Hg}^{\text{false}} = -\frac{\hbar\gamma_{\text{Hg}}\gamma}{2c^2}\sum_{l,m} G_{l,m}\langle\rho\Pi_{\rho,l,m}\rangle, \tag{2.17}$$

where $\Pi_{\rho,l,m}$ is defined as above, d_{Hg}^{false} is the mercury contribution to the neutron false EDM, and γ_{Hg} is the gyromagnetic ratio of the comagnetometer species. With R as the radius of the precession chamber, and $H = h_2 - h_1$ as the height, integrating and expanding the equation

to fifth order:

$$d_{Hg}^{\text{false}} = \frac{\hbar\gamma_{\text{Hg}}\gamma}{8c^2}\cdot R^2\left\{G_{1,0}+G_{2,0}(h_2+h_1)-\frac{G_{3,0}}{2}(R^2-2h_1^2-2h_1h_2-2h_2^2)+\right.$$
$$\left. G_{4,0}\left[\frac{R^2(h_2^2-h_1^2)}{(h_1-h_2)}-\frac{(h_2^4-h_1^4)}{(h_1-h_2)}\right]+G_{5,0}\left[\frac{-(h_2^5-h_1^5)}{h_2-h_1}+5\frac{R^2}{3}\frac{(h_2^3-h_1^3)}{h_2-h_1}-\frac{5R^6}{16}\right]\right\}, \quad (2.18)$$

where h_1 and h_2 are the height of the top and bottom of the chamber above the z=0 plane.

Numerically,

$$\frac{\hbar\gamma_{\text{Hg}}\gamma}{8c^2} = 1.28\times10^{-36}\ \text{C}\cdot\text{m}\cdot\frac{\text{m}}{\text{T}}\cdot\frac{1}{\text{m}^2} = 7.99\times10^{-30}\ \text{e}\cdot\text{cm}\cdot\frac{\text{cm}}{\text{pT}}.\cdot\frac{1}{\text{cm}^2} \quad (2.19)$$

Writing lengths in cm and $G_{l,m}$ in pT/cm^l, equation (2.19) allows equation (2.18) to arrive at

$$d_{Hg}^{\text{false}} = 6.5\times10^{-28}G_{10}+1.6\times10^{-26}G_{20}+2.4\times10^{-25}G_{30}+1.7\times10^{-24}G_{40}+3.4\times10^{-22}G_{50}, \quad (2.20)$$

using $R = 18$ cm, $h_2 = 20.05$ cm, and $h_1 = 5$ cm. These are the values in the latest design at the time of calculation. ℓ has the same value as the index in $G_{l,m}$.

Due to the cylindrical symmetry of the precession chamber only $m = 0$ terms contribute. The ℓ = even terms contribute in the case of these cells because they are offset along the z axis. These terms would be zero for the case of a single cell centred at the origin [3]. In fact it can be shown [23] that for a spherical cell only terms with $m = 0$, $\ell = 0, 1, 2$ can contribute. The cited paper, written alongside this thesis, is included in the appendix for further reading. The thrust of the argument is to show that the operator $x\partial_x + y\partial_y = \rho\partial_\rho$ can be written as a set of spherical tensors of rank 0 and 2, then to show that due to the angular momentum selection rules of Clebsch-Gordon coefficients only $\ell = 0, 1, 2$ and $m = 0$ terms can contribute to the sum.

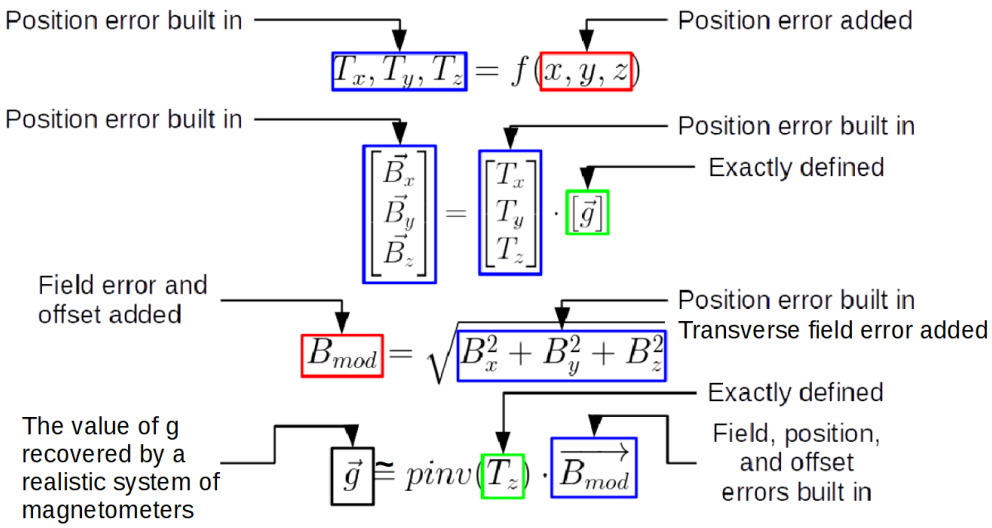

Figure 2-1: An outline of the simulation/fitting algorithm. Red boxes indicate an error being added to that value. Blue boxes indicate that an error has been accounted for in somewhere in the calculation of that variable, and green boxes are exactly defined quantities.

2.2 Simulating magnetometers

In order to evaluate how well the working equation can extract gradient values, realistic magnetometers were simulated. Equation (2.11) allows a field to be exactly defined in all space by defining a gradient vector $\vec{g}$. The magnetometers' realistic response was calculated, and the working equation (2.14) was used to extract the measured $\vec{g}$. The d_{fit} recovered by the fit algorithm and the magnetometry system was compared to the exactly defined d_{sim} in the simulation as a figure of merit.

The magnetometers have a finite field sensing error which must be accounted for. In addition, since the transformation matrices depend on the positions, error in placement must also be accounted for. Figure 2-1 outlines this process. If a quantity was experienced by a magnetometer, like the exactly defined field or its nominal position, the quantity was exactly defined. Whenever a quantity was measured by a magnetometer, like its actual position or the field it records, the quantity had an error added. It is important to note in

the last step that T_z was calculated using the exactly defined positions, with no errors built in. If T_z was used with the same error built in, the position error would cancel itself out in this step.

One last thing to take into account is the fact that the magnetometers operate by passing a laser through a glass cell of finite size, full of cesium vapour in our case. They report the magnitude of the volume average of the field inside the cell. The volume averaging effect is taken into account by sampling the space inside where the cell would be, spreading ≈ 100 points evenly in the space and reporting the average. This was found to be a very small correction, and the size of the cell did not effect results even for 10 cm diameter magnetometer cells. This step was left out to save computation power in further runs.

2.2.1 Gradient generation and truncation

In order to test the magnetometer response to realistic magnetic fields, a method was developed to generate realistic gradient vectors. A reasonable truncation was also found.

The overall goal of the experiment is to measure the neutron EDM with an uncertainty of 1×10^{-27} e·cm. If $d_{false} << 1 \times 10^{-27}$ e·cm level, it will not significantly impact the experiment. To provide a lower boundary for gradient terms that contribute significantly, the value of each of $G_{l,0}$ that would make $d_{Hg}^{\text{false}} = 1 \times 10^{-27}$ was calculated, shown in table 2.1. All gradient components of the same l order get the same lower bound. From equation (2.2) gradients are equivalent to transverse fields, so the field with small random gradients can be written

$$\vec{B} = \vec{B_z} + \delta\vec{B}_{rand}, \tag{2.21}$$

where $\delta\vec{B}_{rand}$ is a small variation on the main $\vec{B_z}$ field. Setting a uniform lower bound for each term in an order is equivalent to saying $\delta\vec{B}_{rand}$ is isotropic.

The performance of existing magnetically shielded environments was used as a reasonable

Table 2.1: The values needed for each gradient component to have a 1×10^{-27} e·cm contribution to the neutron false EDM

Gradient component	Value to make dFalse $= 1 \times 10^{-27}$e·cm
G_{10}	1.5 pT/cm^l
G_{20}	6.3×10^{-2} pT/cm^l
G_{30}	4×10^{-3} pT/cm^l
G_{40}	6×10^{-4} pT/cm^l
G_{50}	3×10^{-6} pT/cm^l

Table 2.2: The values needed for each component by itself to generate a variation of 3 nT in a cubic meter centred at the origin.

Gradient component	Value to make field variation of 3 nT/m
G_{10}	28 pT/cm^l
G_{20}	4×10^{-1} pT/cm^l
G_{30}	3×10^{-3} pT/cm^l
G_{40}	2×10^{-5} pT/cm^l
G_{50}	2×10^{-7} pT/cm^l

upper bound on $G_{l,m}$. The Institut Laue–Langevin (ILL) nEDM experiment calculated that they were able to control their worst gradient ($\frac{\partial B_z}{\partial z}$) to be less than 3 nT/m [28]. To generalize this to place constraints on $l \neq 1, m \neq 0$ gradients, I define a gradient as being too large if it causes a total variation of more than 3 nT in a cubic meter, that is, the difference between the highest field value and the lowest field value in a cubic meter must be less than 3 nT. Table 2.2 lists the values required for each component to produce a 3 nT variation.

Comparing Tables 2.1 and 2.2, realistic gradients of order 4 or higher induce $d_{False} < 1 \times 10^{-27}$ e $\cdot$ cm. Third order gradient terms are therefor sufficient to accurately correct for d_{False}. Exact values will be calculated to fifth order for the simulations, but the final gradient extraction algorithm will only be up to third order.

2.3 Optimization and requirements

The goal of the studies with simulated magnetometers was to determine the number and sensitivity requirements of the magnetometers in light of sensing errors, position errors, transverse fields, and placement constraints such as the cells themselves and the high **E** gradient. These parameters depend on finding an optimally performing set of positions. This optimization was done by simulating the response of magnetometers as described in the previous section, and minimizing the difference between the exactly calculated d_{False}, referred to as d_{sim}, and the recovered d_{False}, referred to as d_{fit}.

For section 2.3.1, the field sensing errors and placement errors were constant throughout, at the level of the noise floor of this type of magnetometer [8]. The sensing error was 10 fT, and the placement error was 0.1 cm. 10,000 randomly generated gradients were produced for each set of positions to measure.

2.3.1 Parameterized positions

"Parameterized" refers to a set of positions that could be described by a reasonably simple function, as this is how they are generated.

Although for a third order fit 16 magnetometers is all that is required, all the tests in this section are shown with 20 magnetometers, for the sake of easy comparison with the results from section 2.3.2.

The highest order contribution to the false EDM is proportional to G_{10}. Examining equation 2.10, the B_z basis function associated with G_{10} is z, so G_{10} is proportional to change in B_z with z, or $\frac{\partial B_z}{\partial z}$. A first try at placing the magnetometers in the volume was two rings of magnetometers, one above the precession chamber and one below, in order to get $\frac{\partial B_z}{\partial z}$ information.

Figure 2-3 shows the results of testing this set of positions on 10,000 randomly generated

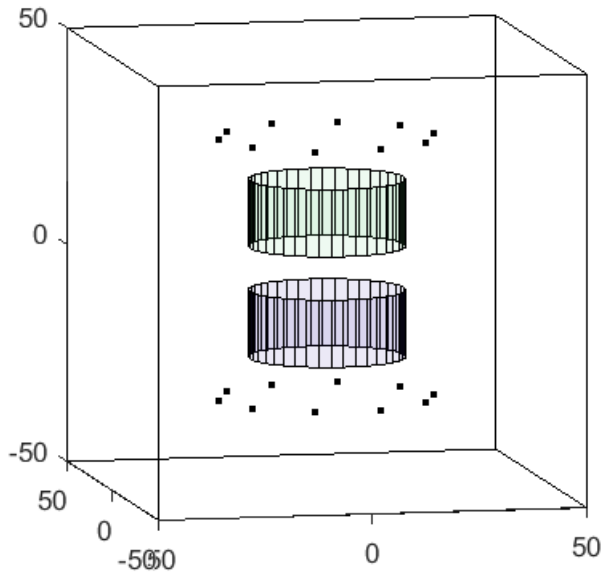

Figure 2-2: The first set of positions tested, two rings of ten magnetometers above and below the chambers.

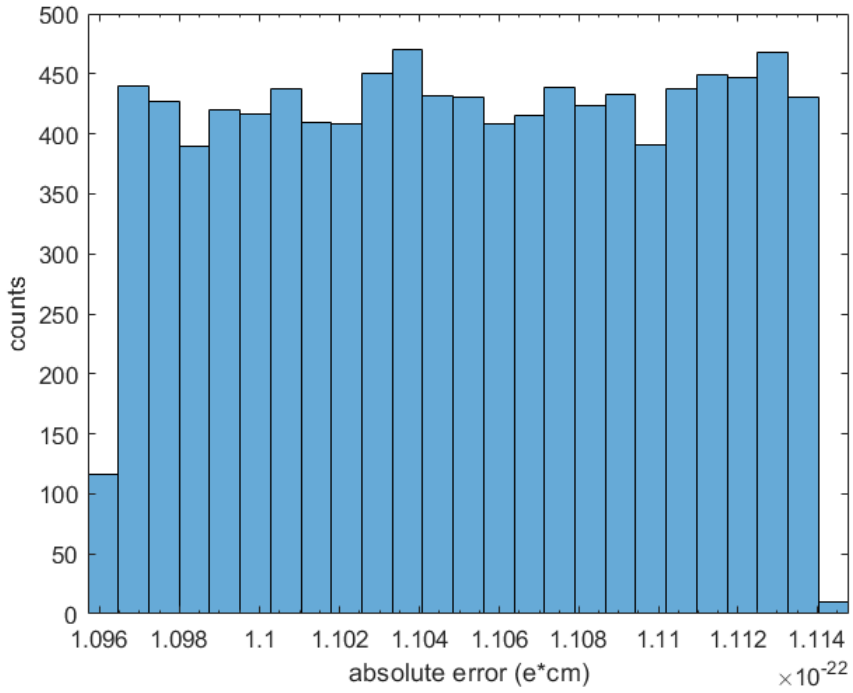

Figure 2-3: The results of testing two rings of magnetometers. As you can see, the absolute error (i.e the difference between d_{sim} and d_{fit}) is 5-6 orders of magnitude higher than acceptable.

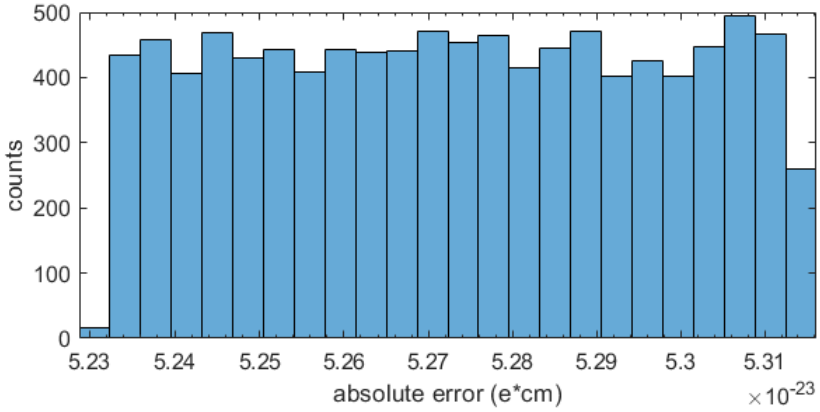

Figure 2-4: The results of 10,000 fits to generated gradients using asymmetric rings of magnetometers.

(realistic) gradients. The absolute error is 5-6 orders of magnitude larger than the goal, this set of positions is not good.

To see why this might be, consider the example of all 20 magnetometers laying on an equi-magnetic surface in the volume. While still technically solvable, the report of the magnetometers would become dominated by the random fluctuations away from the single real measurement value, and the result would be meaningless. In order to accurately extrapolate a mode of the magnetic field, the signal being read by the magnetometers should rise above the noise of the magnetometers, meaning a large relative difference in value.

The next layout is a slight tweak of the first. The lower ring of magnetometers has an angular offset to begin breaking the symmetry, as well as a slightly different radius and height. This offset is larger than the position errors. Figure 2-4 shows the results of another 10,000 generated gradient vectors. An improvement is evident, but still not close to the goal of 1×10^{-27} e·cm.

Extending this principle of breaking symmetry we can have a variable angular offset, a variable z-axis offset, and a variable radial offset. In addition, the upper and lower sets of magnetometers can have different constants for the variation. The result is two winding

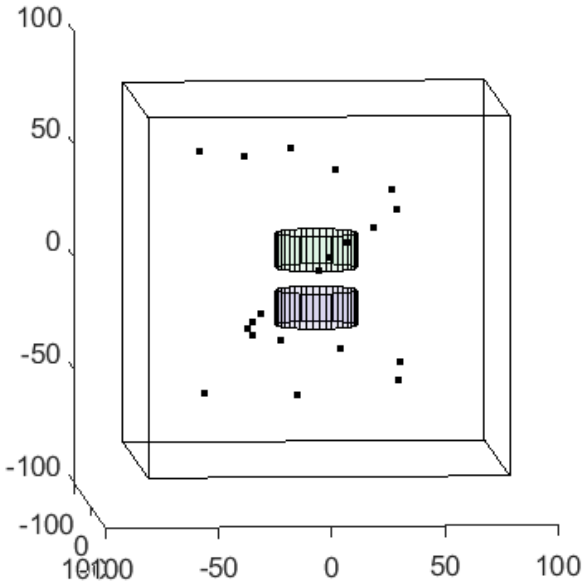

Figure 2-5: The helical layout of magnetometers.

helical structures, designed to hopefully not have significant symmetry with regard to the low order gradients we are trying to sense. This layout is seen in figure 2-5. Each sensor is further than 0.5 cm from its original position. Figure 2-6 shows improvement again, with some results close to the 1×10^{-27} e·cm level.

A logical extension of this symmetry breaking is a completely random layout of magnetometers. Indeed, figure 2-7 shows another clear improvement over previous layouts. Another method is needed to make further progress.

2.3.2 Global position optimization

Ferret is a part of the nQube advanced global optimization toolbox, developed by Dr. Jason Fiege [14], professor of astrophysics at the University of Manitoba. He has provided this software and support for it to our collaboration.

Ferret is an evolutionary optimizer, a class of program that takes problem solving inspiration from the principles of biological evolution [36] [18]. The role of Ferret in this work is

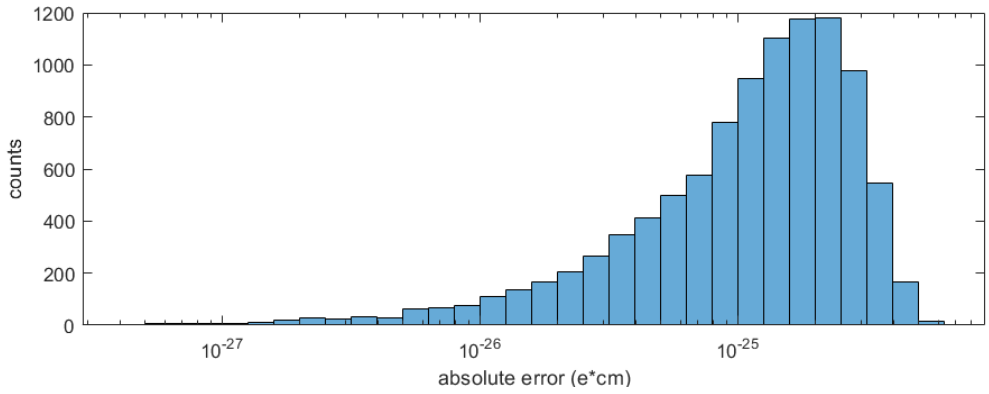

Figure 2-6: The results of 10,000 fits to generated gradients, using a helical layout of magnetometers. Another clear improvement is seen.

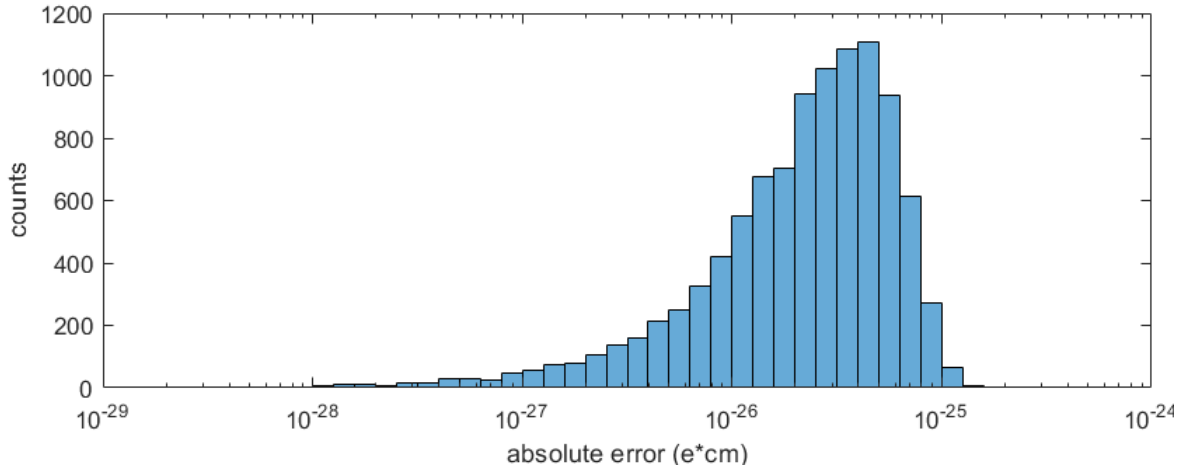

Figure 2-7: The results of 10,000 fits to generated gradients. This is now a random scattering of magnetometers around the chamber. Another increase in precision is apparent.

to optimize the placement of magnetometers in the magnetically shielded volume. 20 magnetometers means 60 position parameters to simultaneously (and globally) optimize with respect to some measure of fitness, or goal. This is the kind of problem that an evolutionary algorithm is ideal for. Evolutionary algorithms have been used to design antennae [18] [11], and image reconstruction techniques [21] specifically dealing with limited measurements or projections. They have also been employed in the design of radio telescope arrays, a close analogue to the kind of field decomposition involved in this work. In particular, the results of reference [15] closely follow the results in section 2.3.1, including the performance of a random array of sensors, and the observation that arrays with regular spatial structures introduce problems for the reconstruction algorithm. They conclude that this kind of optimization is most advantageous when dealing with small numbers of sensors, as is the case in this work.

It should be noted that most evolutionary algorithms try to *maximize* some parameter, attempting to find the highest fitness value. Ferret actually seeks to *minimize* the fitness goal [13] in this configuration, which allows for a more straightforward method of punishing particularly undesirable positions.

The basic algorithm is as follows: Ferret provides the gradient decomposition code a list of sets of parameters (position coordinates) to be evaluated. The decomposition code tries to use each provided set of positions to extract d_{false} from a randomly generated field. The absolute difference between d_{sim} and d_{fit} is reported as the fitness of that generation, the quantity to be minimized. Once a fitness is calculated for each set of positions that Ferret provided, new sets of parameters are generated based on how well the previous ones did. These sets are referred to as generations. Each generation has 500 different sets of positions to test. Huge improvements over just 20-30 generations are not unusual to see.

Ferret continually monitors its own progress, and changes its optimization strategy based on its performance. Occasionally it will completely randomize any non-optimal members of

a generation, casting a wider "net" over the parameter space. This process is called a super-mutation [13]. Once Ferret decides that evolution is done, i.e. no more improvements are being made, it analyzes the history of the entire evolution to construct the optimal set of parameters. This can also be triggered at any time manually.

Ferret offers some control over the parameter space. An upper and lower bound can be defined for each parameter, and a penalty function can also be defined. The penalty function adds a large amount to the fitness whenever a magnetometer is placed somewhere out-of-bounds, like in a precession chamber, or outside the vacuum chamber. This means the upper and lower bounds of the parameters do not need to be defined to avoid keep-out zones, Ferret will avoid them automatically due to the penalty function. This will also allow keep-out zones to be included in the future that allow for the high voltage lines and the UCN guide(s). The further Ferret gets into a keep-out zone, the more it is punished. While Ferret never explicitly calculates any gradients in parameter space [13], this will tend to push the positions toward a lower penalty, until its pushed out of the keep-out zone.

Due to computation time constraints, Ferret can only test each position set against a few randomly generated gradients. It is possible that a particular set of positions is identified as being good simply because it was tested against easy to identify gradients. To mitigate this the results from Ferret are further tested against 10,000 randomly generated gradients to produce the histograms shown previously. The results from this second test are what I interpret as the actual fitness of each set of positions.

The complexity of the evolutionary algorithm process makes the fitness a very complicated function of all the variables, e.g: a good placement for a low-precision magnetometer is not necessarily a good placement for a high-precision magnetometer, even if the only difference is the accuracy of the magnetometers. Similarly, a set of good positions for low-precision magnetometers cannot be improved simply by increasing their precision. Any change in the system at all will result in an unpredictable change in the fitness "landscape".

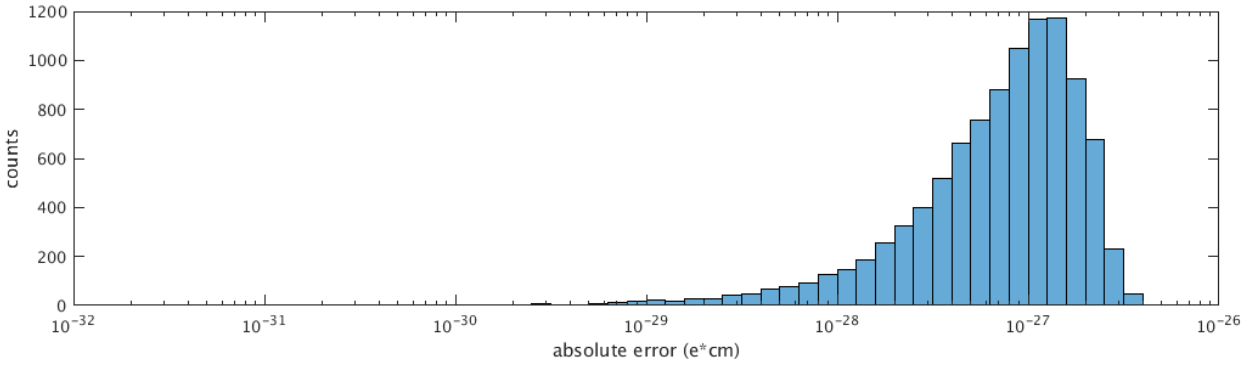

Figure 2-8: The results of putting the above magnetometers into Ferret for 93 generations. The optimal solution was reported with a fitness of 1.4×10^{-31} e·cm

Ferret can optimize the positions of the magnetometers, but only once the magnetometry parameters are defined, such as the positioning and sensing errors, and the total number of sensors. These parameters are optimized iteratively.

If the average error in d_{false} is too large, then the parameters are adjusted in a way that will make the system more accurate, usually by decreasing either the positioning error or the field sensing error, or by increasing the number of sensors. If the error in d_{false} is significantly smaller than the goal, the parameters are adjusted in a way that will make the system easier to implement, usually by relaxing the sensitivity requirements of the magnetometers, or by decreasing the number of magnetometers. This method should result in a system that is both effective and efficient. 20 magnetometers ended up being a good number, and was used in this chapter.

Keeping all non-position parameters the same as the previous section, Ferret was used to optimize the layout of 20 magnetometer positions. This first optimization is done without the averaging described in section 2.3.3. The results of 93 generations of optimization are shown in figure 2-8. To give an idea of how fast Ferret can arrive at a good result, it took only 25 generations of 500 members each to reach a reported fitness of 9.7×10^{-31}.

The results are now almost all within 2×10^{-27}, close to the goal. However, it is important

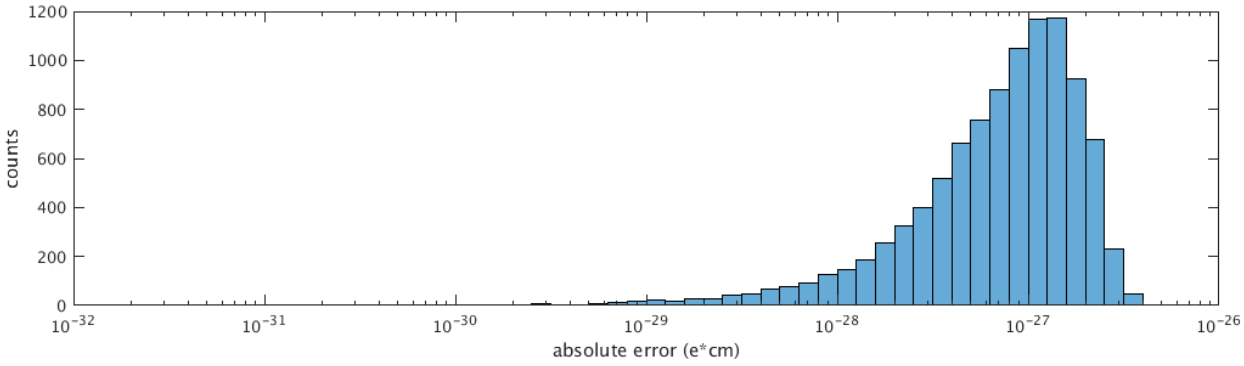

Figure 2-9: The same magnetometers are tested, but with the additional step of averaging. The optimal solution was reported with a fitness of 3.4×10^{-29}, much closer to the centre of this distribution, showing the improvement. The magnetometry results are the same, but the fitness is more accurate.

to note that the fitness associated with this solution was reported as 1.4×10^{-31}, nearly 4 orders of magnitude smaller. This is addressed in the next section.

2.3.3 Local minima

The phase space for $\vec{g}$ has almost as many dimensions as the parameter space, so each time a set of positions is tested in the algorithm, a random gradient vector is generated to be tested against. Since the ability of the algorithm to extract d_{false} is generally a function of the gradient vector, it is possible to randomly get a gradient that is easy to fit. When reported to Ferret, that set of positions would be unfairly weighted. Ferret has a setting that designates the test scenario as being noisy which mitigates this somewhat, but in order to prevent "accidental optimals" each set of positions is tested against at least 10 different gradients, and the fitness averaged. This prevents Ferret from being stuck in local minima, or wasting time trying positions that were only accidentally good. The limitation here is computation time. The field is already averaged over the volume of the Cs cell, these steps compound each other.

Figure 2-8 is the result of insufficient averaging. Ferret reported a fitness of 1.4×10^{-31}

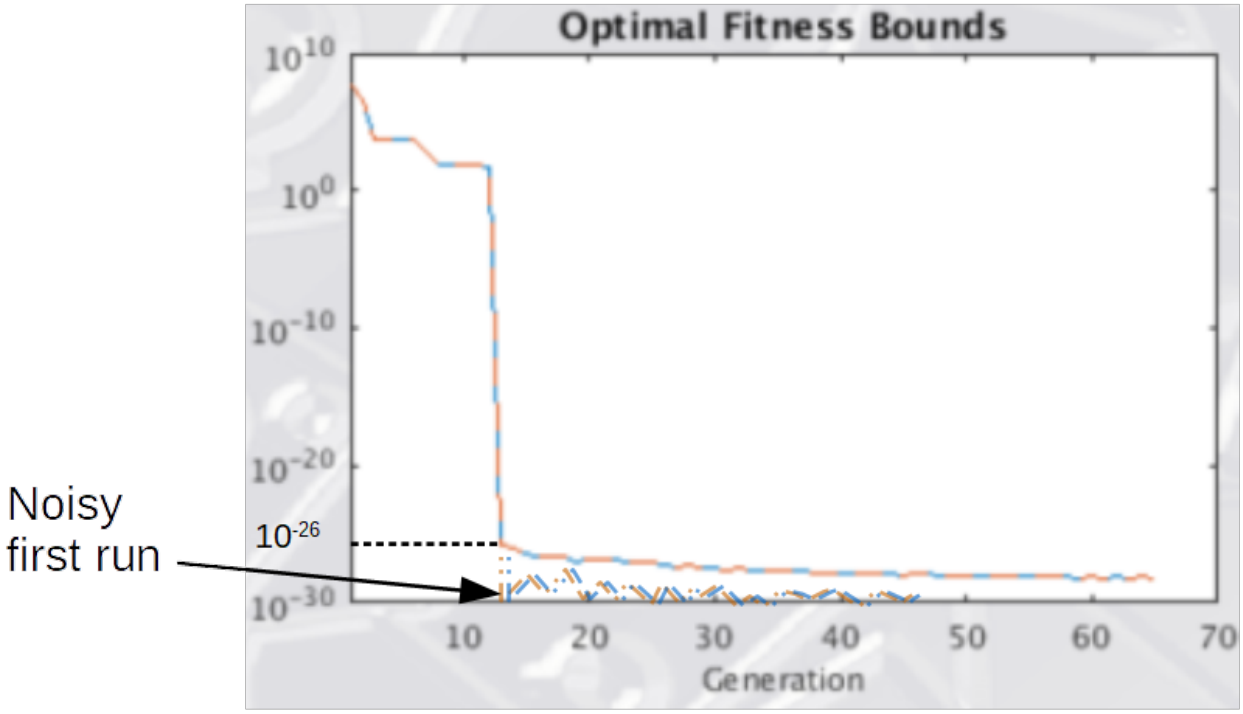

Figure 2-10: The history of the fitness found by ferret. This plot shows the best fitness value found at each generation for two different runs. The lower line (drawn in by hand) represents the run tested in figure 2-8, and the upper line is from figure 2-9.

for this set of positions, however the majority of tests done with that set have a larger error than this. This indicates that Ferret happened to test that position set on some easy gradients, and 1000 generations wasn't long enough for Ferret to re-test that set sufficiently.

Figure 2-9 shows the results of testing positions that were found using averaging. This set was tested with the same positioning and field sensing errors as the first one, the only difference being the extra step of averaging. A history of the fitness of this trial and the non-averaged trial are shown in figure 2-10. The fitness starts off very bad, as Ferret is randomly choosing points, some of which are penalized for being in a keep-out zone. As soon as none of the positions are being penalized, the non-averaged trial plummets to the 1×10^{-30} level immediately. This indicates that out of the 500 position sets in that generation, one of them got lucky with an easy to identify gradient. The averaged trial drops to around the 1×10^{-26}

level, consistent with the random placement result from figure 2-7. The non-averaged trial flounders in the 1×10^{-30} range, picking a different lucky position set each time, ending with a set of positions only an order of magnitude better than random. The averaged trial gradually gets better and better. Eventually, Ferret finds the actual noise floor of the system, and the fitness becomes noisy again. If this trial kept going, eventually Ferret would notice the lack of improvement, and either trigger a supermutation, or finish and find the optimal parameter set.

The fitness reported for this set was 3.4×10^{-29}, still well in the tail of the distribution shown in figure 2-9. However, a marked improvement is evident from the previous, non-averaged trial. Ferret will still tend to under-report the fitness, since out of the optimally performing parameter sets the ones that are tested on the easiest gradients will still have the best fitness. Increasing the averaging is the best way to decrease this mismatch, but at the cost of computational time. This is supported by figure 2-11, in which the reported fitness is even closer to the centre of the distribution. This run was done with 20 averaging steps instead of 10. This number can be increased as computing power allows.

2.3.4 Condition number

When numerically inverting a matrix, a quantity that is often useful is the condition number of the matrix. Very loosely, this describes the stability of the numerical calculation when the inputs are changed slightly. The condition number of the transformation matrix associated with each position set was calculated, listed in table 2.3. There is a clear trend, with lower condition numbers corresponding to better results. This makes sense, a more stable numerical calculation will lead to more accurate results.

With that in mind, the condition number was added as an objective to minimize for the Ferret runs. The result is a pareto-optimal set of solutions in the 2-D objective space. The condition number seems to drop as the error drops, until the fitness suddenly shoots up by

Table 2.3: The condition number of the transformation matrix associated with each set of positions.

Position set	Condition number
Symmetric layout 1	1.6×10^{22}
Symmetric layout 2	8.3×10^{21}
Random layout	2.8×10^{7}
Ferret 23 (Fig 2-8)	9.1×10^{4}
Ferret 24 (Fig 2-9)	4.3×10^{4}
Ferret 26 (Fig 2-11)	3.7×10^{4}

30 orders of magnitude. This indicates that in order to get a better condition number Ferret had to place sensors in a keep-out zone, so the huge jump in fitness is due to the penalty function kicking in. This is consistent with tests calculating the condition number of various position sets, when the positions were close to the origin (where the nEDM cell keepout zone is) it resulted in a lower condition number.

This study is consistent with Shomi Ahmed's thesis [5], where he found that a lower condition number was better in the context of active magnetic shielding, which uses a similar method of inverting a matrix to retrieve magnetic field information. However, it was possible to find solutions with poor condition numbers that still out-performed in the d_{false} extraction, so while the two seem closely correlated, ultimately the goal that should be focused on is the d_{false} extraction.

2.3.5 Simulation results and recommended requirements

The ultimate requirement on the determination of d_{false} has yet to be declared, but it will be on the order of 1×10^{-27}. If a set of parameters can determine d_{false} to within 5×10^{-28} with reasonable confidence, then I can declare those parameters to meet the requirements of the experiment for development purposes. Any result with error $\geq 5 \times 10^{-28}$ is a false report. When $d_{fit} > d_{sim}$ the result is called a false positive, and vice versa. Figure 2-12

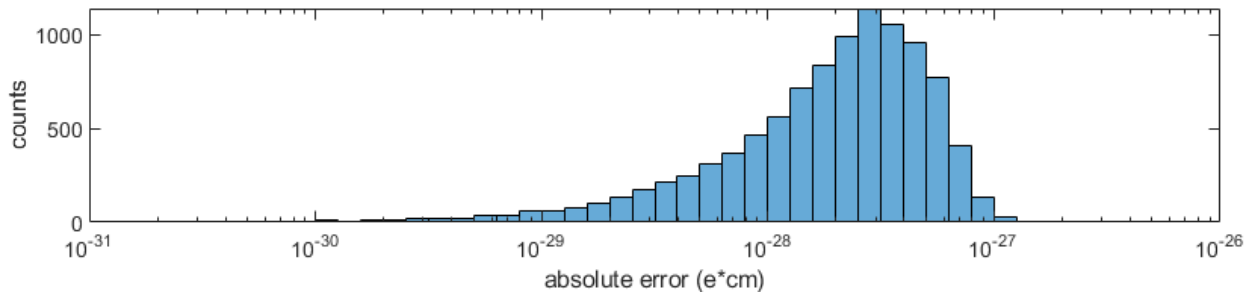

Figure 2-11: The last trial done during this phase of work. This set was reported with a fitness of 1.8×10^{-28}.

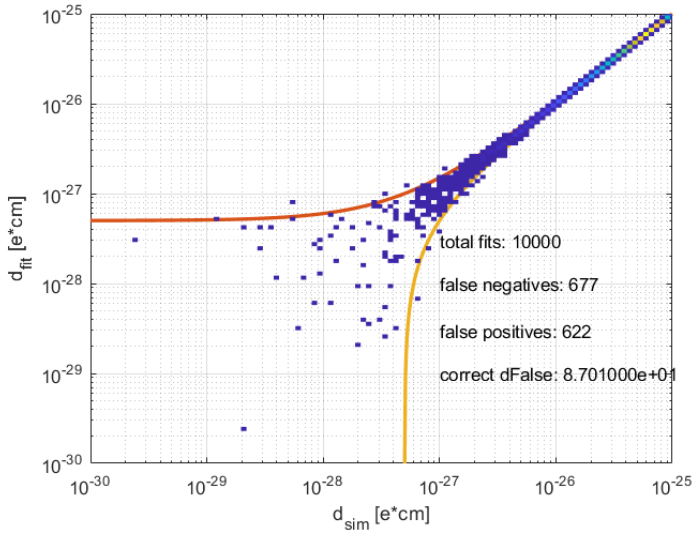

Figure 2-12: d_{sim} plotted against the recovered d_{fit}. The solid lines indicate $d_{fit} = d_{sim} \pm 5 \times 10^{-28}$ Anything outside the lines is a false report. 87% of fits were within 5×10^{-28} of the real answer.

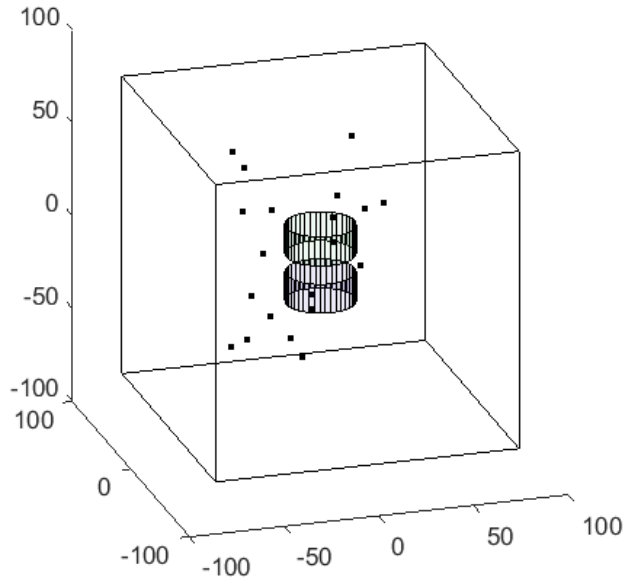

Figure 2-13: A 3D plot of the positions found by Ferret. No pattern is readily apparent, even though this set of positions outperforms our best parameterized set by 3-4 orders of magnitude.

plots d_{fit} against d_{sim}.

The values of the magnetometry parameters (sensitivity etc.) were adjusted until a noticeable effect was seen in the error histograms, giving us requirements for the magnetometers:

- **Number of sensors:** 20
- **Field sensing error:** 2 pT
- **Positioning error:** 0.1 cm
- **Cs cell radius:** No requirement
- **Cs cell height:** No requirement

2.4 Caveats and future implementation

This work has shown that this kind of system is viable, and demonstrates a method by which the placement of the magnetometers can be optimized to maximize accuracy. Since experimental design is ongoing in this project, the exact results of this work serve as a proof of concept, with final design left until the final requirements of all subsystems are specified.

2.4.1 Additional sources of error

So far all calculations assume equation 2.4 holds true. This is true if the source of the field is external to the magnetometry setup, but there are potential sources of magnetic flux that could lie within the radius of the magnetometers, violating this assumption. The central electrode providing the electric field could have leakage current, or there could be a speck of ferromagnetic dust stuck to a surface. Reference [3] calculates that a spherical speck of iron dust with a diameter of 20 microns magnetized to saturation corresponds to a dipole with magnetic moment $m_z = 10$ nA·m^2. The effect of these fields on this system has not been studied.

Another assumption is that the TUCAN MSR will perform similarly to the one I examined in this work. If the TUCAN shield has more or larger access holes cut into the metal, these may produce larger gradients than the current truncation allows for. A thorough study of these effects requires a finite element analysis of some kind, to determine what kind of field gradient is produced in the precession cells due to our MSR geometry.

During the final review of this work some algebra errors and typos were found in the fourth and fifth order magnetic field polynomials, both in their derivation and in the code. These were fixed and double checked thoroughly by myself and Maedeh Lavvaf, and against code written by my supervisor Dr. Martin. I was able to recreate all the critical results, but this illustrates the danger with using a black box solution like Ferret. The citations I provide to

other works that use evolutionary algorithms in a similar way lend credibility to this method, but extra care must be taken to make sure that results are genuine. Further studies using Ferret are planned that will study the effects of (deliberate or accidental) mis-placement of sensors, changing the keep-out zones, and integrating transverse field information into the algorithm.

Chapter 3

Operating principles of NMOR

3.1 Magneto-Optical Rotation

Faraday rotation [12], or linear magneto-optical rotation, is a mechanism by which the angle of polarization of light changes as it passes through a material subject to a magnetic field. This effect was seen to be particularly strong in sodium flames, leading to the discovery of the Macaluso-Corbino effect, or non-linear magneto-optical rotation (NMOR) [8]. This is a resonant effect found in the absorption spectra of alkali atoms.

My goal in this section is to establish the very basic quantum mechanical processes behind NMOR using a simple model, analogous to an alkali D2 transition. This calculation does not deal with doppler broadening, wall collision effects, antirelaxation coated cells, or some specific high power effects from the optical electric field such as Alignment-to-Orientation conversion or Bennet structure effects.

Starting with the Hamiltonian of an F=1 $\rightarrow$ F'=0 transition subject to linearly polarized light, I follow reference [6] through the rotating wave approximation to find a static Hamiltonian. The Liuoville equation is used to find the steady state density matrix elements, related to the population of atomic states and coherences. The optical polarization of a medium is

related to the properties of the electrons in the medium, as well as their distribution, so can be calculated from the density matrix. Observable signals, i.e. the effects of the medium on light passing through it, are calculated from the medium polarization. I specifically go over the results from [6] as they calculate the polarization rotation signal in the case of low power, and the first order nonlinear effect due to higher power. I then go over a more phenomenological description of the effect in the cesium atoms I use, and how resonances can be created away from zero field.

3.1.1 The rotating wave approximation

The density matrix for this 4-state system is written

$$\rho = \begin{pmatrix} \rho_{1,1} & \rho_{1,0} & \rho_{1,-1} & \rho_{1,0'} \\ \rho_{0,1} & \rho_{0,0} & \rho_{0,-1} & \rho_{0,0'} \\ \rho_{-1,1} & \rho_{-1,0} & \rho_{-1,-1} & \rho_{-1,0'} \\ \rho_{0',1} & \rho_{0',0} & \rho_{0',-1} & \rho_{0',0'} \end{pmatrix}, \tag{3.1}$$

which also shows the ordering of the states. Primed subscripts indicate the excited $F' = 0$ state.

The unperturbed Hamiltonian is

$$H_0 = \begin{pmatrix} 0 & 0 & 0 & 0 \\ 0 & 0 & 0 & 0 \\ 0 & 0 & 0 & 0 \\ 0 & 0 & 0 & \omega_0\hbar \end{pmatrix}, \tag{3.2}$$

where ω_0 is the frequency of the transition. Light linearly polarized in the x direction can

be written

$$\vec{\varepsilon} = \varepsilon_0 \cos(\omega t)\hat{x}, \tag{3.3}$$

with the interaction Hamiltonian

$$H_\ell = -\vec{\varepsilon} \cdot \vec{d} = -\varepsilon_0 \cos(\omega t) d_x, \tag{3.4}$$

where $\vec{d}$ is the dipole operator. Since I want to make the rotating wave approximation, I write the x-component of $\vec{d}$ in the circular polarization basis as an equal admixture of RHCP (right-hand circularily polarized) and LHCP (left-hand) light:

$$H_\ell = \frac{-1}{\sqrt{2}}(d_{-1} - d_{+1})\varepsilon_0 \cos(\omega t). \tag{3.5}$$

$d_{\pm 1}$ can be written using the Wigner-Eckart theorem:

$$\langle \xi_1 F_1 m_1 | \, d_{\pm 1} \, | \xi_2 F_2 m_2 \rangle = (-1)^{F_1 - m_1} \langle \xi_1 F_1 || d || \xi_2 F_2 \rangle \begin{pmatrix} F_1 & 1 & F_2 \\ -m_1 & \pm 1 & m_2 \end{pmatrix} \tag{3.6}$$

with the reduced matrix element $\langle \xi_1 F_1 || d || \xi_2 F_2 \rangle$, and using a Wigner 3j symbol. ξ represents additional quantum numbers independent of angular terms. The 3j symbols can be calculated explicitly [34], or using a 3j symbol calculator (`http://www-stone.ch.cam.ac.uk/wigner.shtml` maintained by Anthony Stone).

The block diagonal elements are zero due to parity selection rules forbidding $\Delta J = 0$ transitions. For an example, the $J = 1, m = 1$ to $J' = 0, m' = 0$ element evaluates as

$$(-1)^{1-1} \begin{pmatrix} 1 & 1 & 0 \\ -1 & 1 & 0 \end{pmatrix} = \sqrt{\frac{1}{3}} \tag{3.7}$$

and the $0, 0'$ element is

$$(-1)^{1-0} \begin{pmatrix} 1 & 1 & 0 \\ 0 & 1 & 0 \end{pmatrix} = 0. \tag{3.8}$$

Continuing for the entire matrix:

$$d_{-1} = \frac{\langle \xi 1 || d || \xi' 0' \rangle}{\sqrt{3}} \begin{pmatrix} 0 & 0 & 0 & 0 \\ 0 & 0 & 0 & 0 \\ 0 & 0 & 0 & 1 \\ -1 & 0 & 0 & 0 \end{pmatrix} \tag{3.9}$$

and

$$d_1 = \frac{\langle \xi 1 || d || \xi' 0' \rangle}{\sqrt{3}} \begin{pmatrix} 0 & 0 & 0 & 1 \\ 0 & 0 & 0 & 0 \\ 0 & 0 & 0 & 0 \\ 0 & 0 & -1 & 0 \end{pmatrix}. \tag{3.10}$$

For H_ℓ, then,

$$H_\ell = \frac{\hbar \Omega_R \cos(\omega t)}{\sqrt{2}} \begin{pmatrix} 0 & 0 & 0 & 1 \\ 0 & 0 & 0 & 0 \\ 0 & 0 & 0 & -1 \\ 1 & 0 & -1 & 0 \end{pmatrix} \tag{3.11}$$

where $\Omega_R = \langle \xi 1 || d || \xi' 0' \rangle \frac{\xi_0}{\hbar\sqrt{3}}$ is the optical Rabi frequency.

The magnetic field interacts with the $m = \pm 1$ states, giving them energy equal to $\hbar\Omega_L$

where Ω_L is the Larmor frequency. The magnetic field interaction Hamiltonian is

$$H_B = \hbar\Omega_L \begin{pmatrix} 1 & 0 & 0 & 0 \\ 0 & 0 & 0 & 0 \\ 0 & 0 & -1 & 0 \\ 0 & 0 & 0 & 0 \end{pmatrix}. \tag{3.12}$$

The total interaction Hamiltonian is

$$H = H_0 + H_\ell + H_B = \hbar \begin{pmatrix} \Omega_L & 0 & 0 & \frac{1}{\sqrt{2}}\Omega_R \cos(\omega t) \\ 0 & 0 & 0 & 0 \\ 0 & 0 & -\Omega_L & -\frac{1}{\sqrt{2}}\Omega_R \cos(\omega t) \\ \frac{1}{\sqrt{2}}\Omega_R \cos(\omega t) & 0 & -\frac{1}{\sqrt{2}}\Omega_R \cos(\omega t) & \omega_0 \end{pmatrix}. \tag{3.13}$$

In the rotating wave approximation, the Hamiltonian is transformed into:

$$\widetilde{H} = U^\dagger H U - \hbar A \tag{3.14}$$

where U is the rotation matrix given by

$$U = e^{-iAt} \tag{3.15}$$

and

$$A = \begin{pmatrix} 0 & 0 & 0 & 0 \\ 0 & 0 & 0 & 0 \\ 0 & 0 & 0 & 0 \\ 0 & 0 & 0 & \omega \end{pmatrix} \tag{3.16}$$

where ω is the frequency of the optical field. $U^\dagger H U$ transforms into the rotating frame, and

the $\hbar A$ term is analogous to a coriolis force in the rotating frame. The form of equation 3.14 is derived in many quantum mechanics textbooks [6].

Writing $\cos(\omega t)$ as $\frac{1}{2}\{e^{i\omega t} + e^{-i\omega t}\}$ the rotating frame Hamiltonian is then

$$\widetilde{H} = \hbar \begin{pmatrix} \Omega_L & 0 & 0 & \frac{\Omega_R}{2\sqrt{2}}\left(1 - e^{-2i\omega t}\right) \\ 0 & 0 & 0 & 0 \\ 0 & 0 & -\Omega_L & \frac{-\Omega_R}{2\sqrt{2}}\left(1 - e^{-2i\omega t}\right) \\ \frac{\Omega_R}{2\sqrt{2}}\left(1 - e^{2i\omega t}\right) & 0 & \frac{-\Omega_R}{2\sqrt{2}}\left(1 - e^{2i\omega t}\right) & \omega_0 - \omega \end{pmatrix} \tag{3.17}$$

The main assumption in the rotating wave approximation is that the exponential term integrates away over the relevant timescales when ω is much larger than the natural transition width, leaving a static Hamiltonian:

$$\widetilde{H} \approx \hbar \begin{pmatrix} \Omega_L & 0 & 0 & \frac{\Omega_R}{2\sqrt{2}} \\ 0 & 0 & 0 & 0 \\ 0 & 0 & -\Omega_L & \frac{-\Omega_R}{2\sqrt{2}} \\ \frac{\Omega_R}{2\sqrt{2}} & 0 & \frac{-\Omega_R}{2\sqrt{2}} & -\Delta \end{pmatrix} \tag{3.18}$$

with $\Delta = \omega - \omega_0$.

The density matrix must also be solved in the rotating frame, but observables are seen in the lab frame. The lab frame density matrix is written in terms of the rotating frame matrix elements:

$$\rho = U\widetilde{\rho}U^{\dagger} = \begin{pmatrix} \tilde{\rho}_{1,1} & \tilde{\rho}_{1,0} & \tilde{\rho}_{1,-1} & e^{i\omega t}\tilde{\rho}_{1,0'} \\ \tilde{\rho}_{0,1} & \tilde{\rho}_{0,0} & \tilde{\rho}_{0,-1} & e^{i\omega t}\tilde{\rho}_{0,0'} \\ \tilde{\rho}_{-1,1} & \tilde{\rho}_{-1,0} & \tilde{\rho}_{-1,-1} & e^{i\omega t}\tilde{\rho}_{-1,0'} \\ e^{-i\omega t}\tilde{\rho}_{0',1} & e^{-i\omega t}\tilde{\rho}_{0',0} & e^{-i\omega t}\tilde{\rho}_{0',-1} & \tilde{\rho}_{0',0'} \end{pmatrix} \tag{3.19}$$

3.1.2 The quantum Liouville equation

Just as the time evolution of a wavefunction is connected to the static Hamiltonian via the Schrödinger equation, the time evolution of the density matrix is connected to the static Hamiltonian via the quantum Liouville equation.

The equation is

$$i\hbar\frac{d}{dt}\tilde{\rho} = [\hat{H}, \tilde{\rho}]. \tag{3.20}$$

However, this form of the Liouville equation assumes the atoms never leave the light field. In a real experiment the laser has a finite width, so atoms transit the beam in time $\frac{1}{\gamma}$, meaning an effective relaxation rate of γ. This relaxation can be modelled with an additional $\frac{d\rho}{dt}$ term given by

$$\left.\frac{d\rho}{dt}\right|_{relax} = -\frac{1}{2}(\hat{\Gamma}\rho + \rho\hat{\Gamma}) \tag{3.21}$$

where $\hat{\Gamma}$ is a diagonal matrix whose values are the relaxation rates of the basis states. The excited state also relaxes with a rate Γ, so $\hat{\Gamma}$ is

$$\hat{\Gamma} = \begin{pmatrix} \gamma & 0 & 0 & 0 \\ 0 & \gamma & 0 & 0 \\ 0 & 0 & \gamma & 0 \\ 0 & 0 & 0 & \gamma + \Gamma \end{pmatrix}. \tag{3.22}$$

The experiment is in an enclosed container, so as atoms leave the beam they also re-enter it. In this simple model polarization is not maintained after the atoms leave the light field, so atoms re-enter each basis state equally. They also only enter the ground states, the assumption here is that the excited state decay rate is much faster than the beam transit rate. For each atom that leaves a polarized state with rate γ, it re-enters the other three

with rate $\gamma/3$. The repopulation matrix looks like

$$\begin{pmatrix} \frac{\gamma}{3} & 0 & 0 & 0 \\ 0 & \frac{\gamma}{3} & 0 & 0 \\ 0 & 0 & \frac{\gamma}{3} & 0 \\ 0 & 0 & 0 & 0 \end{pmatrix}. \tag{3.23}$$

In addition to stray atoms re-entering the beam, these states are also populated in the same uniform way by the decay of the excited state. This rate depends on the population of the excited state, so the repopulation rate due to this decay is $\Gamma\tilde{\rho}_{0',0'}$, where Γ is the decay rate of the excited state from the relaxation matrix. The full repopulation matrix is then:

$$\left.\frac{d\rho}{dt}\right|_{repop} = \Lambda = (\gamma + \Gamma\rho_{0',0'}) \begin{pmatrix} \frac{1}{3} & 0 & 0 & 0 \\ 0 & \frac{1}{3} & 0 & 0 \\ 0 & 0 & \frac{1}{3} & 0 \\ 0 & 0 & 0 & 0 \end{pmatrix}. \tag{3.24}$$

The complete quantum Liouville equation is

$$i\hbar\frac{d}{dt}\tilde{\rho} = [\tilde{H}, \tilde{\rho}] - i\hbar\frac{1}{2}(\hat{\Gamma}\tilde{\rho} + \tilde{\rho}\hat{\Gamma}) + i\hbar\Lambda \tag{3.25}$$

The quantum mechanics is now done. The steady state solution of the density matrix is found by setting the time derivatives in equation 3.25 equal to zero, and solving the resulting set of linear equations. I highlight the important terms for my work in this chapter. These solutions are taken from reference [6], who in turn utilized a computer algebra system to solve the equations. A single simplifying assumption is that the excited state decay rate is much faster than the beam transit time, a reasonable assumption for a physical laser beam.

The two elements I require for my analysis are

$$\tilde{\rho}_{1,0'} = \frac{\sqrt{2\gamma\Gamma\kappa}}{D}\{8\Omega_L^2[2(\Omega_L+\Delta)+i\Gamma][8(\Delta-\Omega_L)^2+\Gamma^2(\kappa+2)] - 2\gamma\Gamma^2\kappa\Omega_L[\Gamma(\kappa+2)-4i\Delta] + \gamma^2(2\Delta+i\Gamma)[-8i\Gamma\Omega_L+16\Delta(\Delta-\Omega_L)+\Gamma^2(\kappa+2)^2]\} \quad (3.26)$$

and

$$\tilde{\rho}_{-1,0'} = \frac{\sqrt{2\gamma\Gamma\kappa}}{D}\{-2\gamma\Gamma^2\kappa\Omega_L[\Gamma(\kappa+2)-4i\Delta]-i\gamma^2(\Gamma-2i\Delta)[8i\Gamma\Omega_L+16\Delta(\Omega_L+\Delta)+\Gamma^2(\kappa+2)^2] + 8\Omega_L^2(2\Omega_L-i\Gamma-2\Delta)[8(\Omega_L+\Delta)^2+\Gamma^2(\kappa+2)]\}, \quad (3.27)$$

where D is

$$D = 8\Omega_L^2\left[32\Gamma^2(\kappa+3)(\Omega_L^2+\Delta^2)+192(\Delta^2-\Omega_L^2)^2+\Gamma^4(\kappa+2)(\kappa+6)\right] + 2\gamma^2[\Gamma^2(\kappa+2)^2+16\Delta^2][\Gamma^2(2\kappa+3)+12\Delta^2], \quad (3.28)$$

and $\kappa = \Omega_R^2/(\Gamma\gamma)$ is called the optical pumping saturation parameter. It parameterizes the strength of the optical field with respect to the strength of the atomic transitions. This will be the term that allows us to distinguish the linear and non-linear effects.

3.1.3 Optical polarization of the medium

The expectation value of the optical polarization of a medium is

$$\mathbf{P} = n\mathrm{Tr}\rho\mathbf{d} = n\mathrm{Re}\left(\sqrt{\frac{2}{3}}\langle\xi 1||d||\xi' 0'\rangle\, e^{-i\omega t}\left[(\tilde{\rho}_{0',-1}-\tilde{\rho}_{0',1})\tilde{\mathbf{x}}+i(\tilde{\rho}_{0',-1}+\tilde{\rho}_{0',1})\tilde{\mathbf{y}}+\sqrt{2}\tilde{\rho}_{0',0}\tilde{\mathbf{z}}\right]\right) \quad (3.29)$$

Where n is the number density of atoms interacting with the light, and Tr is the trace operator. Given this equation, it is convenient to parameterize the polarization in terms of in phase and quadrature components:

$$\mathbf{P} = \mathrm{Re}\{e^{i(\mathbf{k}\cdot\mathbf{r}-\omega t+\phi)}[(P_1 - iP_2)\tilde{\mathbf{e}}_\mathbf{1} + (P_3 - iP_4)\tilde{\mathbf{e}}_\mathbf{2}]\} \tag{3.30}$$

The parameter I am interested in is the optical rotation α, which is found in the $\alpha - \epsilon$ parametrization of the incoming light field. I won't go over solving the wave equation, but the following result [6] is useful:

$$\frac{d\alpha}{d\ell} = \frac{2\pi\omega}{\epsilon_0 c} P_4. \tag{3.31}$$

Identifying that $\tilde{\rho}_{0',0} = 0$, $\tilde{\mathbf{e}}_\mathbf{1} = \tilde{\mathbf{x}}$, and $\tilde{\mathbf{e}}_\mathbf{2} = \tilde{\mathbf{y}}$, comparing equations (3.29) and (3.30) it can be shown that

$$P_4 = -\sqrt{\frac{2}{3}}\,\langle \xi 1||d||\xi' 0'\rangle\, n\mathrm{Re}(\tilde{\rho}_{-1,0'} + \tilde{\rho}_{1,0'}). \tag{3.32}$$

At last we have an equation relating the optical rotation to the density matrix elements:

$$\frac{d\alpha}{d\ell} = -\frac{n\Gamma\lambda^2 \mathrm{Re}(\tilde{\rho}_{-1,0'} + \tilde{\rho}_{1,0})}{4\sqrt{2\pi\Omega_R}}, \tag{3.33}$$

where the reduced matrix element is related to the lifetime of the excited state by [34]

$$\Gamma = |\langle \xi' F'||d||\xi F\rangle|^2 \frac{1}{2F'+1}\frac{4\omega_0^3}{3\hbar c^3}. \tag{3.34}$$

The polarization rotation is given by

$$\ell_0 \frac{d\alpha}{d\ell} = -\frac{6\Gamma\Omega_L}{D}\{8\Omega_L^2[8\Omega_L^2 + \Gamma^2(\kappa+2) - 8\Delta^2] + \gamma[4\gamma(\Gamma^2 - 4\Delta^2) - \Gamma^3\kappa(\kappa+2)]\}, \tag{3.35}$$

where D is again given by equation 3.28, and $\ell_0 = 6\pi/\lambda^2 n$ is the unsaturated absorption

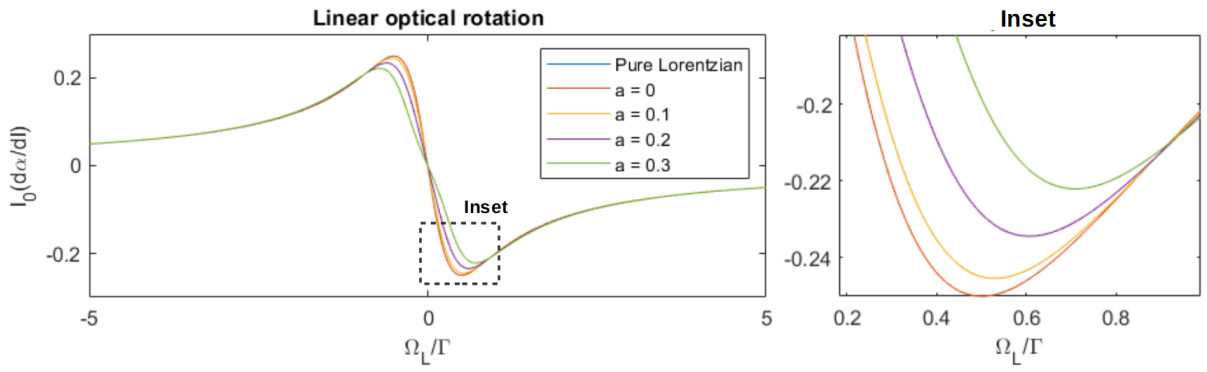

Figure 3-1: The linear optical rotation signal is shown along with a pure absorptive Lorentzian. The Lorentzian lies exactly under the a = 0 case. The normalization means the characteristic width of the linear effect is Γ, the lifetime of the excited state.

length on resonance. This is found when $\kappa = \Omega_L = \Delta = 0$.

3.1.4 The linear effect

The linear effect is found by taking $\kappa = 0$. For optical rotation:

$$\ell_0 \frac{d\alpha}{d\ell} = -\frac{\Gamma\Omega_L(4\Omega_L^2 - 4\Delta^2 + \Gamma^2)}{16(\Delta^2 - \Omega_L)^2 + 8\Gamma^2(\Delta^2 + \Omega_L^2) + \Gamma^4}. \tag{3.36}$$

Fixing the detuning at $\Delta = a \cdot \Gamma$, and writing as a function of $\beta = \Omega_L/\Gamma$,

$$\ell_0 \frac{d\alpha}{d\ell} - \frac{\beta(4\beta^2 - 4a^2 + 1)}{16(a^2 - \beta^2)^2 + 8(a^2 + \beta^2) + 1}. \tag{3.37}$$

A plot of this function is in figure 3-1. For small values of a (that is, small values of frequency detuning), the optical rotation is a dispersive Lorenztian with width Γ. The approximately linear response near zero field is Faraday rotation.

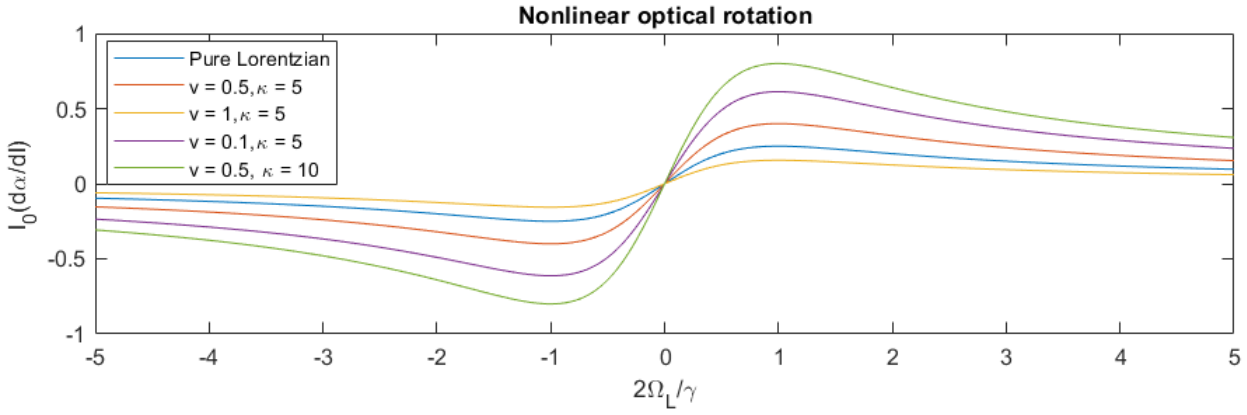

Figure 3-2: The nonlinear rotation signal, shown with several values of $v = 2\Delta/\Gamma$ and κ. A dispersive Lorentzian is also shown, plotted with width = 2. From the normalization of the horizontal axis, it is clear that the characteristic width of the NMOR shape is given by γ.

3.1.5 The nonlinear effect

The non-linear effects happen when κ is non-zero. It is useful to define $u = 2\Omega_L/\gamma$ and $v = 2\Delta/\Gamma$ [6], both of which are of order unity in the non-linear regime. Under this assumption, and the previous assumption that $\gamma \ll \Gamma$, the optical rotation signal is [6]

$$\ell_0 \frac{d\alpha}{d\ell} = \frac{1}{8} \frac{u\kappa(\kappa+2)}{u^2(v^2+1+\frac{\kappa}{2})(v^2+1+\frac{\kappa}{6}) + (v^2+1+\frac{2\kappa}{3})(v^2+(1+\frac{\kappa}{2})^2)}. \tag{3.38}$$

To make this clearer, I can expand to first order in κ, giving

$$\ell_0 \frac{d\alpha}{d\ell} = \frac{u\kappa}{4(u^2+1)(v^2+1)^2} + \mathcal{O}(\kappa^2)... \tag{3.39}$$

This function is shown in figure 3-2. The shape is a dispersive Lorentzian with characteristic width = γ for any reasonable value of Δ or κ. This is consistent with the common approximation for NMOR used in Moushumi Das' thesis [10]:

$$\ell_0 \cdot d\alpha = \frac{(2g\mu B)/(\hbar\gamma)}{(1+((2g\mu B)/(\hbar\gamma))^2)} d\ell. \tag{3.40}$$

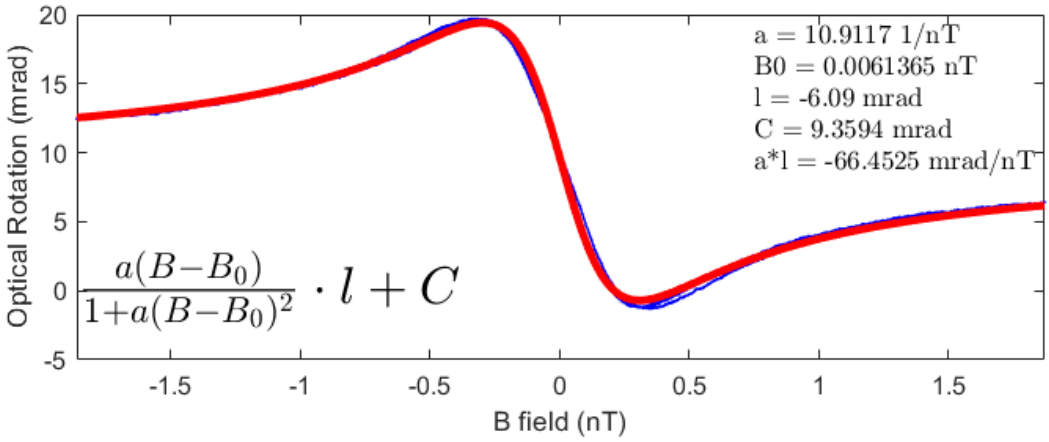

Figure 3-3: An example zero field resonance in Cs. Equation 3.40 is used to fit the data. This signal has been maximized for field sensitivity. Vertical units are millirads (see section 4).

3.2 NMOR in Cs

Moving from this idealized analog to a real system, it is useful to describe NMOR in more qualitative terms. There is an intuitive classical interpretation [6] of the dispersive Lorentzian in equation 3.40, similar to the classical interpretation of the Hanle effect, a related phenomena, found in [26]. NMOR becomes a three step process, explicitly showing why this is a non-linear phenomenon. Roughly, these steps can be called the *pump*, *precess*, and *probe* stages. At zero field, these happen continuously and simultaneously, but it will be handy later on to think of them as discrete steps happening in order, as a representative atom in the ensemble might experience. This model is referred to as the "rotating polarizer model" in optical magnetometry [6].

In the pump stage, the atoms are prepared by the laser into a particular state. Since equations 3.39 and 3.40 use the lifetime of the ground state, the atoms are in a polarized ground state. This polarized state starts out completely dark to the pump light, as the interacting states have been depleted from the laser. This process is “optical pumping”, the bulk rearrangement of atomic states due to light interaction. Since the interacting states are

being excited by linearly polarized light, the dark state only interacts with the orthogonal linear polarization state of light. These atoms can be said to be optically polarized.

In the precession stage, the polarized atoms precess in the magnetic field. The stronger the field the faster the atoms precess, so the further around they get before the next interaction with the laser light.

In the probe stage, the laser light interacts with the now rotated atoms. They used to be completely dark to the light, but as they precess their angle of polarization precesses with them. The further they rotate, the more they will interact with the incoming light. This leads to the polarization being rotated in the same direction as the atoms. As the field strength increases, the rotation is larger and larger, reaching a maximum as the atoms precess all the way around. As they precess further, the effect starts to average itself out as some atoms go slightly faster than others, and the rotation signal drops back down to zero. The atoms precess the other way in a magnetic field of the opposite sign, explaining the symmetry of the function.

Figure 3-3 was the most sensitive resonance with respect to magnetic field, recorded near zero field. This is the most sensitive this technique can be, parameterized by $a \cdot l$, in units of V/nT. The best value for $a \cdot l$ was around 0.5. A reasonable signal variance of 0.5 mV would allow for single-shot measurements with a variance of less than 1 pT.

3.2.1 Amplitude Modulated (AM) NMOR

So far the resonances examined have been at or near zero field (when u in equation 3.39 is of order unity), but the TUCAN nEDM experiment has a background field of 1 μT. In order to create resonances at this high field value we must modify the technique we use.

A single Cs atom in such a high field would, when polarized, precess at its Larmour frequency. In principle, measuring this frequency would be a direct (and absolute) measure of the magnetic field strength, since the Larmour frequency of cesium is very well known.

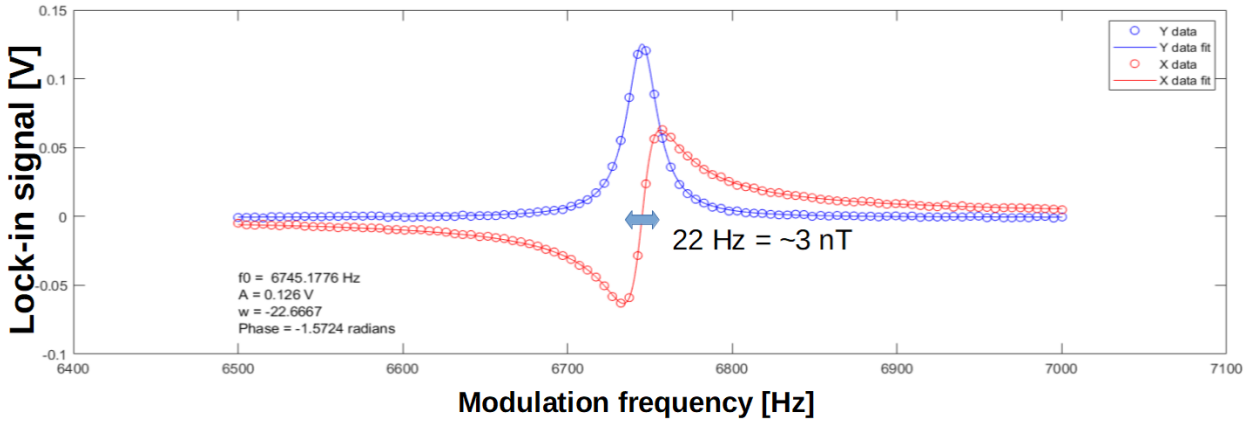

Figure 3-4: A forced oscillation scan, demonstrating AM NMOR. The central frequency is the Larmour frequency of Cs in approx. 1 μT.

At zero field, the rotation is a property of the average amount of rotation each atom goes through *starting from zero phase*. If we imagine the atoms precessing very fast, the phase of the atoms in the system quickly becomes decoherent, and the average rotation is identically zero. In order to keep the atoms coherent, two lasers are now needed.

A short, strong pulse of polarized light would create a small population of atoms all in phase with each other. Just as in the zero field case, these atoms quickly start to decohere. If we want to keep these atoms in phase, another pulse of light is needed. After a full period of precession (what we might call a Larmour period T_L), a pulse of polarized light will again create a population of atoms, this time in phase with the existing atoms. As this amplitude modulation (AM) continues, a coherent population of precessing atoms is built up, all precessing at their Larmour frequency.

A second, much weaker laser beam is then passed through this medium. This beam probes the precessing atoms, having its polarization rotation modulated periodically as the atoms go from dark to bright states as they precess. The frequency of this modulation is the measurement of the magnetic field. This is typically detected with a lock-in amplifier.

In fact modulation can be done at twice the Larmour frequency, since this atomic state has twofold symmetry. This fact is less obvious in this derivation, but can be seen by

examining the angular momentum probability surface associated with the density matrix [6].

In reality, this method would require precisely knowing the Larmour frequency ahead of time, which defeats the purpose. In a practical application, the frequency of the pulsed probe beam is swept through resonance with the atoms, and the central frequency found. An example of this is seen in figure 3-4. The in-phase signal from the lock-in amplifier is in red, and shows the characteristic dispersive Lorentzian shape. This fit function is discussed in detail in section 5.1.2. A final modification must be made to our technique before single shot in-situ magnetic field measurements can be made.

3.2.2 Free Induction Decay (FID) NMOR

Once a large coherent population of atoms has been built up, we take advantage of the long lifetime of the ground state, as well as an anti-relaxation coating in the vapour cell (see section 4.1.5) which further lengthens the lifetime of the atomic state. If we shut off the probe beam, the atoms will continue to precess until wall collisions and spin-exchange collisions deplete the polarized state. For as long as this takes, we can probe the atoms as they are solely influenced by the magnetic field itself, not the pump beam. This technique gets its name from the characteristic decay signal that results, a free induction decay (FID) signal.

This is the technique I use in this system. Figure 3-5 shows an example FID signal. Section 5.1.2 goes over the optimization process for obtaining the best signal. In even the most simple model case, equation 3.38 is a complicated function of detuning, optical pumping power, and magnetic field. The addition of Doppler broadening, anti-relaxation coating, and further nonlinear effects means the best way to optimize the signal is experimentally, using the precision of the extracted frequency as the figure of merit. The next chapters describe the equipment required to perform these frequency measurements and the optimization process.

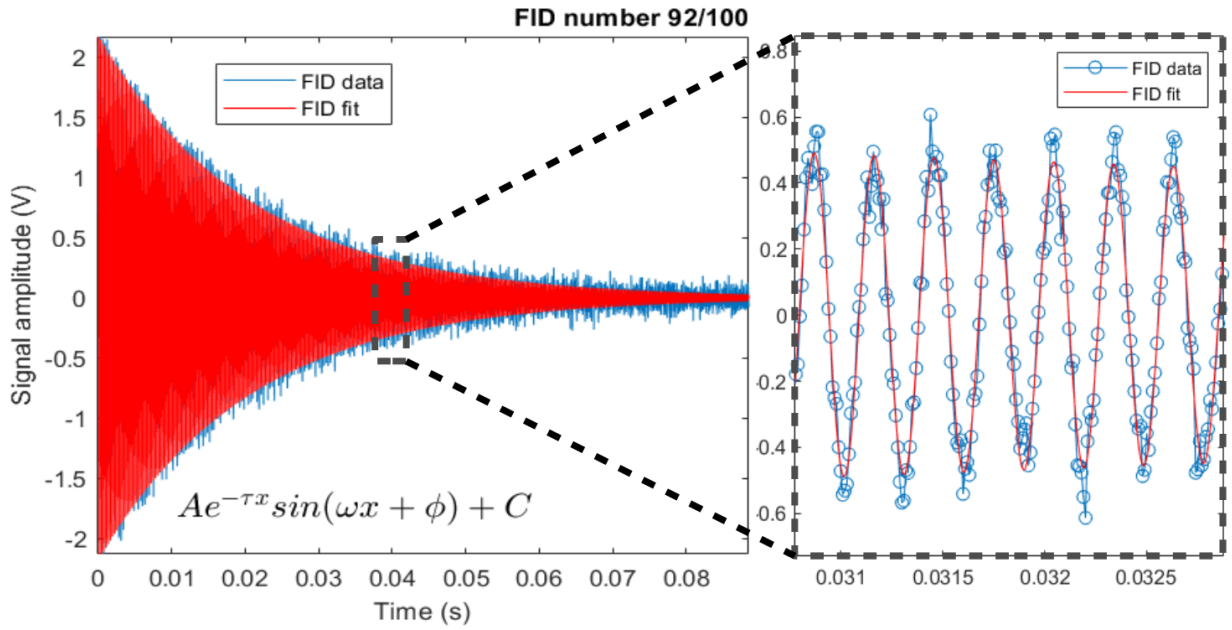

Figure 3-5: A free induction decay (FID) signal. The signal is 10 ms long in total, the pump period is cut out of this graph for the sake of fitting the decaying signal. The function is shown as well.

Chapter 4

Experimental setup

This chapter details the setup and calibration of the apparatus required to execute and record FID measurements at the University of Winnipeg.

4.1 Optics

4.1.1 The laser table

The optics in this project are mounted to a Newport RS 2000 optics table, which has the option to float on pneumatic legs to isolate the table from vibration. The basic layout is shown in figure 4-1. There is a main laser beam running along one side of the table, secondary beams are split off with beamsplitters, microscope slides in this case. The main beam first goes through a Thorlabs model IO-3D-850-VLP free space isolator, to prevent reflections propagating back to the diode, potentially causing harm/interference. The beam leaves this device linearly polarized at 45°. The beam is sent directly into a dump after all other beams are split off, for safety.

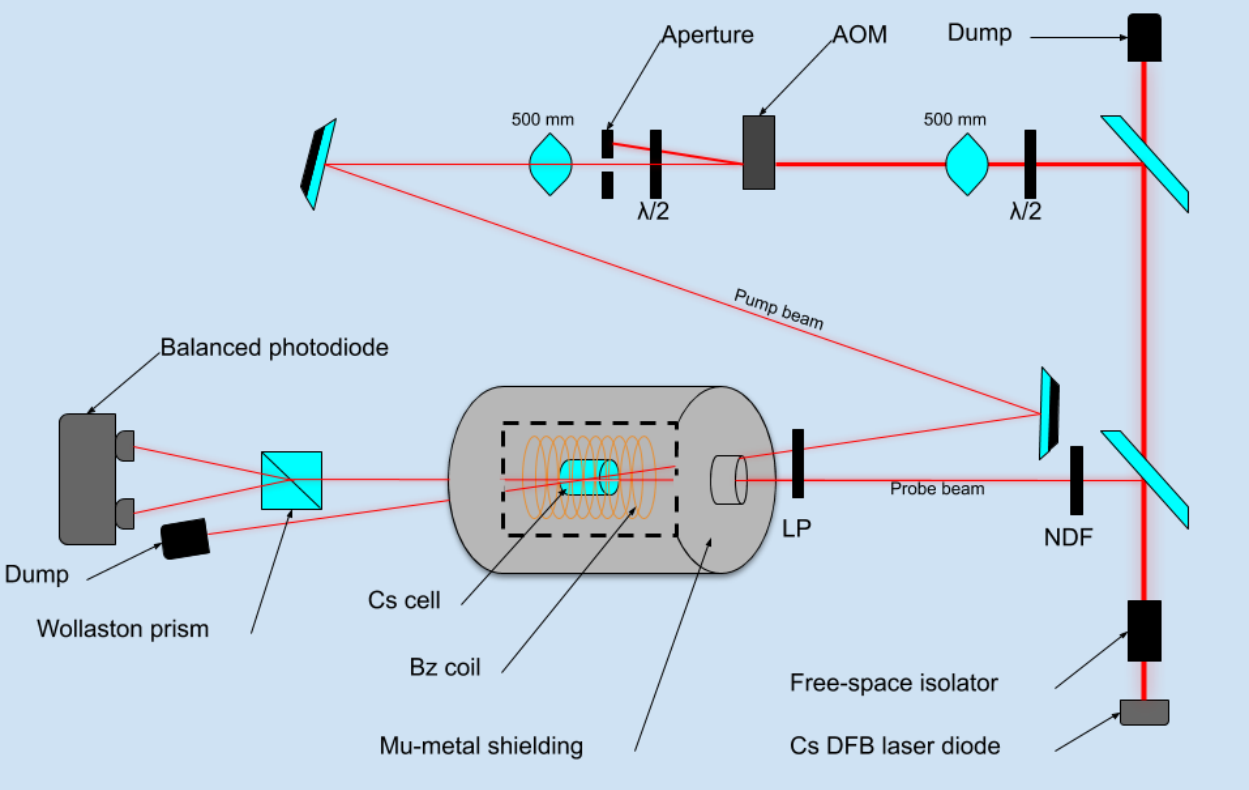

Figure 4-1: A schematic view of the laser table, set up to perform FID NMOR measurements. Angles are exaggerated for illustrative purposes.

4.1.2 The laser

This magnetometry setup uses an Eagleyard model EYP-DFB-0852-00150-1500-TOC03-0005 distributed feedback (DFB) laser diode, designed to excite the Cs D2 transition at 852 nm with a linewidth of 0.6 MHz. Rather than an optical cavity as in a Fabry-Perot style laser, the active volume in a DFB laser is a diffraction grating. This means that a very narrow selection of wavelengths can satisfy the conditions for lasing, resulting in a very narrow, very stable linewidth from this kind of laser.

This laser has two control inputs: the current going to the diode, and the temperature of the diode. The primary method of changing the frequency of a DFB laser is by adjusting the temperature, and therefore the spacing of the grating. Adjusting the current also can tune the frequency of the laser, and adjust its power output. In general the power and frequency

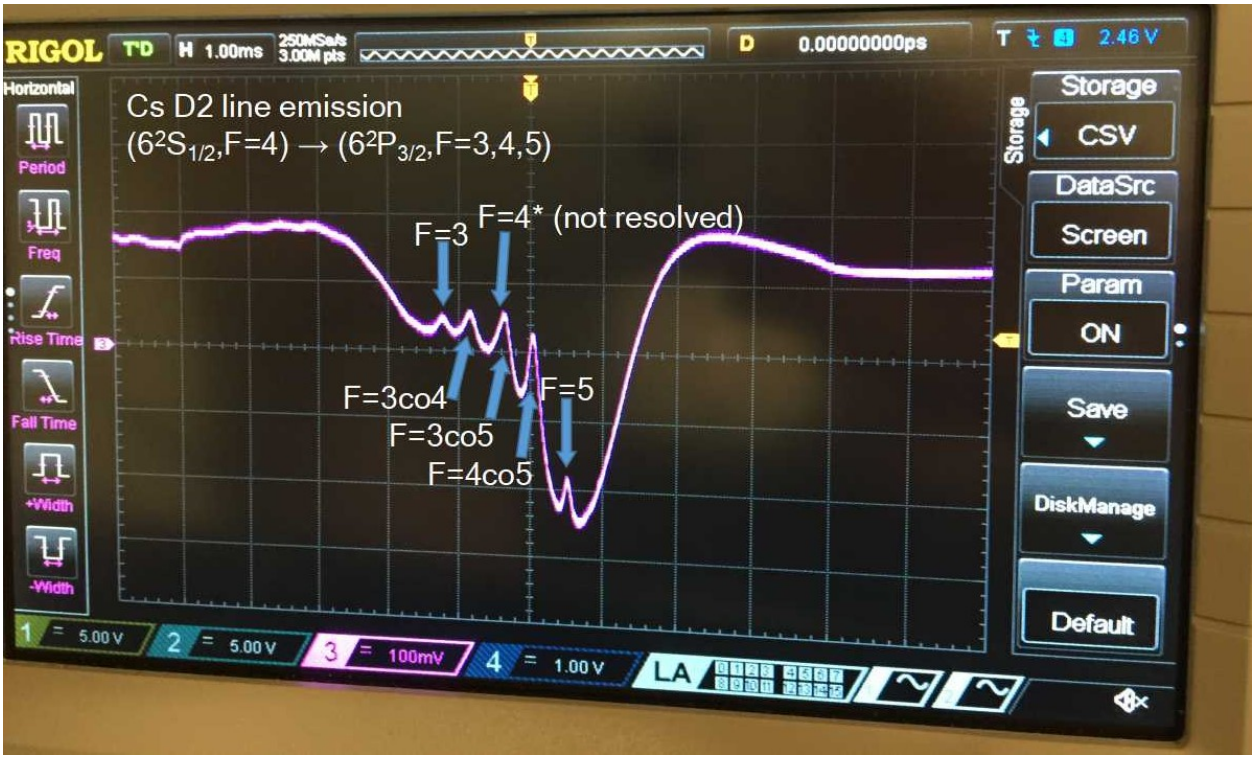

Figure 4-2: Doppler-free absorption spectroscopy confirms that this system is at the $6^2P_{\frac{1}{2}} \rightarrow 6^2P_{\frac{3}{2}}$ transition line.

of the laser are coupled. Setting a fixed temperature before tuning using the current results in a very small power dependence in the region of the Cs resonance. The dials on the lasers current control module are extremely sensitive, so a triple-channel Keithley power supply (PS) is connected to the mod-in port on the current supply. The Keithley PS allows much finer control for tuning.

This style of laser is very stable, with no mode hopping, but there are still some long term drifts when the laser is warming up. Generally the laser was left on overnight before taking any data, this is enough to reach a steady state. The drifts are on the order of the natural linewidth of the Cs D2 line over the course of an hour. The tune can be "locked" using a dichroic atomic vapour laser lock (DAVLL) system, but the laser is stable enough not to require one at the development stage. The final system will require a DAVLL system

to operate reliably. Moushumi Das' thesis work [10] uses a DAVLL system very similar to the one that will be used in this final system. Figure 4-2 shows saturated absorption spectroscopy done with the laser, confirming that it is indeed spectroscopy quality and that we are near the correct frequency.

4.1.3 The probe beam and balanced polarimetry

The probe beam is the first to be split off from the main beam. It passes through a series of neutral density filters until it is at the desired intensity (5-7 μW). It then passes through a polarizing film, set to polarize the light at 45° with respect to the surface of the table. The polarizer was verified to be at 45° with a Wollaston polarizing beam splitter. A Wollaston polarizing beam splitter splits the beam into it's vertical and horizontal polarization components, which are collected and measured by the two photodiodes on the New Focus 2307 balanced photodiode. The angle was chosen as it results in two beams of equal intensity on the diodes, which makes the differenced output zero. The difference signal is proportional to the rotation of the angle of the plane of polarization of the beam. To see this, take the total intensity as the sum of the two polarization components:

$$I_0 = I_x + I_y, \tag{4.1}$$

where I_0 is the total intensity of both polarizations, and I_x, I_y is the intensity of the x,y polarized light. I_x will obey Malus' law:

$$I_x = I_0 \cos^2(\theta - \frac{\pi}{4}), \tag{4.2}$$

where θ is a small angle between the plane of polarization and $\pi/4$. Using the cosine difference

formula:

$$I_x = I_0(\cos\theta\cos(\pi/4) + \sin\theta\sin(\pi/4))^2, \tag{4.3}$$

using a small angle approximation:

$$I_x = \frac{I_0}{2}(1+\theta)^2, \tag{4.4}$$

and using a Taylor expansion for small θ:

$$I_x = \frac{I_x + I_y}{2}(1+2\theta). \tag{4.5}$$

We can solve for θ:

$$\theta = \frac{I_x - I_y}{2(I_x + I_y)}. \tag{4.6}$$

In general, $(I_x + I_y) >> (I_x - I_y)$, so $\frac{1}{2(I_x+I_y)}$ is treated as a constant, and $(I_x - I_y)$ is usually reported as the rotation signal. The absolute magnitude of the rotation in millirads ultimately sets the sensitivity of the magnetometer to magnetic fields.

The difference signal is fed into a Stanford Research Systems SR560 preamplifier, where a bandpass filter is applied. The highpass value is typically at 300 Hz, high enough to definitely filter out any 60 Hz noise created upstream of the preamp.

Unlike previous magnetometry studies at the UofW (M. Das [10]), waveform digitization is done directly by a Tektronix DPO 4054 oscilloscope, rather than passing through a lock-in amplifier first. This means the oscilloscope must sample much faster, limiting the number of FIDs that can be held in the buffer of the scope, but it eliminates some possible phase dependent frequency shifts induced by the lock-in [10].

4.1.4 The pump beam and AOM

In order to have a pump beam that turns on and off in a well-controlled square wave an acousto-optic modulator (AOM) is used. I used an Isomet 1205C-1 AOM with a central frequency of 80 MHz. This device consists of a crystal affixed with a transducer. When the transducer vibrates the crystal at its central RF frequency, the compressions and rarefactions in the crystal form a standing wave that acts as a diffraction grating. The first order diffracted beam is only present when the transducer is active. By modulating the transducer's RF signal the diffracted beam can be turned on and off as desired. This beam forms the pump beam. Since the first order diffraction beam is used, there is perfect extinction of the beam when the AOM is turned off, as there is no diffraction when the AOM is not active. This allows us to turn the pump on and off easily at kHz frequencies with well defined duty cycles.

Most of the optics in the pump beam line are for the purpose of successfully launching the beam into and recovering the beam from the AOM. The alignment of the AOM is very sensitive, so it is mounted on a rotating mount. The angle of this mount is adjusted, and the beam re-aimed, until the first order beam has the maximum achievable power, typically $\approx 10\%$ of the incoming beam power in our case.

The intensity of the first order diffraction beam can be modified by changing the amplitude of the square wave used to modulate the AOM driver. A 0-1 V square wave will turn the AOM fully on and off. Values in between will result in reduced intensity of the beam. This is a convenient way of changing the pump beam intensity without using neutral density filters, or changing any other parameters of the beam.

Optimal diffraction happens when the polarization of the beam is perpendicular to the acoustic waves propagating in the medium. In this device the waves propagate along the body of the AOM, horizontally along the surface of the laser table. Since the main beam is polarized at 45°, a half wave plate is placed before and after the AOM to rotate the polarization to vertical for the passage through the AOM. The addition of these wave plates

improved the coupling efficiency into the first order diffraction mode, and eliminated some time dependant polarization changes that seemed to be caused by the AOM.

The diffracting region of an AOM is typically quite small, so lenses are also placed before and after the AOM to focus the beam into the AOM and re-collimate it afterwards. The first order diffraction beam, diffracted at an angle of 19°, is blocked by an aperture that only allows the zero-th order beam through.

Before the pump beam passes through the magnetic shield system and the Cs cell, it passes through the same polarizer as the probe beam, ensuring both beams have identical polarization. The beam is directed to overlap with the probe beam at the Cs vapour cell. This isn't strictly necessary to operate the magnetometer, and the final fibre-ized system will likely not have overlapping pump and probe beams, but this angle is necessary to pick up only the probe beam with the balanced photodiode. This can be seen in figure 4-1. The atoms maintain their polarization through many wall collisions, so the positions of the pump or probe beam do not not matter, as long as they are in the phase space of the atoms.

4.1.5 The vapour cell

The vapour cell is the most specific, and hardest piece of equipment to acquire. A plain glass cell full of cesium would not work very well for a magnetometry application, as the lifetime of the polarized state in such a cell is relatively short. In an uncoated vapour cell, almost every cell wall bounce is a depolarizing bounce, so the resulting signal is too small to use.

The cells required for this technique are coated with a special formulation of paraffin wax. The very best cells for this kind of work come from a single source, the lab of Mikhail Balabas at Saint-Petersburg State University. Moushumi Das' work in rubidium uses one such cell [10]. The process uses a custom distillation of wax [8]. These cells are difficult to obtain commercially, so for large scale system a reliable supply of adequate cells is needed.

Our lab has obtained several sample cells from the Colorado-based Precision Glass Blow-

ing, and they have proved to have sufficient lifetimes for our purpose. These are relatively small cells, 30 mm long by 10 mm diameter, so they can be placed into a relatively small magnetometer head (mag-head). They have a reservoir of bulk metallic cesium in a stem, with a small pinhole open to the cell. This ensures a vapour pressure of cesium in the cell, while preventing collisions between the vapour and the bulk metal, which would cause depolarization.

The wax coating is not optically significant in a typical cell, although some very old cells can start to display a bloom of wax in some localized spots in the cell. These may be due to deposits of bulk metallic cesium building up on the walls, or be the result of coming into contact with a heat source, melting the wax slightly.

The cell is held in the centre of the magnetic shield using wood and non-dyed plastic, avoiding any potentially magnetic materials.

The polarization lifetime of the cell was measured using Franzen's method of relaxation in the dark, as in [16]. The best cell had a lifetime of around 400 ms, depending on the exact tune of the laser. See appendix B for a figure, as well as a table comparing different cells tested in the UofW lab. The frequency dependence of the lifetime is studied in detail in the cited paper, and was replicated by my study as well.

4.2 Magnetics

4.2.1 The baby shield

In order to test very sensitive magnetometers, our collaboration has previously designed and built a four layer mu-metal magnetic shield, called the "baby shield" [25]. This served as both a prototype and proof of concept for a larger shielded volume, and studies of this and a larger version ultimately informed the design of the MSR for the nEDM experiment.

We believe the volume inside the baby shield to be the best magnetically shielded vol-

ume in North America, and it provides the magnetically quiet environment required to test these very sensitive magnetometry techniques. It consists of 4 nested cylinders, each with a stovepipe style endcap. The innermost endcap is typically left off in order to accommodate a degaussing coil wrapped around the innermost cylinder. A schematic view of the baby shield can be seen in figure 4-3. The quasi-static axial magnetic shielding factor of the baby shield has been measured to be $\sim$ 14 million [25]. The transverse shielding factor in such designs is typically orders of magnitude higher [31], although it hasn't been measured in ours.

There is a 16-turn degaussing coil wound toroidally around the innermost shield, and a single wire wound toroidally around the other three collectively. The coils are placed to drive magnetic field through the shields around the curved dimension, as in a toroidal winding. A strong oscillating field is driven back and forth through zero, and the amplitude slowly decreased, driving the remnant field in the mu-metal closer and closer to zero. At 4.2 A and 10 Hz, the H-field reaches a maximum of 210 A/m in the medium. This is enough to degauss [10]. This degaussing procedure is performed at least once per day, unless specific studies are being done.

4.2.2 The B coil

The inner B coil is the same as was used in Mouhsumi Das' thesis [10] and the shielding factor measurement [25]. It is a seven turn, 7.62 cm diameter solenoid, designed to provide an infinite field approximation when the innermost endcaps are installed in the shield. M. Das confirmed that the field generated by the solenoid is uniform in the center to within 5% when the innermost endcaps are not installed. The coil constant was measured to be $\approx$ 48 nT/mA.

The solenoid is also equipped with X and Y saddle coils, wound to provide a transverse field in two orthogonal directions. The saddle coils produce magnetic fields along and perpendicular to the plane of polarization of the incoming light. Assembling the baby shield

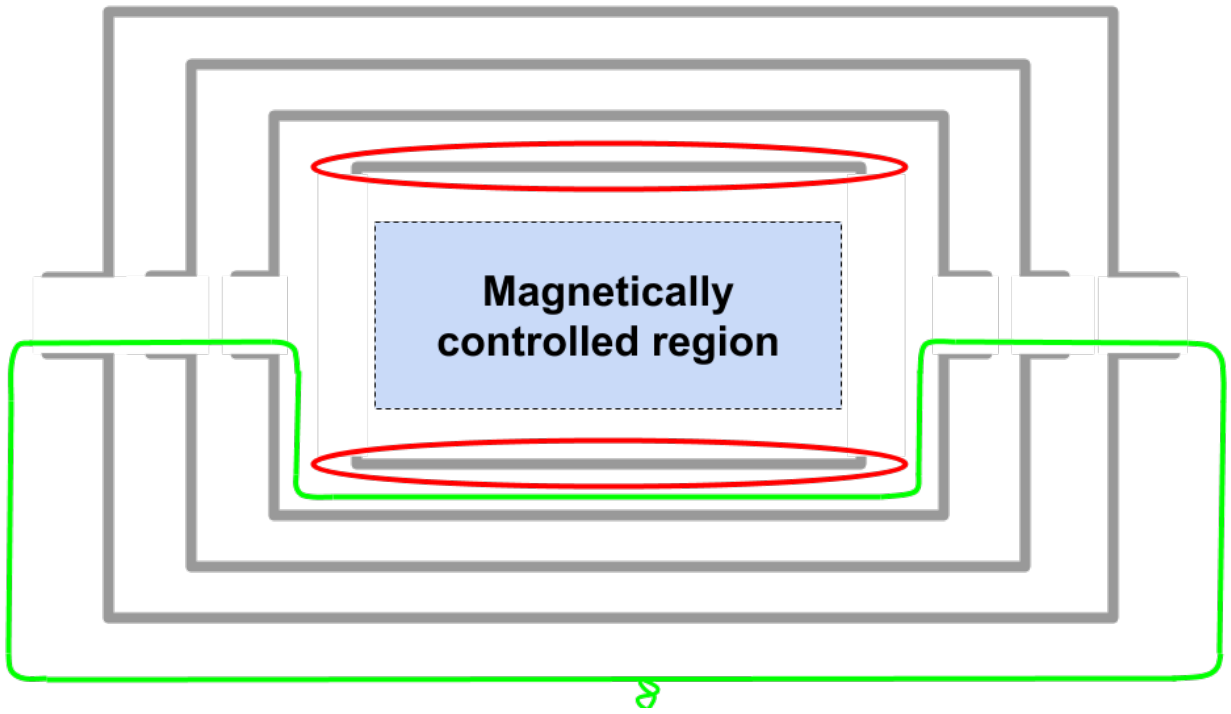

Figure 4-3: A schematic view of the baby shield. This is a top-down view of a horizontal cut halfway through the shield. The red ovals indicate two of the 16 degaussing coils wrapped around the innermost shield, shown here with its endcaps off. The green line is the outer degaussing coil, and it goes around the outermost 3 shells of the shield. The outermost shield is $\approx$ 30 cm long, and the innermost is 20. **Not shown:** the inner B coil and the Cs cell.

with a specific angle of the solenoid is non-trivial, so there is some uncertainty in the degree of alignment. The saddle coils are typically only used for tilted field studies. They can also be used to buck remnant transverse fields inside the baby shield, but this effect is typically too small to bother with.

The B coil is driven by an Agilent B2962A 6.5 digit low-noise power supply. A current of 20 mA provides a magnetic field just under 1 μT, the design value for the nEDM experiments' B_0 field. Experimentally, this unit was found to operate much more stably at 10 mA. Final results in this thesis use this lower more stable current. Figure 4-4 shows the result of performing magnetometry with a setting of 20.00000 mA, see figure 5-5 for comparison. The reading is $\sim 1\mu$T. The data are stable to within 0.004%. In general, fluctuations in the

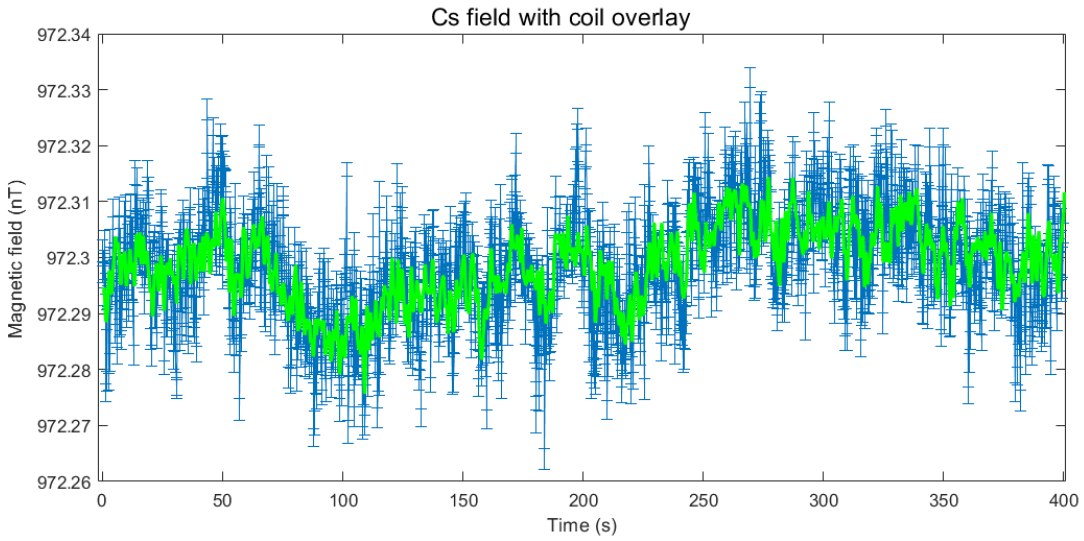

Figure 4-4: Repeated FID measurements (in blue) compared to the recorded current in the B coil (in green). The current has been scaled to match the FID data. The correlation between the coil current and the magnetic field is apparent.

current are seen in the magnetometer. The correlation is strong enough to conclude that the stability of the DC current plays a significant role in characterizing these magnetometers. This was the first time this kind of current-field correlations were seen in the UofW lab.

Each FID required 6 ms to pump up, and was allowed 194 ms to decay, for a total of 2000 FIDs acquired during these 400 seconds. The time constant of these FIDs was $\sim$ 25 ms. The error bar on each FID measurement is calculated from the covariance matrix of the least squares fit of the decaying exponential.

The current is monitored by a Keithley 2002 Digital Mutlimeter (DMM). The current going to the coil is first shunted through a 100 Ω Vishay foil resistor to produce a voltage. The Vishay is chosen because of its low temperature coefficient. The absolute value of the resistor isn't critical, as the voltage reading is normalized to a field reading using the Cs precession frequency. Based on typical temperature fluctuations in the room, the reading across the resistor is reliable to within 2 ppm [10]. The standard deviation of the coil current

was $\sim$ 0.16 mA, which translates to a magnetic field standard deviation of 7.9 pT. The maximum range was 50 pT, this is visible in figure 4-4 as 0.05 on the vertical scale. The Keithley is set to perform 10 power line cycles with the full 8.5 digits of precision available. This makes the effective bandwidth of the coil reading 6 Hz. 2000 readings are made in 400 seconds for a sample rate of 5 Hz.

There is a component of noise not correlated to the current. This may be a real change in the magnetic field, such as external fields being imperfectly shielded by the $\mu-$metal or thermal magnetic noise from the shield itself. As shall be discussed in section 5.1.1, this may also be the result of the uncertainty associated with fitting for the frequency of a noisy signal. It is difficult to test the contributions of current instability with the limited bandwidth of the device. The next step is likely to get a better current supply.

4.3 Electronics

Most of the electronics used in the execution of an FID are controlled from a Matlab program (See Appendix C) running on a laptop. This section will provide a full list with part numbers, parameters, and function in the experiment. This does not include the laser controllers, which are considered part of the laser system. The AOM and degaussing circuit are discussed in detail in M. Das' work [10].

Keithley 2002 DMM

The Keithley digital multimeter (DMM) monitors the voltage across a precision foil resistor, and therefore the current inside the B coil. It is set to the 2 V scale, with the maximum 8.5 digits of precision. It performs 10 power-line-cycle averages per reading, imitating the relatively long integrating time of the FID. It is controlled by channel one on the Prologix GPIB controller, which also collects the data from the DMM.

Agilent 33522A Arbitrary Waveform Generator (AWG)

The Agilent arbitrary waveform generator (AWG) provides the square wave that modulates the AOM driver, as well as the waveform that drives the degaussing circuit. The square wave is typically a 0-400 mV square wave with a 10% duty cycle, at a frequency of 3.4 kHz (for the 0.5 μT field) or 6.8 kHz (for the 1 μT field). The waveform generator is set to provide this square wave in 30-50 cycle bursts, 100 ms apart.

The degaussing waveform is a 10 Hz sine wave that ramps from 0 to 10 V in 4 seconds, then from 10 back to 0 in another 16 seconds. This is put through a very stable trans-impedance amplifier to turn the voltage signal into a current signal, and a transformer to decouple the degaussing coils from the DC circuit. The Agilent AWG is controlled by channel 2 on the Prologix GPIB controller.

SRS SR830 DSP lock-in

The lock-in amplifier is used when performing AM NMOR resonance scans. The sensitivity is set to 200-500 mV/nA, with a time constant of 100 ms. This is controlled by channel 3 on the Prologix GPIB controller, which also read the data back for storage.

Agilent B2962A PS

This power supply drives the current through the B coil. It is typically set to provide 10 mA, with a voltage protection of at least 4 V, to avoid being voltage limited. The current seems to be much more unstable when operating in voltage limited mode. The second channel can be used to drive the saddle coils if desired.

SRS SR560 Preamp

This preamp filters the signal from the photodiode. The gain is set to x200, with a bandpass filter from 300 Hz to 10 kHz.

Tektronix DPO4054 Scope

Channel one of the scope shows either the X or Y signal from the lock-in. This is only used when performing AM NMOR scans.

Channel two of the scope shows the filtered and amplified signal from the photodiodes. The scale is adjusted so the FIDs fill the vertical range of the screen. The scope is in hi-res mode, which oversamples at the maximum sample frequency of the scope, then downsamples and averages them to my desired sample rate. This effectively eliminates high frequency noise.

Channel three of the scope shows the intensity of the pump beam, as measured by a single photodiode picking up the beam after it passes through the shield. This was not used in the final data sets, but was useful for developing and troubleshooting the system.

Channel four shows the trigger signal from the Agilent AWG. This signal is synced to the burst mode of the AWG, so it is only on when pumping is active.

The scope is set to trigger at the very beginning of the scopes memory buffer, and fill the entire scope with FIDs. The scope is controlled via USB through the same Matlab program, which also reads the data from the scope at the end of the run. All data analysis is done offline.

New Focus 2307 Balanced Photodiode

This photodiode is set to provide the highest gain possible, and the signal is fed directly into the preamp. No other adjustment or control is necessary .

Keithley 223X-30 PS

The sole function of the Keithley 3-channel supply is to provide fine adjustment over the laser diode current. To use the stable mid range of the supply, the dial on the laser supply

is deliberately set low, and the rest of the current is provided by the Keithley. 2-300 mV is the voltage associated with this current.

4.3.1 Collecting data

The data collection program first connects to and sets up each piece of equipment. The user is prompted for most setting values, which are stored in a metadata text file. This includes things like the filename to be saved under, the frequency of the AOM modulation, the duty cycle and peak intensity values, etc. This also includes the oscilloscope buffer length, sample rate, sample method, and coupling. Vertical and horizontal scales are set as well.

The Agilent AWG is set to start generating the AOM controlling bursts as soon as it is set up. When ready to start taking data, the scope is set to perform a single trigger, which starts the scope recording FIDs. The trigger is set to use the sync output form the AWG, so the scope triggers when the pump beam stops.

Since the FIDs are recorded in the scope buffer and only transferred in the end, the control program is free to run a sub-routine, controlling the Keithley to read the voltage in the Bz coil. This is done at an even multiple/divisor of the FID sample rate, so the trendline of the two can be easily compared/subtracted.

Once the buffer of the scope is full the control program downloads the data channel by channel from the scope and stores them in a data structure to be analyzed offline. Each channel reading is also associated with an array of timestamp values, one for each reading in the buffer. These should all be identical, and one of them is saved as an array as well. The signal is now ready for analysis. Figure 5-3 shows the display of the oscilloscope during a typical measurement.

Chapter 5

Analysis and results

This chapter will go over the analysis method used to process the FID signals, as well as show the final results of the system as a magnetometer.

5.1 Analysis

This section will describe the data taking process, then go over the analysis of that data. With these tools in place, results are discussed in the next section.

5.1.1 Extracting and fitting FIDs

The FIDs are separated into individual data structures, so each can be passed through to a fitting program. findFIDs.mat examines the trigger signal from the AWG, and finds the places where it jumps from low-to-high and from high-to-low. A low-to-high transition indicates the end of an FID, while a high-to-low transition indicates the beginning of an FID. The beginning indices are all stored in an array, the end indices are all stored in an array, and these two arrays are stored together. This array is structured so that ind(600,1) is the beginning of FID #600, and ind(600,2) is the end. These values are then used to separate

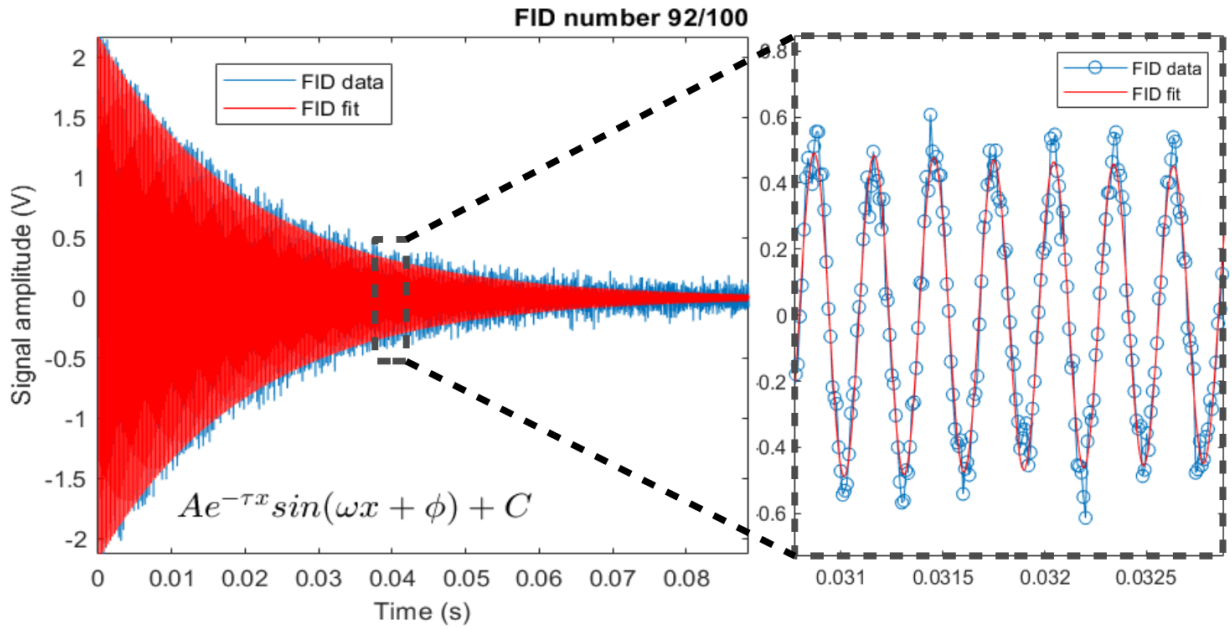

Figure 5-1: A single FID showing the fit. The red line is a close fit to the signal.

and save the FIDs separately before analysis.

In order to evaluate the fit method itself, I used the arbitrary waveform editor in the Agilent AWG to create a convincing fake FID with a precisely defined frequency to test my fit method against. The waveform is created by defining a series of points that are played back at a certain rate by the AWG. The rate of playback is controllable to 10 decimal places in megasamples per second. By defining a waveform 100,000 points long with 340 full cycles of a sine wave, the frequency is defined to the nHz level, corresponding to 1×10^{-18} Tesla in our system. This waveform is multiplied by a rising and falling exponential to mimic the decay of the real FID. White noise is added using the software to mimic the variance in a real FID signal.

The FID being played back by the AWG is identical each time including the white noise profile, minus the small amount of noise introduced by the SRS preamp and the scope itself. By fitting an identical FID repeatedly the variance introduced by the fit method itself can be measured, and potential phase/frequency dependent effects examined without them being

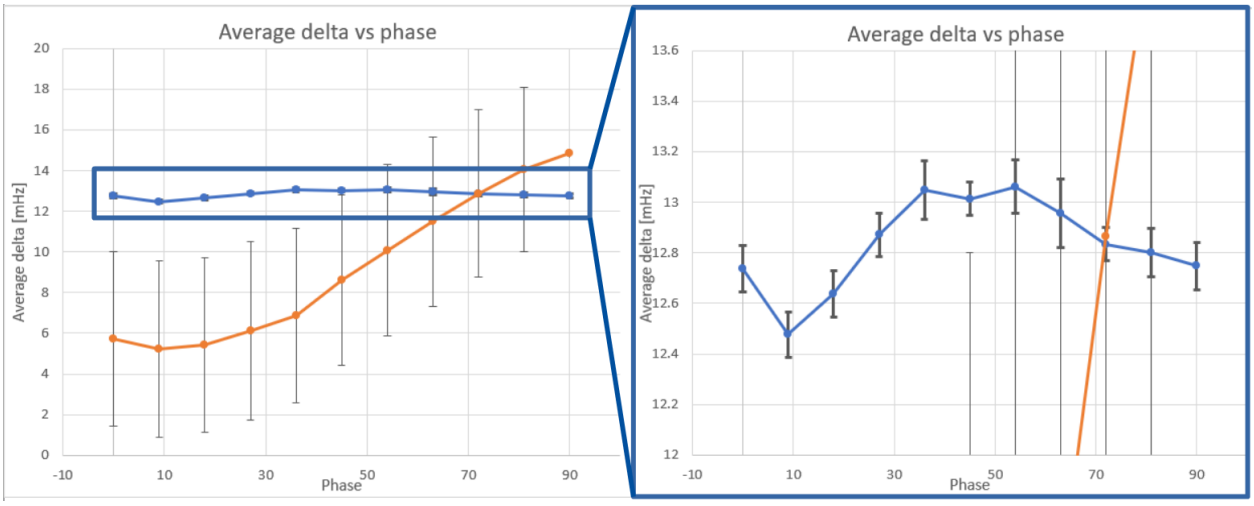

Figure 5-2: Deviations in mHz from the exactly defined frequencies as a function of phase. Each point is the average deviation for that phase value as averaged over all the frequencies. The error bar indicates the standard deviation of the results for that phase. The orange curve was made using an frequency domain method for frequency extraction, the blue curve with a time domain fit. It is reasonable to assume that this phase response is symmetric about 90°, meaning this is a reasonable range to sample.

washed out by the much larger noise effects. A total of 21 FIDs with frequencies between 3390 and 3410 Hz are fitted, each with 10 different phase settings between 0 and 90 degrees. Figure 5-2 shows the result of this study. The points are the average difference between the exactly defined and fitted frequencies for that phase, and the error bars indicate the standard deviation of the differences for that phase. The blue time domain result is much stabler in both frequency and phase. 45° is the most stable in terms of frequency response, and the phase response also looks flattest at 45°. A time domain fit at 45° is the best option.

This is the uncertainty associated with the fitting method itself, as the white noise built into the signal is the same each time. The uncertainty from this method is 0.5 mHz, or 70 fT. This is much smaller than the uncertainty associated with the noise in the signal, but confirms the optimal fit method and parameters.

Nine additional fake FIDs are made with identical parameters, but unique white noise. The definition of the white noise waveform parameters in the AWG is unclear and poorly

File name	$\overline{\mathbf{Var}}$ [mV]	$\boldsymbol{\Delta F}$ [mHz]
FID_013.arb	60	55.7
FID_014.arb	59.6	-59.8
FID_015.arb	59.7	32
FID_016.arb	59.2	-47.1
FID_017.arb	59.5	47.1
FID_018.arb	59.4	6.9
FID_019.arb	61.1	-33.3
FID_020.arb	59.8	1.9
FID_021.arb	60.9	-49.4
FID_022.arb	60.9	-9.2

Table 5.1: Trials of fitting machine generated FIDs. Each one was constructed through the built-in waveform generator function in the Agilent AWG. The average variance of the real FID being modelled was 58.8 mV. The sample standard deviation of the deltas is 41.6 mHz, or 5.9 pT.

documented, so trial FIDs were made until the observed variance in the collected signal matched a sample FID collected at the same time, an average of 60 mV variance from the fitted equation. This ended up being slightly larger variance than the final best experimental signal produced.

Taking into account rounding errors and the small intrinsic fit error found earlier, a 6 pT standard deviation is reasonable to expect from a signal with 60 mV average variation. This generally agrees with the results of real FIDs, as shall be seen in section 5.2.

5.1.2 Optimizing FID parameters

The pump beam power, pump duty cycle, number of cycles in the burst, beam tune, AOM modulation frequency, and probe beam power are the parameters that were optimized for the purpose of extracting the frequency.

The number of cycles in the burst is the most straightforward to optimize. Depending on the other parameters, it is possible to pump the atoms into the dark state faster than they relax out of it. In such a case the optimal pump time is clear, as seen in figure 5-3.

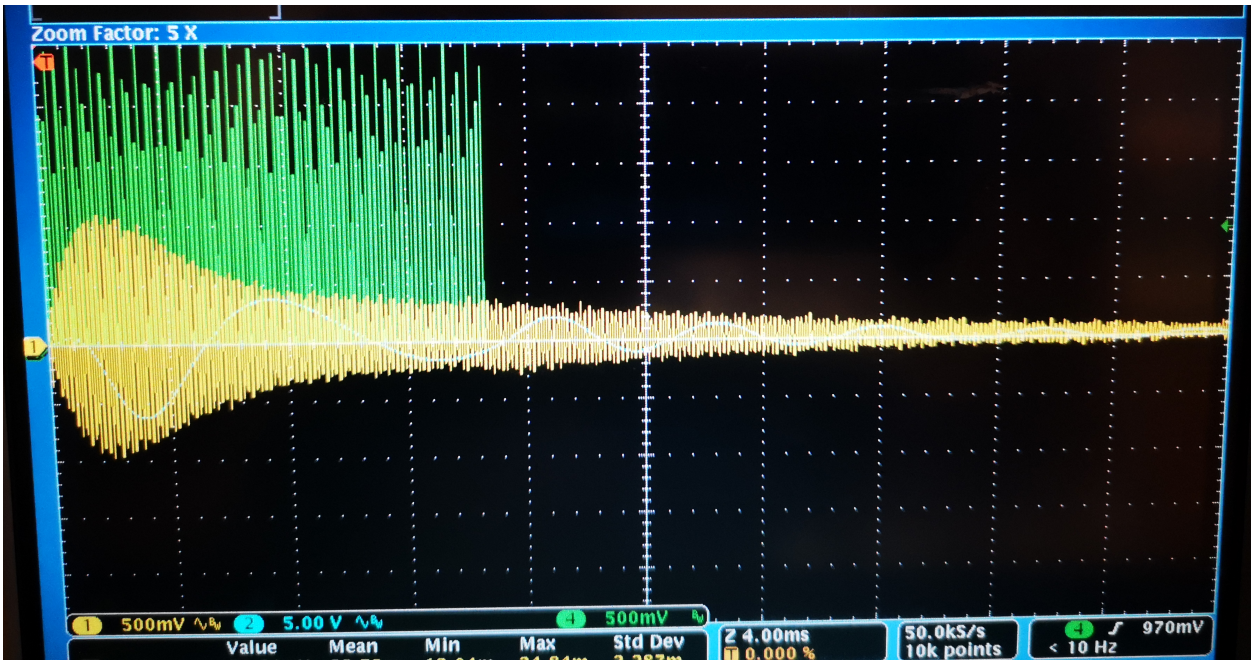

Figure 5-3: An example of an overpumped system. The characteristic double exponential is clear, with an obvious maximum.

Halting the pumping at this maximum will result in the largest signal amplitude, allowing the atoms to oscillate coherently for longer. Since adjusting the burst length shouldn't affect the relaxation rate after the pump is turned off, maximizing the amplitude will also maximize the signal fidelity. For any given set of other parameters, the burst length can be optimized by over pumping, looking for this maximum, then adjusting the pump time accordingly. This is typically done by hand for each change in parameters, including changing the tune of the laser, the duty cycle, or the power. The best results typically happened when the burst length was 30-50 cycles long. The systems that took longer than that to pump up usually had either a much smaller amplitude or a much shorter lifetime.

The laser was tuned at the beginning of each day of data taking, after being allowed to warm up for a day. Actually optimizing the tune is with respect to the goal of fitting for the frequency of a single FID accurately. The best NMOR response was on the wings of the $6^2P_{\frac{1}{2}} \rightarrow 6^2P_{\frac{3}{2}}$ transition line. Doppler-free saturated absorption spectroscopy was performed

on the Cs to confirm the tune, shown in figure 4-2. Once this tune was found, returning to it was simply a matter of setting the same current in the diode. The exact current varies from run to run, but is generally within 1 mA of the previous setting. The laser current is adjusted as FIDs are taken, and the uncertainty on the frequency fit parameter is used to determine the best tune.

The laser power and duty cycle are very closely linked, as each is proportional to the total power being pumped into the cell. Additionally, both the probe power and the duty cycle are linked to the decoherence time of the atoms. The error calculated from the covariance matrix from the fit was used as a measure of fitness. The final error is not calculated this way, but is a good measure for the sake of optimization. See Appendix B for the full set of graphs. Figure 5-4 shows the best results, obtained with a probe power of 5.3 μW. However, the results are very similar to the 7 μW plot in the appendix, indicated that the magnetometer response is fairly flat in probe power. Also examining figure 5-4 there is little difference between the minima reached by the 0.2 and 0.6 relative pump power, indicating a flat response in pump power as well. Finally, each of the curves is fairly flat near the bottom. The broad minimum indicates that the magnetometer will work just as well for a fairly broad range of parameters. This will make for a robust system.

The AOM modulation frequency is found by performing a single AM NMOR resonance scan, sometimes called a forced oscillation scan (FOS). The FOS can be fit to the in and out of phase components of the lock-in signal, seen in figure 3-4. The two signals from the lock-in will be admixtures of absorptive and dispersive Lorentzians. The two signals are nominally orthogonal, so a single phase parameter describes this admixture. A simultaneous fit is

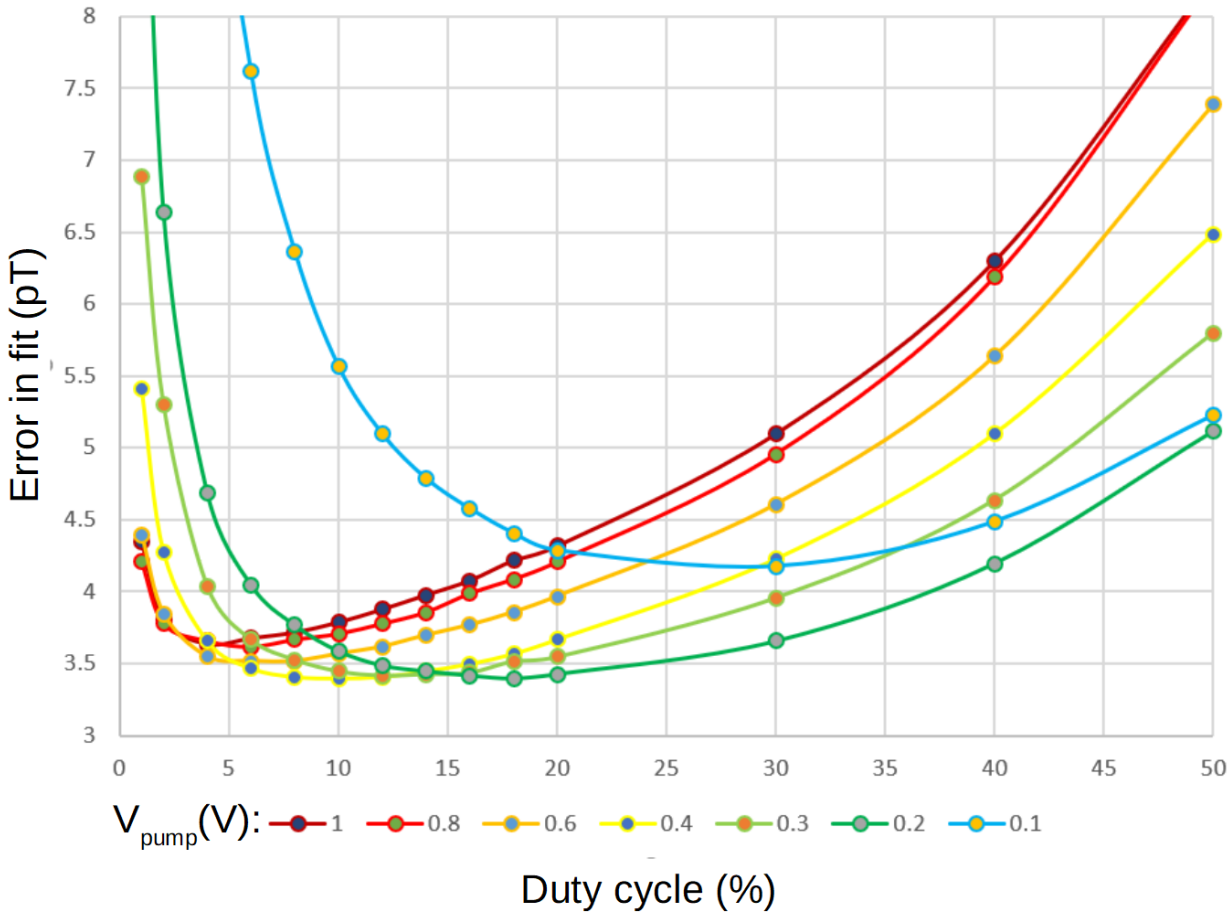

Figure 5-4: Fit error as a function of duty cycle for various pump powers, with a constant probe power of 5.3 μW. The pump power values are scaled to their maximum value. The fit error is calculated from the covariance matrix of the least-squares fit. This is only equal to the statistical error if all data points are completely independent and statistically distributed.

performed using the lsqcurvefit function in Matlab. The two functions can be written[10]:

$$Y = \cos(\theta) \cdot \left(\frac{A \cdot \omega \cdot (\frac{x-f_0}{2})}{(x-f_0)^2 + \frac{\omega^2}{4}} \right) - \sin(\theta) \cdot \left(\frac{\omega^2 \cdot \frac{A}{4}}{(x-f_0)^2 + \frac{\omega^2}{4}} \right), \tag{5.1.1}$$

$$X = \sin(\theta) \cdot \left(\frac{A \cdot \omega \cdot (\frac{x-f_0}{2})}{(x-f_0)^2 + \frac{\omega^2}{4}} \right) + \cos(\theta) \cdot \left(\frac{\omega^2 \cdot \frac{A}{4}}{(x-f_0)^2 + \frac{\omega^2}{4}} \right). \tag{5.1.2}$$

This is done once at the beginning of the day. This frequency is related to the magnetic field in the experimental region, therefor it is as stable as the field. Once the power supply was switched to run in a current limited mode, the frequency was usually stable to within 1 Hz over the course of a day, and did not need adjusting between runs.

5.2 Results

With a probe power of 5.3 μW, a pump power of 0.5 mW, a 10 % duty cycle, and 35 total pump cycles before each probe cycle, figure 5-5 shows the calculated field overlaid on the current from the solenoid (scaled so their averages match). The rate of the Cs FIDs is 10 Hz, the coil current bandwidth is 5 Hz. The standard deviation of this signal is 3.85 pT, and the standard (statistical) error on the mean is 122 fT. This is a shorter run than the one in figure 4-4, with 1000 FIDs collected over 100 seconds. Relative to that run, these FIDs are allowed half as much time to decay, $\sim$ 90 ms. The decay constant was $\sim$ 43 ms. Fitting errors are not shown for each FID in this plot. I instead rely on other statistical tests over time, such as the Allan standard deviation (ASD), as is discussed next. The set current for this run was 10.00000 mA, using the full 6.5 digits of precision of the Agilent PS. The Keithley monitor settings were the same as the drifting run. The current fluctuations are smaller than the 20 mA trial, with a standard deviation equivalent to 0.8 pT, an order of magnitude improvement. The maximum variation in the current is equivalent to 4.8 pT,

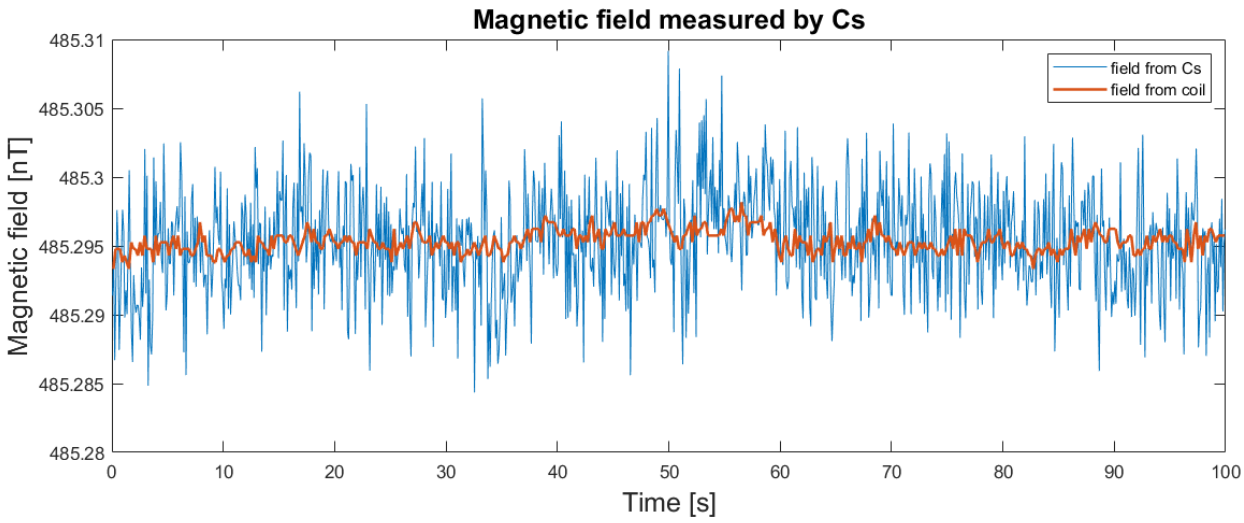

Figure 5-5: 100 seconds of field measurements made by the Cs magnetometer. The blue curve is the Cs signal, the red is the current measured in the solenoid, scaled to match.

again an order of magnitude improvement.

The average voltage variation on this signal was 45 mV, making 3.85 pT a reasonable standard deviation, given the noise study performed earlier. In general the current lies within the envelope of the magnetometer signal, largely due to bandwidth differences. The correlation of the magnetometer with the current is reduced, but still visible.

The Allan standard deviation is used to examine errors for quantities measured over long periods of time. The ASD is an indication of the stability of a signal with respect to an integration time, τ. The ASD is given by

$$\sigma_y(\tau) = \sqrt{\frac{1}{2(P-1)} \sum_{k=1}^{P-1} (\tilde{y}_{k+1} - \tilde{y}_k)^2}, \tag{5.2}$$

where τ is the duration of the averaged section of data $\tilde{y}_k$, given by

$$\tilde{y}_k = \sum_{i=(k-1)N+1}^{kN} \frac{y_i}{N}, \tag{5.3}$$

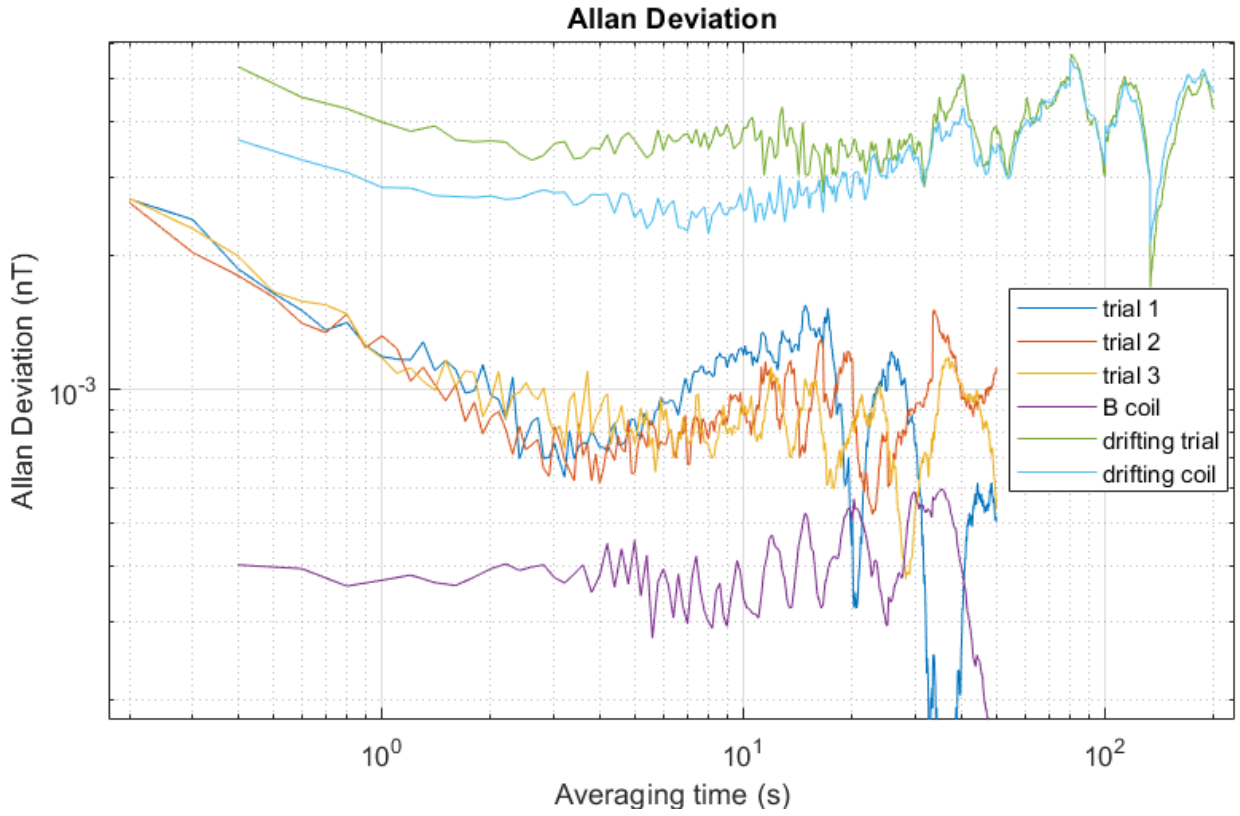

Figure 5-6: An Allan deviation plot for the final 3 trials, along with the Allan deviation of the B coil from the last run. The Allan deviations of the noisy current supply and noisy run from section 4.2.2 are also shown. The minimum of the ASD is lower than 1 pT for averaging times on the order of seconds in the best runs.

where y_i are individual data points, in this case a total of N FID frequencies.

For a signal that is purely a statistical distribution of points about a mean the ASD at $\tau = 0$ is equal to the standard deviation, and the ASD will fall as $\sim \sqrt{N}$. The standard deviations of each signal plotted in figure 5-6 are each higher than ASD($\tau = 0$), which is consistent with each signal having a drift on top of its statistical fluctuations. The ASD of the magnetometer in trials 1-3 in figure 5-6 drops statistically, with one decade drop per two horizontal decades, until the minimum at 3-4 seconds. It then becomes dominated by drifts. The ASD of the magnetometer is consistently above the ASD of the current monitor for the measurement period of 100 seconds. The ASD of the current monitor is flat, indicating non-statistical behaviour. The lower bandwidth of the current monitor means that high frequency contributions to the magnetometer ASD are not ruled out, although the statistical behaviour of the magnetometer ASD suggests this effect must be small. A new current supply is needed to test this system further.

Magnetometers of exactly this configuration have not been used for nEDM experiments. The PSI nEDM experiment used an RF-coupled Mx configuration Cs magnetometer [1], which achieves the required spin coherence via an RF coil driving an oscillating magnetic field at the Larmor frequency of the atoms. They have done in-situ measurements with a demonstrated sensitivity of 750 ft/$\sqrt{Hz}$. The closest work to our configuration is done by Grujić et al. [17], who operate a free spin precession magnetometer with orientation pumping rather than alignment pumping as in our system. They calculate a real-world performance of 200 fT/$\sqrt{Hz}$, although this is a theoretical calculation, not based on real time-domain magnetometry signals. They found in that work that pumping an oriented state with circularly polarized light can induce energy shifts that change the Larmor precession of the atoms. This can create arbitrary offsets as high as 100 pT [4]. This should not be an issue in alignment pumping [17], where we use linearly polarized light.

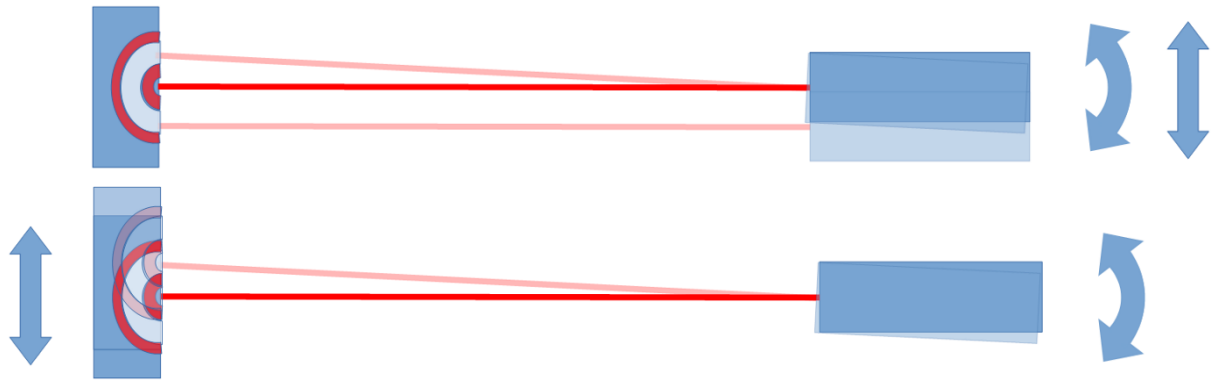

Figure 5-7: A schematic showing two fibre coupling schemes which both require walking the beam. Maximal coupling is achieved when the beam is centred on the target and normal to it. Available adjustments are shown with arrows. Neither adjustment alone can make the coupling better, a compound adjustment is required.

5.3 Fibre studies

5.3.1 Coupling

In addition to the magnetometry studies, I also performed some fibre coupling studies. These will motivate the ultimate design of the magnetometer heads. These studies were all qualitative studies of launching into fibre in different configurations, with different adjustable parameters. There are two broad categories I found, those configurations that require "walking the beam" and those that did not.

Since I am working with a fixed wavelength, I can select fibres and fixed lenses that produce the beam profile I want, a collimated $\sim$ 2mm free space beam. This is the beam that will be produced in the mag head to pass through the vapour cell, and coupled back into some kind of fibre to be analyzed. For these studies I use 1 m lengths of single mode fibre. One end of each fibre is a fixed GRIN lens to collimate the fibre mode into a free space beam, the other is an FC/APC connector. The GRIN lens is built into the fibre so does not need to be adjusted. In order to launch into the fibre I used a fixed focus aspheric collimation lens, which attached to the FC/APC connector. I launched the DFB laser into

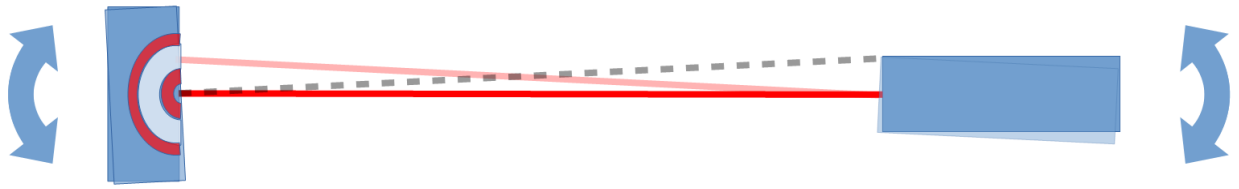

Figure 5-8: A schematic showing a coupling scheme which does not require walking the beam. The black dotted line indicates the normal of the target. This scheme does not have the constraint that the beam must lie parallel to the original beam path.

a length of fibre using such a lens, to act as the laser source. This ensures that the beam profile of the free space beam I'm studying matches the final one.

The GRIN lenses attached to each fibre are intended to be used in matched pairs, the beam profile produced by such a lens should be the ideal profile to launch back into one. There is an ideal coupling distance according to the manufacturer (Thorlabs), but the difference in coupling efficiency is too small for me to notice at this stage.

The main difference between studies was what kind of kinetic stage each lens was mounted to. Which lenses were adjustable and in what way determined if "walking the beam" was necessary. This is when a compound adjustment of parameters is needed in order to improve coupling. Figure 5-7 shows two such schemes. Maximal coupling is achieved when the beam is centred on and normal to the target. Simply maximizing the coupling with each parameter in turn cannot lead to maximal coupling. Instead two parameters must be changed simultaneously, the results of which inform the next adjustment. The procedure is complicated, and takes practice to perform well. This method guarantees the final coupled beam is parallel to the targets original beam path, which may be desirable in some cases.

Figure 5-8 shows a coupling scheme that does not require walking the beam. The black line shows the normal of the target. In this scheme a straightforward maximization of the coupling with respect to each parameter will result in maximal coupling. This scheme eliminates the constraint that the final beam end up parallel to the original optical axis.

Additional constraints can make walking the beam necessary again. If I split the beam

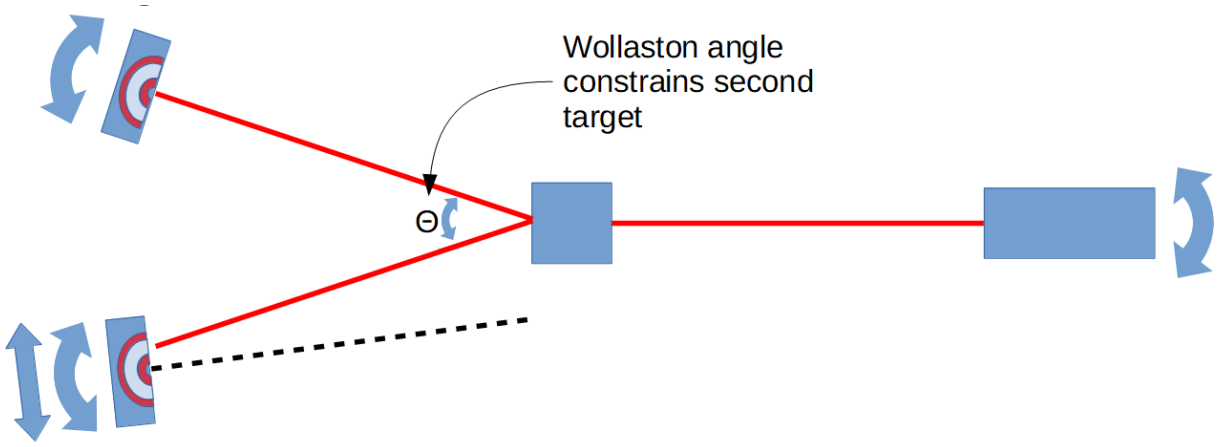

Figure 5-9: A schematic showing coupling multiple targets from a single source. More adjustment is needed in order to couple all beams, and walking the beam is again needed.

# turns	P_{max}	P_{max} with polarizer	P_{min} with polarizer	degree of polarization
1	12.2 mW	8.92 mW	2.53 mW	56%
2	12.25 mW	11.2 mW	170 μ W	97%
3	12.2 mW	9.17 mW	2.28 mW	60%

Table 5.2: The degree of linear polarization of the beam after passing through a fibre wrapped around a lens tube a number of times. This was to simulate different fibre conditions. The degree of polarization is very sensitive to fibre conditions.

as in the polarimetry setup, the additional constraint of the angle of the beam splitter makes coupling much harder. Figure 5-9 shows a minimal example of the controls required to couple the two beams. Even if the top target is coupled perfectly, the bottom target must reduce to one of the schemes in figure 5-7, meaning walking the beam is required once again.

5.3.2 Polarization

The polarization of the beam after passing through the fibre is very sensitive to the condition of the fibre itself. I wrapped the fibre around a one inch diameter lens tube a number of times to simulate non-ideal fibre conditions. I passed the beam through the fibre, a linear polarizer, then collected the light with a power meter. Table 5.2 shows the result of 1, 2, and 3 wraps around a lens tube, showing that the signal is very sensitive to fibre condition.

Θ_i	Θ_{max}	I_{max} (mW)	I_{min} (mW)	P_L (%)
0.9°	242.5°	8.7	2.47	56
10.0°	234.0°	8.9	1.98	64
20.0°	217.0°	8.97	1.09	78
30.0°	218.0°	8.18	0.37	91
40.0°	203.0°	6.81	0.05	98.5
45.0°	201.0°	5.86	0.007	99.8
50.0°	200.0°	4.98	0.03	98.8
60.0°	196.0°	2.91	0.12	92
70.0°	192.5°	1.33	0.15	80
80.0°	174.0°	0.35	0.07	67

Table 5.3: Degree of polarization for various incident angles. The incident angle is controlled by rotating a linear polarizer before the beam is launching into the fibre, which is why I_{max} is not constant. There is an angle which achieves maximal linear polarization in the fibre.

The degree of polarization of the beam is also sensitive to the incident angle of polarization. Table 5.3 shows the degree of polarization for various incident angles. This angle is relative to how the lens is mounted in its kinetic stage, so it is a relative measure not an absolute one. Any twists in the fibre will effect this angle as well.

Chapter 6

Conclusion and outlook

6.1 Conclusion

In this thesis I have developed and standardized the gradient decomposition method that will be used in the TUCAN nEDM experiment. I have identified the gradient terms most relevant to one particular systematic error, and shown a way to extract this quantity from local field measurements around the precession cell. My simulations have shown that it is in principle possible for an array of 20 scalar magnetometers with pT sensitivity to fulfill this role in the experiment, and shown how such an arrangement can be found.

This work has provided insights into further studies that should be done with the position optimization, these will be carried out by myself at the UofW during the summer of 2020. I plan to build further confidence in the performance of the results from Ferret, and study more restrictive exclusion zones. A new method of using scalar magnetometers to make vector field maps was introduced recently [2], and incorporating this technique is also part of these new studies.

I developed a prototype Cs based optical magnetometer which serves as a proof of concept for the final system. This system is sensitive enough to measure a 1 μT magnetic field to

within 120 fT over 100 seconds. I developed all of the machine control programs required to execute and collect measurements. In developing this prototype I also developed techniques for optimizing various aspects of the NMOR signal, such as pump power, duty cycle, number of pump cycles, etc. I also made progress toward a fibre optics coupled design, and a partnership with a commercial optics company.

The precision goal that my system meets is a statistical one, studying systematic errors requires more than one sensor. Other magnetometry systems [3] have reported unknown or drifting systematic offsets on the order of 50-100 pT, which would be well outside the requirements of this system. Some of these offsets stem from the techniques used in those magnetometry schemes, and my system should be immune to many of them, such as the offsets from pumping with circularly polarized light, or phase drifts in a lock-on signal. Systematic studies with our magnetometer will have to wait until we have multiples to test against each other.

6.2 Outlook

The next steps in the development of this system are the fibre-ization of both the pump and probe beams. From my brief studies of fibre coupling the DFB laser diode into fibre optics, designing a mag-head with multiple fibres in and out would be a challenge, from a mechanical alignment perspective.

6.2.1 Fibre coupling

There are three fundamental requirements for light in the mag-heads. The pump laser must be delivered to the vapour cell, the probe laser must be delivered to the vapour cell, and the rotation signal must be reported to the DAQ. Given these 3 conditions, there are 2 main viable configurations for the fibres in the mag-head. I refer to these as 2-in-2-out, and

2-in-1-out.

2-in-2-out is the most straightforward configuration, but perhaps the most difficult to implement. The pump and probe beams are each delivered by a fibre, collimated to a mm sized free space beam by a GRIN (graded index) lens, built into the end of the fibre. These can be made of completely non-metallic parts, and since they are permanently mounted require no aiming or adjusting in order to achieve collimation. The pump beam gets dumped inside the head after it goes through the vapour cell, but the polarization rotation of the probe beam has to be analyzed still. This is the major difference between the two configurations. In the 2-in-2-out version, the probe beam is split into its polarization components in the mag head, by a polarizing beam splitter (PBS) of some kind, usually a Wollaston or Rochon cube. The two resulting components are coupled into separate multimode (MM) fibres, which carry the signals outside the MSR to be analyzed.

The disadvantage in this configuration is the difficulty in launching the beam into the MM fibre. In this geometry, there are sufficient constraints to ensure that "walking the beam" is always necessary to align the beam, that is, a compound adjustment of two beam parameters is needed to maximally couple the beam. It is difficult to build this fine adjustability into such a small sensor head, especially since it will likely be made of plastic.

The solution for this is the 2-in-1-out configuration. The pump beam is unchanged, but the probe beam is not split in the mag head. Instead, it is coupled into a single polarization maintaining (PM) fibre after passing through the vapour cell. This single fibre is then fed out of the MSR for analysis. If the kHz optical rotation signal can be successfully carried by the PM fibre, this is a much easier configuration to realize practically, as incremental optimization of beam parameters is enough to maximally couple the beam into the fibre.

Another potential simplification is to eliminate the separate probe beam and use a single pump-probe beam. The probe beam is not needed when pumping is active, and the pump beam is not needed when probing is active. In principle, one could use the "off" portion of

the pump duty cycle as a probe, if the intensity could be controlled well enough. This was proposed during this work, but never tested. This could lead to a very simple 1-in-1-out design for the mag-heads.

6.2.2 More Ferret optimization

My optimization work with Ferret has lead to several other TUCAN subsystems looking into optimization with Ferret. Dr. Beatrice Franke put me in contact with a UBC engineering capstone project underway at the time of writing. I am guiding them through using much of my magnetic field generation code. Ultimately they will do much more general field mapping and sensor optimization study with Ferret than I had a chance to, I am helping them through much of the development I did during my own project.

The active magnetic shielding subsystem (in particular the work of collaboration member Dr. Takashi Higuchi) is also showing interest in using Ferret to help design active magnetic shielding around the MSR.

Finally, I am working with professor Fiege to integrate an optimization tool with the nEDM experimental design as a whole. This work seeks to maximize the overall sensitivity per day of the nEDM experiment with respect to various experimental design parameters. This builds on a single parameter sensitivity search done by lead members of the collaboration including Drs. Russ Mammei and Rüdiger Picker.

6.2.3 Commercial integration

The final version of this system implemented by the TUCAN collaboration will involve at least 20 individually manufactured magnetometer heads. This is not practical to carry out at the UofW. We have been in contact with a specialty optics manufacturing company, Southwest Sciences, in particular optical magnetometry expert Dr. Chris Hovde. Ultimately

Southwest Sciences will carry out the manufacture of the magnetometers to our specifications, under the supervision of Dr. Hovde. I believe some further tests of fibre compatibility are needed before designs are finalized, but a formal agreement is in preparation.

Appendix A

Tables

A.1 The Associated Legendre Polynomials

Here is listed the Associated Legendre Polynomials, including the Condon-Shortley phase, up to $l = 6$

Table A.1: The Associated Legendre Polynomials, sorted by degree

l m	$P_l^m(x)$
0 0	1
1 0	x
1 1	$-\sqrt{1-x^2}$

Continued on next page

Table A.1 – continued from previous page

l m	$P_l^m(x)$
2 0	$\frac{1}{2}(3x^2-1)$
2 1	$-3x\sqrt{1-x^2}$
2 2	$3(1-x^2)$
3 0	$\frac{1}{2}x(5x^2-3)$
3 1	$-\frac{3}{2}(5x^2-1)\sqrt{1-x^2}$
3 2	$15x(1-x^2)$
3 3	$-15(1-x^2)^{\frac{3}{2}}$
4 0	$\frac{1}{8}(35x^4-30x^2+3)$
4 1	$-\frac{5}{2}(7x^3-3x)\sqrt{1-x^2}$
4 2	$\frac{15}{2}(7x^2-1)(1-x^2)$

Continued on next page

Table A.1 – continued from previous page

l m	$P_l^m(x)$
4 3	$-105x(1-x^2)^{\frac{3}{2}}$
4 4	$105(1-x^2)^2$
5 0	$\frac{1}{8}x(63x^4-70x^2+15)$
5 1	$-\frac{15}{8}\sqrt{1-x^2}(21x^4-14x^2+1)$
5 2	$\frac{105}{2}x(1-x^2)(3x^2-1)$
5 3	$-\frac{105}{2}(1-x^2)^{\frac{3}{2}}(9x^2-1)$
5 4	$945x(1-x^2)^2$
5 5	$-945(1-x^2)^{\frac{5}{2}}$
6 0	$\frac{1}{16}(231x^6-315x^4+105x^2-5)$
6 1	$-\frac{21}{8}x(33x^4-30x^2+5)\sqrt{1-x^2}$

Continued on next page

Table A.1 – continued from previous page

l m	$P_l^m(x)$
6 2	$\frac{105}{8}(1-x^2)(33x^4-18x^2+1)$
6 3	$-\frac{315}{2}(11x^2-3)x(1-x^2)^{\frac{3}{2}}$
6 4	$\frac{945}{2}(1-x^2)^2(11x^2-1)$
6 5	$-10395x(1-x^2)^{\frac{5}{2}}$
6 6	$10395(1-x^2)^3$

A.2 Magnetic scalar potential basis

The basis presented in [3] is defined as follows:

$$\Phi_{l,m} = C_{l,m}(\phi) r^l P_l^{|m|}(\cos\theta) \tag{A.1}$$

with

$$\begin{aligned} C_{l,m}(\phi) &= \frac{(l-1)!(-2)^{|m|}}{(l+|m|)!}\cos(m\phi) && \text{for} \quad m \geq 0 \\ &= \frac{(l-1)!(-2)^{|m|}}{(l+|m|)!}\sin(|m|\phi) && \text{for} \quad m < 0 \end{aligned} \tag{A.2}$$

Here the basis for the magnetic potential is listed, up to $l = 6$. Note that for the cartesian version I leave $r^2 = x^2 + y^2 + z^2$ for the sake of brevity, when calculating the derivatives in the next table the appropriate substitutions are made.

Table A.2: The basis of the magnetic potential sorted by degree.

l m	$\Phi_{l,m}$ **in Spherical Polar**	$\Phi_{l,m}$ **in Cartesian**
1 -1	$r\sin\theta\sin\phi$	y
1 0	$r\cos\theta$	z
1 1	$r\sin\theta\cos\phi$	x
2 -2	$\frac{1}{2}r^2\sin^2\theta\sin(2\phi)$	xy
2 -1	$r^2\cos\theta\sin\theta\sin\phi$	yz
2 0	$\frac{1}{4}r^2(3\cos^2\theta - 1)$	$\frac{1}{4}(3z^2 - y^2 - x^2)$
2 1	$r^2\cos\theta\sin\theta\cos\phi$	xz
2 2	$\frac{1}{2}r^2\sin^2\theta\cos(2\phi)$	$\frac{1}{2}(x^2 - y^2)$

Continued on next page

Table A.2 – continued from previous page

l m	$\Phi_{l,m}$ **in Spherical Polar**	$\Phi_{l,m}$ **in Cartesian**
3 -3	$\frac{1}{3}r^3 \sin^3\theta \sin(3\phi)$	$x^2y - \frac{1}{3}y^3$
3 -2	$r^3 \cos\theta \sin^2\theta \sin(2\phi)$	$2xyz$
3 -1	$\frac{1}{4}r^3(5\cos^2\theta - 1)\sin\theta \sin\phi$	$yz^2 - \frac{1}{4}x^2y - \frac{1}{4}y^3$
3 0	$\frac{1}{6}r^3 \cos\theta(5\cos^2\theta - 3)$	$\frac{1}{3}z^3 - \frac{1}{2}z(x^2 - y^2)$
3 1	$\frac{1}{4}r^3(5\cos^2\theta - 1)\sin\theta \cos\phi$	$xz^2 - \frac{1}{4}x(x^2 + y^2)$
3 2	$r^3 \cos\theta \sin^2\theta \cos(2\phi)$	$z(x^2 - y^2)$
3 3	$\frac{1}{3}r^3 \sin^3\theta \cos(3\phi)$	$\frac{1}{3}x^3 - xy^2$
4 -4	$\frac{1}{4}r^4 \sin^4\theta \sin(4\phi)$	$x^3y - xy^3$
4 -3	$r^4 \cos\theta \sin^3\theta \sin(3\phi)$	$3x^2yz - zy^3$
4 -2	$\frac{1}{4}r^4(7\cos^2 -1)\sin^2\theta \sin(2\phi)$	$3xyz^2 - \frac{1}{2}x^3y - \frac{1}{2}xy^3$
4 -1	$\frac{1}{4}r^4(7\cos^3\theta - 3\cos\theta)\sin\theta \sin\phi$	$yz^3 - \frac{3}{4}z(x^2y - y^3)$

Continued on next page

Table A.2 – continued from previous page

l m	$\Phi_{l,m}$ **in Spherical Polar**	$\Phi_{l,m}$ **in Cartesian**
4 0	$\frac{1}{32}r^4(35\cos^4\theta - 30\cos^2\theta + 3)$	$\frac{1}{4}z^4 - \frac{3}{4}z^2(x^2-y^2) + \frac{3}{32}(x^2+y^2)^2$
4 1	$\frac{1}{4}r^4(7\cos^3\theta - 3\cos\theta)\sin\theta\cos\phi$	$xz^3 - \frac{3}{4}z(x^3 - xy^2)$
4 2	$\frac{1}{4}r^4(7\cos^2\theta - 1)\sin^2\theta\cos(2\phi)$	$\frac{3}{2}z^2(x^2-y^2) + \frac{1}{4}(y^4 - x^4)$
4 3	$r^4\cos\theta\sin^3\theta\cos(3\phi)$	$z(x^3 - 3xy^2)$
4 4	$\frac{1}{4}r^4\sin^4\theta\cos(4\phi)$	$\frac{1}{4}(y^4 + x^4) - \frac{3}{2}x^2y^2$
5 -5	$\frac{1}{5}r^5\sin^5\theta\sin(5\phi)$	$\frac{1}{5}y^5 + yx^4 - 2y^3x^2$
5 -4	$r^5\cos(\theta)\sin^4\theta\sin(4\phi)$	$4xyz(x^2-y^2)$
5 -3	$\frac{1}{4}r^5(9\cos^2\theta - 1)\sin^2\theta\sin(3\phi)$	$6x^2yz^2 - 2y^3z^2 - \frac{1}{2}x^2y^3 - \frac{3}{4}x^4y + \frac{1}{4}y^5$
5 -2	$r^5(3\cos^3\theta - \cos\theta)\sin^2\theta\sin(2\phi)$	$2xyz(2z^2 - x^2 - y^2)$
5 -1	$\frac{1}{8}r^5(21\cos^4\theta - 14cos^2\theta + 1)\sin\theta\sin\phi$	$yz^4 - \frac{3}{2}x^2yz^2 - \frac{3}{2}y^3z^2 +$ $\frac{1}{8}x^4y + \frac{1}{8}y^5 + \frac{1}{4}x^2y^3$

Continued on next page

Table A.2 – continued from previous page

l m	$\Phi_{l,m}$ **in Spherical Polar**	$\Phi_{l,m}$ **in Cartesian**
5 0	$\frac{1}{40}r^5(63\cos^5\theta - 70\cos^3\theta + 15\cos\theta)$	$\frac{1}{5}z^5 - x^2z^3 - y^2z^3 +$ $\frac{3}{8}x^4z + \frac{3}{8}y^4z + \frac{3}{4}x^2y^2z$
5 1	$\frac{1}{8}r^5(21\cos^4\theta - 14\cos^2\theta + 1)\sin\theta\cos\phi$	$xz^4 - \frac{3}{2}x^3z^2 - \frac{3}{2}xy^2z^2 +$ $\frac{1}{8}x^5 + \frac{1}{8}xy^4 + \frac{1}{4}x^3y^2$
5 2	$r^5(3\cos^3\theta - \cos\theta)\sin^2\theta\cos(2\phi)$	$2z^3(x^2 - y^2) + z(y^4 - x^4)$
5 3	$\frac{1}{4}r^5(9\cos^2\theta - 1)\sin^3\theta\cos(3\phi)$	$2x^3z^2 - 6xy^2z^2 - \frac{1}{4}x^5 + \frac{1}{2}x^3y^2 + \frac{3}{4}xy^4$
5 4	$r^5\cos\theta\sin^4\theta\cos(4\phi)$	$z(y^4 + x^4 - 6x^2y^2)$
5 5	$\frac{1}{5}r^5\sin^5\theta\cos(5\theta)$	$\frac{1}{5}x^5 - 2y^2x^3 + y^4x$
6 -6	$\frac{1}{6}r^6\sin^6\theta\sin(6\phi)$	$x^5y - \frac{10}{3}x^3y^3 + xy^5$
6 -5	$r^6\cos\theta\sin^5\theta\sin(5\phi)$	$y^5z + 5x^4yz - 10x^2y^3z$
6 -4	$\frac{1}{4}r^6(11\cos^2\theta - 1)\sin^4\theta\sin(4\phi)$	$10xyz^2(x^2 - y^2) - xy(x^4 - y^4)$
6 -3	$\frac{5}{12}r^6(11\cos^3 - 3\cos\theta)\sin^3\theta\sin(3\phi)$	$10x^2yz^3 - \frac{10}{3}y^3z^3 - \frac{5}{2}x^2y^3z -$ $\frac{15}{4}x^4yz + \frac{15}{12}y^5z$

Continued on next page

Table A.2 – continued from previous page

l m	$\Phi_{l,m}$ **in Spherical Polar**	$\Phi_{l,m}$ **in Cartesian**
6 -2	$\frac{5}{32}r^6(33\cos^4\theta - 18\cos^2\theta + 1)\sin^2\theta\sin(2\phi)$	$5xyz^4 - 5x^3yz^2 - 5xy^3z^2 +$ $\frac{5}{16}x^5y + \frac{5}{16}xy^5 + \frac{5}{8}x^3y^3$
6 -1	$\frac{1}{8}r^6(33\cos^5\theta - 30\cos^3\theta + 5\cos\theta)\sin\theta\sin\phi$	$yz^5 - \frac{5}{2}x^2yz^3 - \frac{5}{2}y^3z^3 +$ $\frac{5}{8}x^4yz + \frac{5}{8}y^5z + \frac{5}{4}x^2y^3z$
6 0	$\frac{1}{96}r^6(231\cos^6\theta - 315\cos^4\theta + 105\cos^2\theta - 5)$	$\frac{1}{6}z^6 - \frac{5}{4}x^2z^4 - \frac{5}{4}y^2z^4 + \frac{15}{16}x^4z^2 + \frac{15}{16}y^4z^2 +$ $\frac{15}{8}x^2y^2z^2 - \frac{5}{96}x^6 - \frac{5}{96}y^6 - \frac{15}{96}x^4y^2 - \frac{15}{96}x^2y^4$
6 1	$\frac{1}{8}r^6(33\cos^5\theta - 30\cos^3\theta + 5\cos\theta)\sin\theta\cos\phi$	$xz^5 - \frac{5}{2}x^3z^3 - \frac{5}{2}xy^2z^3 +$ $\frac{5}{8}x^5z + \frac{5}{8}xy^4z + \frac{5}{4}x^3y^2z$
6 2	$\frac{5}{32}r^6(33\cos^4\theta - 18\cos^2\theta + 1)\sin^2\theta\cos(2\phi)$	$\frac{5}{2}x^2z^4 - \frac{5}{2}y^2z^4 - \frac{5}{2}x^4z^2 + \frac{5}{2}y^4z^2 +$ $\frac{5}{32}x^6 - \frac{5}{32}y^6 - \frac{5}{32}x^2y^4 + \frac{5}{32}x^4y^2$
6 3	$\frac{5}{12}r^6(11\cos^3\theta - 3\cos\theta)\sin^3\theta\cos(3\phi)$	$\frac{10}{3}x^3z^3 - 10xy^2z^3 + \frac{5}{2}x^3y^2z -$ $\frac{5}{4}x^5z + \frac{15}{4}xy^4z$
6 4	$\frac{1}{4}r^6(11\cos^2\theta - 1)\sin^4\theta\cos(4\phi)$	$\frac{5}{2}y^4z^2 - \frac{5}{2}x^4z^2 - 15x^2y^2z^2 + \frac{5}{4}x^2y^4 +$ $\frac{5}{4}x^4y^2 - \frac{1}{4}y^6 - \frac{1}{4}x^6$
6 5	$r^6\cos\theta\sin^5\theta\cos(5\phi)$	$x^5z - 10x^3y^2z + 5xy^4z$

Continued on next page

Table A.2 – continued from previous page

l m	$\Phi_{l,m}$ **in Spherical Polar**	$\Phi_{l,m}$ **in Cartesian**
6 6	$\frac{1}{6}r^6 \sin^6\theta \cos(6\phi)$	$\frac{1}{6}x^6 - \frac{1}{6}y^6 - \frac{5}{2}x^4y^2 + \frac{5}{2}x^2y^4$

Taking derivatives gives us the $\Pi_{x_i,l,m}$ functions. Note that the l in the subscript always refers to the degree of the polynomial in the term itself, not the degree of the legendre polynomial that it came from:

$$\Pi_{x_i,l,m} = \partial_{x_i}\Phi_{l+1,m} \tag{A.3}$$

A.3 Magnetic field harmonic polynomials in x,y,z sorted by degree

Observing the $m = 0$ terms of the Π_z terms, the choice of $C_{l,m}$s is more apparent; they have been chosen so that the leading order z term has no coefficient.

Table A.3: The basis of harmonic polynomials sorted by degree

l m	Π_x	Π_y	Π_z
0 -1	0	1	0
0 0	0	0	1
0 1	1	0	0
1 -2	y	x	0
1 -1	0	z	y
1 0	$-\frac{1}{2}x$	$-\frac{1}{2}y$	z
1 1	z	0	x

Continued on next page

Table A.3 – *Continued from previous page*

l m	Π_x	Π_y	Π_z
1 2	x	$-y$	0
2 -3	$2xy$	$x^2 - y^2$	0
2 -2	$2yz$	$2xz$	$2xy$
2 -1	$-\frac{1}{2}xy$	$\frac{1}{4}(4z^2 - x^2 - 3y^2)$	$2yz$
2 0	$-xz$	$-yz$	$z^2 - \frac{1}{2}(x^2 + y^2)$
2 1	$-\frac{1}{4}(3x^2 + y^2 - 4z^2)$	$-\frac{1}{2}xy$	$2xz$
2 2	$2xz$	$-2yz$	$x^2 - y^2$
2 3	$x^2 - y^2$	$-2xy$	0
3 -4	$3x^2y - y^3$	$x^3 - 3xy^2$	0
3 -3	$6xyz$	$3(x^2z - y^2z)$	$3x^2y - y^3$
3 -2	$-\frac{1}{2}(3x^2y + y^3 - 6yz^2)$	$-\frac{1}{2}(x^3 + 3xy^2 - 6xz^2)$	$6xyz$

Continued on next page

Table A.3 – *Continued from previous page*

l m	Π_x	Π_y	Π_z
3 -1	$-\frac{3}{2}xyz$	$-\frac{1}{4}(3x^2z + 9y^2z - 4z^3)$	$3yz^2 - \frac{3}{4}(x^2y + y^3)$
3 0	$\frac{3}{8}(x^3 + xy^2 - 4xz^2)$	$\frac{3}{8}(x^2y + y^3 - 4yz^2)$	$z^3 - \frac{3}{2}z(x^2 + y^2)$
3 1	$-\frac{1}{4}(9x^2z + 3y^2z - 4z^3)$	$-\frac{3}{2}xyz$	$3xz^2 - \frac{3}{4}(x^3 + xy^2)$
3 2	$-x^3 + 3xz^2$	$-3yz^2 + y^3$	$3(x^2z - y^2z)$
3 3	$3(x^2z - y^2z)$	$-6xyz$	$x^3 - 3xy^2$
3 4	$x^3 - 3xy^2$	$-3x^2y + y^3$	0
4 -5	$4xy(x^2 - y^2)$	$y^4 - 6x^2y^2 + x^4$	0
4 -4	$12x^2yz - 4y^3z$	$4x^3z - 12xy^2z$	$4x^3y - 4xy^3$
4 -3	$xy(12z^2 - 3x^2 - y^2)$	$6x^2z^2 - \frac{3}{4}x^4 - \frac{3}{2}x^2y^2$ $-6y^2z^2 + \frac{5}{4}y^4$	$12x^2yz - 4y^3z$
4 -2	$2yz(2z^2 - 3x^2 - y^2)$	$2xz(2z^2 - x^2 - 3y^2)$	$2xy(6z^2 - x^2 - y^2)$

Continued on next page

Table A.3 – *Continued from previous page*

l m	Π_x	Π_y	Π_z
4 -1	$\frac{1}{2}xy(x^2+y^2-6z^2)$	$z^4-\frac{3}{2}x^2z^2-\frac{9}{2}y^2z^2$ $+\frac{1}{8}x^4+\frac{3}{4}x^2y^2+\frac{5}{8}y^4$	$4yz^3-3x^2yz-3y^3z$
4 0	$xz\left(\frac{3}{2}(y^2+x^2)-2z^2\right)$	$yz\left(\frac{3}{2}(y^2+x^2)-2z^2\right)$	$z^4-3z^2(x^2+y^2)+$ $\frac{3}{8}(x^4+y^4)+\frac{3}{4}x^2y^2$
4 1	$\frac{5}{8}x^4+z^4-\frac{9}{2}x^2z^2-\frac{3}{2}y^2z^2$ $+\frac{3}{4}x^2y^2+\frac{1}{8}y^4$	$xy\left(\frac{1}{2}(x^2+y^2)-3z^2\right)$	$4xz^3-3x^3z-3xy^2z$
4 2	$4xz(x^2-z^2)$	$4yz(y^2-z^2)$	$6z^2(x^2-y^2)+y^4-x^4$
4 3	$6x^2z^2-\frac{5}{4}x^4-6y^2z^2$ $+\frac{3}{2}x^2y^2+\frac{3}{4}y^4$	$-12xyz^2+x^3y+3xy^3$	$4x^3z-12xy^2z$
4 4	$4x^3z-12xy^2z$	$4y^3z-12x^2yz$	$y^4+x^4-6x^2y^2$
4 5	$x^4+y^4-6x^2y^2$	$4xy(y^2-x^2)$	0
5 -6	$5x^4y-10x^2y^3+y65$	$x^5-10x^3y^2+5xy^4$	0
5 -5	$20xyz(x^2-y^2)$	$5z(y^4+x^4-6x^2y^2)$	$y^5+5x^4y-10x^2y^3$

Continued on next page

Table A.3 – *Continued from previous page*

l m	Π_x	Π_y	Π_z
5 -4	$30x^2yz^2 - 5x^4y$ $-10y^3z^2 + y^5$	$10x^3z^2 - 30xy^2z^2 + 5xy^4$	$20xyz(x^2 - y^2)$
5 -3	$5xyz\left(4z^2 - 3x^2 - y^2\right)$	$10x^2z^3 - \frac{15}{4}x^4z - \frac{15}{2}x^2y^2z$ $-10y^2z^3 + \frac{25}{4}y^4z$	$30x^2yz^2 - \frac{15}{4}x^4y - \frac{5}{2}x^2y^3$ $-10y^3z^2 + \frac{5}{4}y^5$
5 -2	$5yz^4 - 15x^2yz^2 - 5y^3z^2$ $+\frac{25}{16}x^4y + \frac{5}{16}y^5 + \frac{15}{8}x^2y^3$	$5xz^4 - 5x^3z^2 - 15xy^2z^2$ $+\frac{5}{16}x^5 + \frac{25}{16}xy^4 + \frac{15}{8}x^3y^2$	$10xyz\left(10z^2 - x^2 - y^2\right)$
5 -1	$\frac{5}{2}xyz(x^2 + y^2 - 2z^2)$	$z^5 - \frac{5}{2}x^2z^3 - \frac{15}{2}y^2z^3$ $+\frac{5}{8}x^4z + \frac{25}{8}y^4z + \frac{15}{4}x^2y^2z$	$5yz^4 - \frac{15}{2}x^2yz^2 - \frac{15}{2}y^3z^2$ $+\frac{5}{8}x^4y + \frac{5}{8}y^5 + \frac{5}{4}x^2y^3$
5 0	$-\frac{5}{2}xz^4 + \frac{15}{4}x^3z^2 + \frac{15}{4}xy^2z^2$ $-\frac{5}{16}x^5 - \frac{5}{8}x^3y^2 - \frac{5}{16}xy^4$	$-\frac{5}{2}yz^4 + \frac{15}{4}y^3z^2 + \frac{15}{4}x^2yz^2$ $-\frac{5}{16}x^4y - \frac{5}{8}x^2y^3 - \frac{5}{16}y^5$	$z^5 - 5x^2z^3 - 5y^2z^3$ $+\frac{15}{8}x^4z + \frac{15}{8}y^4z + \frac{15}{4}x^2y^2z$
5 1	$z^5 - \frac{15}{2}x^2z^3 - \frac{5}{2}y^2z^3$ $+\frac{25}{8}x^4z + \frac{5}{8}y^4z + \frac{15}{4}x^2y^2z$	$-5xyz^3 + \frac{5}{2}xy^3z + \frac{5}{2}x^3yz$	$5xz^4 - \frac{15}{2}x^3z^2 - \frac{15}{2}xy^2z^2$ $+\frac{5}{8}x^5 + \frac{5}{8}xy^4 + \frac{5}{4}x^3y^2$
5 2	$5xz^4 - 10x^3z^2 + \frac{15}{16}x^5$ $-\frac{5}{16}xy^4 + \frac{5}{8}x^3y^2$	$-\frac{5}{8}x^2y^3 + \frac{5}{16}x^4y - 5yz^4$ $+10y^3z^2 - \frac{15}{16}y^5$	$10z^3(x^2 - y^2) + 5z(y^4 - x^4)$

Continued on next page

Table A.3 – *Continued from previous page*

l m	Π_x	Π_y	Π_z
5 3	$10x^2z^3 - \frac{25}{4}x^4z + \frac{15}{2}x^2y^2z$ $-10y^2z^3 + \frac{15}{4}y^4z$	$5xyz(x^2 + 3y^2 - 4z^2)$	$10x^3z^2 - \frac{5}{4}x^5 + \frac{5}{2}x^3y^2$ $-30xy^2z^2 + \frac{15}{4}xy^4$
5 4	$\frac{5}{2}xy^4 + 5x^3y^2 + 10x^3z^2$ $-\frac{3}{2}x^5 - 30xy^2z^2$	$10y^3z^2 + 5x^2y^3 + \frac{5}{2}x^4y$ $-\frac{3}{2}y^5 - 30x^2yz^2$	$5z(y^4 + x^4 - 6x^2y^2)$
5 5	$5z(x^4 + y^4 - 6x^2y^2)$	$20xyz(y^2 - x^2)$	$x^5 - 10x^3y^2 + 5xy^4$
5 6	$x^5 - 10y^2x^3 + 5y^4x$	$-y^5 - 5yx^4 + 10y^3x^2$	0

A.4 Cs vapour cell lifetimes

The lifetimes of various cells were measured at the UofW. Cells 1-5 were on loan from Japan, and our "400 ms" cell was the one used for NMOR in this thesis. Franzen's method of relaxation in the dark was used [16]. See appendix B for a sample of figures.

Cell	γ_s **(Hz)**	γ_f **(Hz)**
1	51	339
2	255	296
3	29.15	231.4
4	13.7	80.4
5	54.3	439
our "100 ms" cell	4.2	33.4
our "400 ms" cell	2.5	49
Uncoated	N/A	N/A

Table A.4: Polarization lifetime measurements for various Cs vapour cells tested at the UofW. The cells are named as they are physically labelled.

Appendix B

Figures

B.1 Parameter optimization

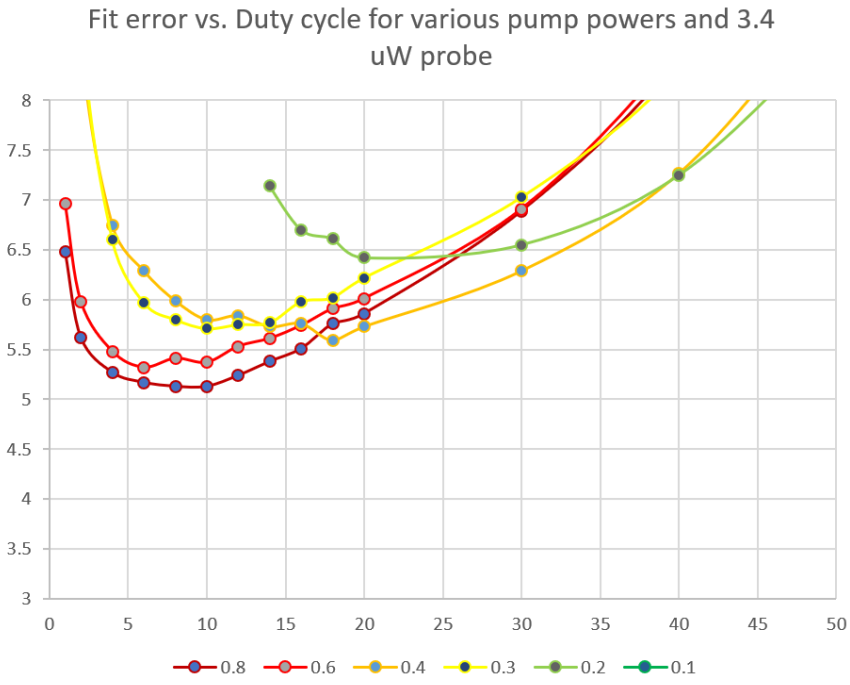

Figure B-1: Probe power = 3.4 μW

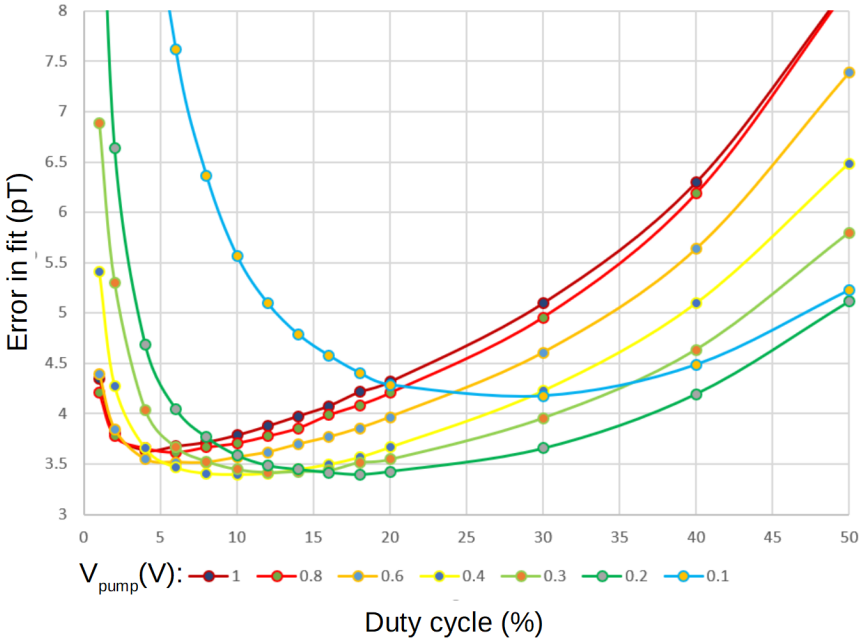

Figure B-2: Probe power = 5.3 μW

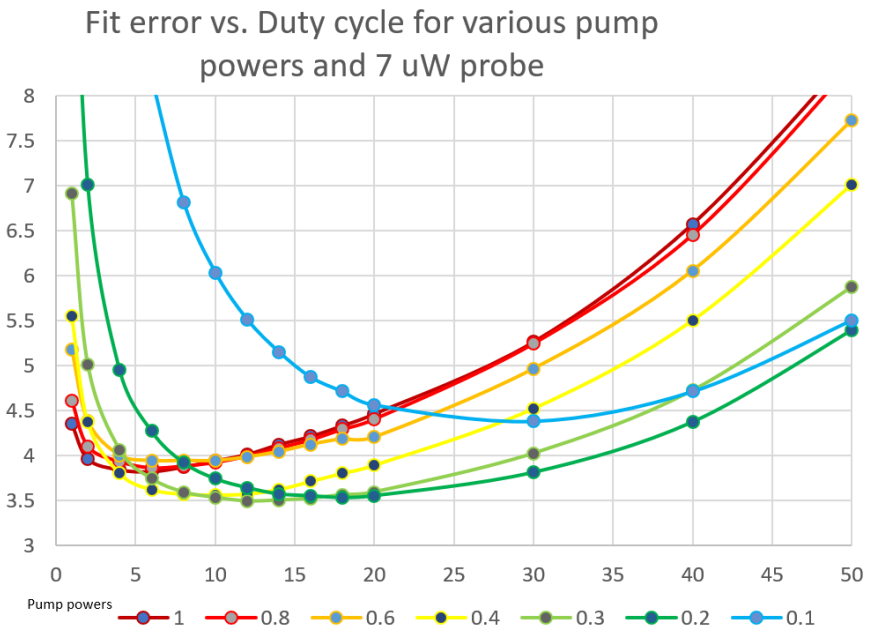

Figure B-3: Probe power = 7 μW

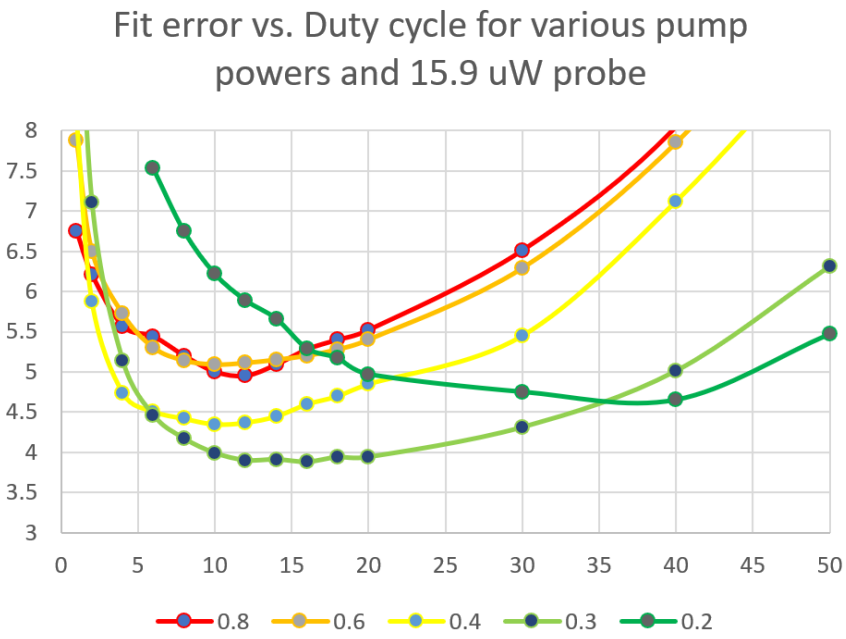

Figure B-4: Probe power = 15.9 μW

B.2 Cs vapour cell lifetimes

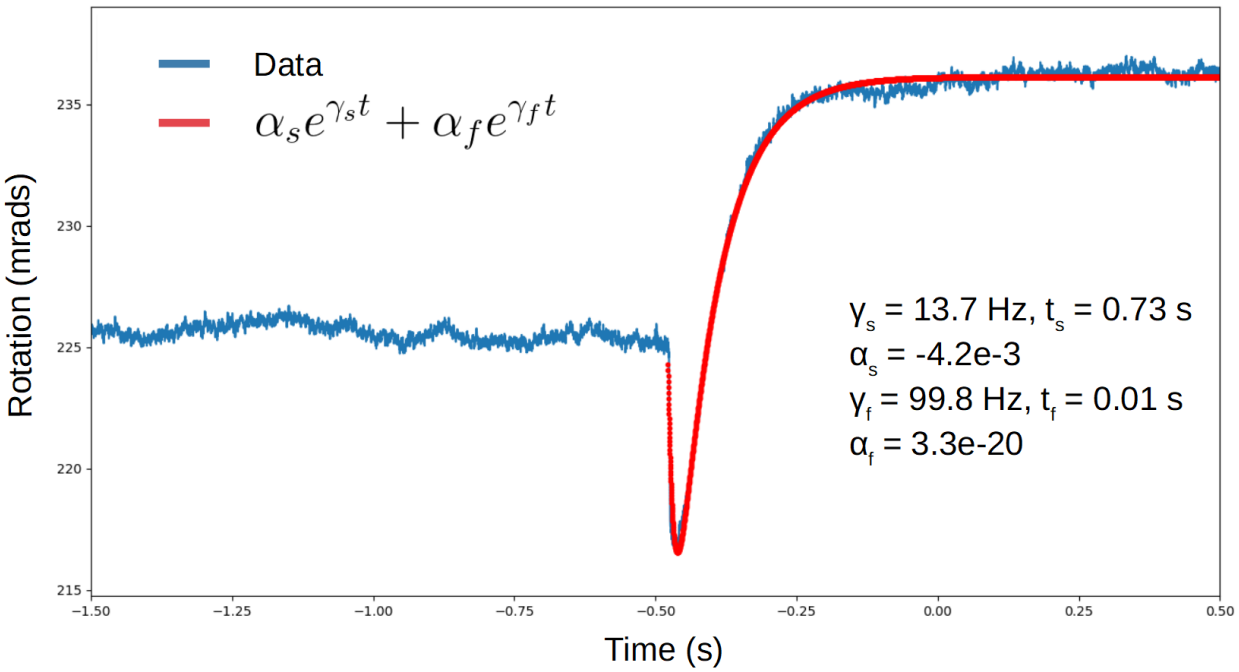

Figure B-5: A lifetime measurement of a Cs cell from Japan. This was the best such cell, cell #4 in table A.4.

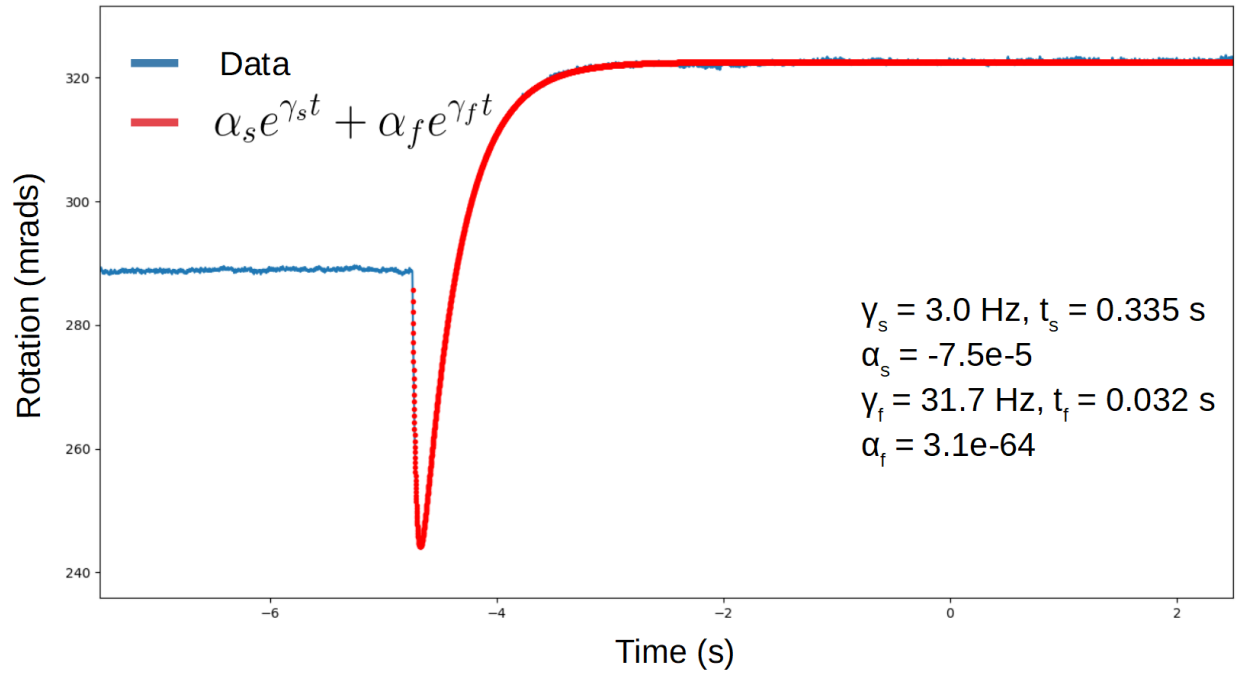

Figure B-6: A lifetime measurement for the Cs cell used for NMOR in this thesis. This is the "400 ms" cell in table A.4.

Appendix C

Code

C.1 Decomposition and optimization code

Here is the code used to run the simulations. The comments are intended to be detailed enough to explain the functions.

```
function extPar = init()
%This function initializes all the constant parameters and structures that
%the calcFitness funtion needs whenever it runs.  This is done only once at
%the beginning of the run, and the extPar structure is passed through to
%everything that needs it.
temp = load('C:\Users\wolfy\Matlab\UofM\gMax.mat');
extPar.gMax = temp.gMax;
extPar.fieldError = 1e-6; % units of uT (1e-6 = 1pT) adjusted as needed
extPar.posError = 0.1; % units of cm adjusted as needed
extPar.Rcell = 18; % units of cm
extPar.Rvac = 50; % units of cm
extPar.Rmsr = 80; % units of cm
```

```
extPar.h1 = 5; % units of cm
extPar.h2 = 20.05; % units of cm
extPar.Hvac = 30; % units of cm
extPar.Hmsr = 80; % units of cm
extPar.numAverages = 20; %adjusted as needed
extPar.cell.radius = 10; % units of cm
extPar.cell.height = 10; % units of cm
extPar.cell.numPosRadius = 10;
extPar.cell.numPosHeight = 10;
end
```

```
function F = fitness(X,extPar)
%%%%%%%%%%%%%%%%%%%%%%%%%%%%%%%
%This function takes requests from Ferret in the form of columns of
%parameters to test.  This returns a column of fitness results, in this
%case chi squared values.
%%%%%%%%%%%%%%%%%%%%%%%%%%%%%%%
[~, N] = size(X);
%N -> number of models requested by Ferret
for model = N:-1:1
    %select a single column of parameters to check
    Xtemp = X(:,model);
    %check parameters, report fitness for each set
    F(model) = calcFitness(Xtemp,extPar,model);
end
end
```

```
function fitness = calcFitness(Xtemp,extPar,model)
pos = reshape(Xtemp,length(Xtemp)./3,3);
penalty = 0;
auxOutput(model).penalty = false;
for i = 1:length(pos(:,1))
    if isPenalty(pos(i,:),extPar) % checks if each position is penalizable
        penalty = penalty + calcPenalty(pos(i,:),extPar);
        auxOutput(model).penalty = true; % sets penalized flag to true if
                                         %even one position is penalized
    end
end
baselines = calcBaselines(pos);%calculates the distance between each set of
                               %points in the position set
if min(baselines)<3%punishes ferret for overlapping positions by 3 cm
    penalty = 1000;
    auxOutput(model).penalty = true;
end
transMatZ = calcTransMatZThird(pos);  %this matrix should be the truncated
%order with no errors AND NO ZEROS, G VECTOR IS SHORTER G(3) = G_10
%transMatZfifth = calcTransMatZFifth(pos);
for n = extPar.numAverages:-1:1
    posErrors = calcPosErrors(pos,extPar.posError);
    g = genGradRandom(extPar);%generate random gradient on the order of the
    %largest expected from the measured uniformity of magnetically shielded
    %rooms G VECTOR IS LONGER, INCLUDES ZERO MODES IN Z, G(6) = G_10
```

```
    dReal = calcdFalseFifth(extPar.Rcell,extPar.h1,extPar.h2,g); %dReal
    %should always be calculated to the highest order with no errors
    for j = length(posErrors):-1:1%cal
        Bfield(j,1) = calcBavg(extPar,posErrors(j,:),g) + ...
            randn.*extPar.fieldError;
    end
    g_fit = calcGrad(Bfield,transMatZ);%truncated order, NO ERR IN TRANSMAT
    dFit = calcdFalseThird(extPar.Rcell,extPar.h1,extPar.h2,g_fit);
                                                        %truncated order
    fitness(n) = penalty + abs(dFit - dReal);%goal is for this to be as
    %low as possible for any arbitrary g
end
fitness = mean(fitness);
end
```

```
function posErrors = calcPosErrors(pos,posError)
%calcPosErrors takes in a set of positions and adds a random gaussian error
%with a sigma equal to the positioning error defined in extPar.
posErrors(:,1) = pos(:,1) + posError.*(randn(length(pos),1));
posErrors(:,2) = pos(:,2) + posError.*(randn(length(pos),1));
posErrors(:,3) = pos(:,3) + posError.*(randn(length(pos),1));
end
```

```
function isPenalty = isPenalty(pos,extPar)
rho = sqrt(pos(1).^2 + pos(2).^2);
z = pos(3);
if and(rho<extPar.Rvac,abs(z)<extPar.Hvac)
    isPenalty = true;
else
    isPenalty = false;
end
end
```

```
function penalty = calcPenalty(pos,extPar)
penalty = 0;
x = 0;
rho = sqrt(pos(1).^2 + pos(2).^2);%put into cylindrical coordinates
z = pos(3);
if rho>=abs(z)
    x = extPar.Rvac./rho;
elseif abs(z)>rho
    x = extPar.Hvac./abs(z);
end
penalty = penalty + (x-1).^4;
end
```

```
function g = genGradRandom(extPar)
%generates a random gradient vector, with values large enough to have a
%1e-27 dFalse contribution.  Units are microtesla/cm^(ell), where ell is
%the degree of the polynomial associated with the gradient term.
%values are generated to be on the order of the largest gradients we might
%expect to encounter, as caluated using 3 nT variation in the volume.
for i = 48:-1:4
    g(i) = (2*rand - 1)*extPar.gMax(i);
end
g(1) = (2*rand - 1)*1e-3;%transverse (X&Y) fields set to ~nT scale
g(3) = (2*rand - 1)*1e-3;%transverse (X&Y) fields set to ~nT scale
g(2) = 1;%Bz set to 1 uT
g = g';
end
```

```
function dFalse = calcdFalseFifth(R,h1,h2,g)
% calcdFalse calulates the mercury contribution to the false EDM signal,
% given a precession volume with radius R in cm, height h1 in cm above the
%origin, and total height (h2-h1) in cm, and given the gradient vector g.
%This calculation assumes the gradient vector is given in units of
%microtesla/cm^{ell}, where ell is the degree of the polynomial associated
%with the gradient term.  This version calculates up to fifth order.  It
%also assumes the full 48 term gradient vector, where G(6) = G_10
dFalse = 8e-30*(R^2)*(g(6)*1e6 + g(12)*1e6*(h2+h1) - ...
    (g(20)*1e6/2)*(R^2 - 2*h1^2 - 2*h1*h2 - 2*h2^2) + ...
    (g(30)*1e-6)*((R.^2).*((h2^2 - h1^2)/(h2 - h1)) - ...
```

```
        (h2^4 - h1^4)/(h2 - h1)) + ...
    (g(42)*1e-6)*(-(h2^5 - h1^5)/(h2 - h1) + ...
        5*((R^2)/3)*(h2^3 - h1^3)/(h2 - h1) - (5*R^6)/(16)));
end
```

```
function transMat = calcTransMatZThird(pos)
%calcTransMat takes in a 3-by-numPos matrix of positions, and calculates
%the trans. matrix between the Bz field space and the gradient space.
%This version calculates up to third order.  In order for
%calcGrad to solve for g_fit, which excludes the zero modes in z, this
%version also excludes the zero modes.  This shouldn't effect the higher
%order versions which calculate the full field.
x = pos(:,1);
y = pos(:,2);
z = pos(:,3);
transMat = zeros(length(pos),16);
transMat(:,1) = 1;%
transMat(:,2) = y;%
transMat(:,3) = z;%
transMat(:,4) = x;%
transMat(:,5) = 2.*x.*y;%
transMat(:,6) = 2.*y.*z;%
transMat(:,7) = z.^2 - 0.5.*(x.^2 + y.^2);%
transMat(:,8) = 2.*x.*z;%
transMat(:,9) = x.^2 - y.^2;%
transMat(:,10) = 3.*x.^2.*y - y.^3;%
```

```
transMat(:,11) = 6.*x.*y.*z;%
transMat(:,12) = 3.*y.*z.^2 - 0.75.*(x.^2.*y + y.^3);%
transMat(:,13) = z.^3 - 1.5.*z.*(x.^2 + y.^2);%
transMat(:,14) = 3.*x.*z.^2 - 0.75.*(x.^3 + x.*y.^2);%
transMat(:,15) = 3.*z.*(x.^2 - y.^2);%
transMat(:,16) = x.^3 - 3.*x.*y.^2;%
end
```

```
function Bavg = calcBavg(extPar,pos,g)
%calcBavg returns the average Bfield over the input points "pos" for a
%given magnetic field described by "g"
transMat(:,:,1) = calcTransMatXFifth(pos); % These should be
transMat(:,:,2) = calcTransMatYFifth(pos); % to the highest
transMat(:,:,3) = calcTransMatZFifth(pos); % order, with errors
Bfield = calcBfield(transMat,g);
Bavg = mean(Bfield);
end
```

```
function posCell = genPosCell(cell,pos)
%genPosCell generates a list of positions that are within a cylindrical
%volume with radius "cell.radius" and a hieght/depth of "cell.height",
%centered on the input position "pos".  cell.numPosRadius/cell.radius
%describes the density of points along the x and y axis,
%cell.numPosHeight/cell.height describes the density of points along the z
%axis.
x = linspace(pos(1) - cell.radius,pos(1) + cell.radius,cell.numPosRadius);
y = linspace(pos(2) - cell.radius,pos(2) + cell.radius,cell.numPosRadius);
```

```
z = linspace(pos(3) - cell.height,pos(3) + cell.height,cell.numPosHeight);
[X,Y,Z] = ndgrid(x,y,z);
grid = [X(:),Y(:),Z(:)];
posCell = grid((((grid(:,1) - pos(1)).^2 + (grid(:,2)...
    - pos(2)).^2) < cell.radius),:);
end
```

```
function transMat = calcTransMatXFifth(pos)
%calcTransMat takes in a 3-by-numPos matrix of positions, and calculates
%the trans. matrix between the Bz field space and the gradient space.
%This version calculates up to fifth order.
%Feb 2020: checked all terms up to order 5 with Maedeh Lavvaf, corrected a
%bunch of typos.  Check was done both by hand and using Jeffs Pis.py
%program.
x = pos(:,1);
y = pos(:,2);
z = pos(:,3);
transMat = zeros(length(pos),24);
transMat(:,1) = 0;%
transMat(:,2) = 0;%
transMat(:,3) = 1;%
transMat(:,4) = y;%
transMat(:,5) = 0;%
transMat(:,6) = -0.5.*x;%
transMat(:,7) = z;%
transMat(:,8) = x;%
```

```
transMat(:,9) = 2.*x.*y;%
transMat(:,10) = 2.*y.*z;%
transMat(:,11) = -0.5.*x.*y;%
transMat(:,12) = -x.*z;%
transMat(:,13) = -0.25.*(3.*x.^2 + y.^2 - 4.*z.^2);%
transMat(:,14) = 2.*x.*z;%
transMat(:,15) = x.^2 - y.^2;%
transMat(:,16) = 3.*(x.^2).*y - y.^3;%
transMat(:,17) = 6.*x.*y.*z;%
transMat(:,18) = -0.5.*(3.*(x.^2).*y + y.^3 - 6.*y.*(z.^2));%
transMat(:,19) = -1.5.*x.*y.*z;%
transMat(:,20) = (3/8).*(x.^3 + x.*(y.^2) - 4.*x.*(z.^2));%
transMat(:,21) = -0.25.*(9.*(x.^2).*z + 3.*(y.^2).*z - 4.*(z.^3));%
transMat(:,22) = -x.^3 + 3.*x.*(z.^2);%
transMat(:,23) = 3.*((x.^2).*z - (y.^2).*z);%
transMat(:,24) = x.^3 - 3.*x.*(y.^2);%
transMat(:,25) = 4.*x.*y.*(x.^2 - y.^2);%
transMat(:,26) = 12.*(x.^2).*y.*z - 4.*(y.^3).*z;%
transMat(:,27) = x.*y.*(12.*(z.^2) - 3.*(x.^2) - y.^2);%
transMat(:,28) = 2.*y.*z.*(2.*(z.^2) - 3.*(x.^2) - y.^2);%
transMat(:,29) = 0.5.*x.*y.*(x.^2 + y.^2 - 6.*(z.^2));%
transMat(:,30) = x.*z.*(1.5.*(y.^2 + x.^2) - 2.*(z.^2));%
transMat(:,31) = z.^4 - (9/2).*(x.^2).*(z.^2) - (3/2).*(y.^2).*(z.^2) + ...
    0.75.*(x.^2).*(y.^2) + 0.125.*y.^4 + (5/8).*x.^4;%
transMat(:,32) = 4.*x.*z.*(-(x.^2) + z.^2);%
transMat(:,33) = 6.*(x.^2).*(z.^2) - 1.25.*(x.^4) - 6.*(y.^2).*(z.^2) + ...
```

```
    1.5.*(x.^2).*(y.^2) + 0.75.*(y.^4);%
transMat(:,34) = 4.*(x.^3).*z - 12.*x.*(y.^2).*z;%
transMat(:,35) = x.^4 + y.^4 - 6.*(x.^2).*(y.^2);%
transMat(:,36) = 5.*(x.^4).*y - 10.*(x.^2).*(y.^3) + y.^5;%
transMat(:,37) = 20.*x.*y.*z.*(x.^2 - y.^2);%
transMat(:,38) = 30.*(x.^2).*y.*(z.^2) - 5.*(x.^4).*y -...
    10.*(y.^3).*(z.^2) + y.^5;%
transMat(:,39) = 5.*x.*y.*z.*(4.*(z.^2) - 3.*x.^2 - (y.^2));%
transMat(:,40) = 5.*y.*(z.^4) - 15.*(x.^2).*y.*(z.^2) - ...
    5.*(y.^3).*(z.^2) + (25/16).*(x.^4).*y + (5/16).*(y.^5) + ...
    (15/8).*(x.^2).*(y.^3);%
transMat(:,41) = (5/2).*x.*y.*z.*(x.^2 + y.^2 - 2.*(z.^2));%
transMat(:,42) = -(5/2).*x.*(z.^4) + (15/4).*(x.^3).*(z.^2) + ...
    (15/4).*x.*(y.^2).*(z.^2) - (5/16).*(x.^5) - ...
    (5/8).*(x.^3).*(y.^2) - (5/16).*x.*(y.^4);%
transMat(:,43) = (z.^5) - (15/2).*(x.^2).*(z.^3) - ...
    (5/2).*(y.^2).*(z.^3) + (25/8).*(x.^4).*z + (5/8).*(y.^4).*z + ...
    (15/4).*(x.^2).*(y.^2).*z;%
transMat(:,44) = 5.*x.*(z.^4) - 10.*(x.^3).*(z.^2) + (15/16).*x.^5 - ...
    (5/16).*x.*(y.^4) + (5/8).*(x.^3).*(y.^2);%
transMat(:,45) = 10.*(x.^2).*(z.^3) - (25/4).*(x.^4).*z + ...
    (15/2).*(x.^2).*(y.^2).*z - 10.*(y.^2).*(z.^3) + (15/4).*(y.^4).*z;%
transMat(:,46) = 2.5.*x.*(y.^4) + 5.*(x.^3).*(y.^2) + 10.*(x.^3).*(z.^2)...
    - 1.5.*(x.^5) - 30.*x.*(y.^2).*(z.^2);%
transMat(:,47) = 5.*z.*(x.^4 + y.^4 - 6.*(x.^2).*(y.^2));%
transMat(:,48) = x.^5 - 10.*(y.^2).*(x.^3) + 5.*(y.^4).*x;%
```

```
end
```

```
function transMat = calcTransMatYFifth(pos)
%calcTransMat takes in a 3-by-numPos matrix of positions, and calculates
%the trans. matrix between the Bz field space and the gradient space.
%This version calculates up to fifth order.
%Feb 2020: checked all terms up to order 5 with Maedeh Lavvaf, corrected a
%bunch of typos.  Check was done both by hand and using Jeffs Pis.py
%program.
x = pos(:,1);
y = pos(:,2);
z = pos(:,3);
transMat = zeros(length(pos),48);
transMat(:,1) = 1;%
transMat(:,2) = 0;%
transMat(:,3) = 0;%
transMat(:,4) = x;%
transMat(:,5) = z;%
transMat(:,6) = -0.5*y;%
transMat(:,7) = 0;%
transMat(:,8) = -y;%
transMat(:,9) = x.^2 - y.^2;%
transMat(:,10) = 2.*x.*z;
transMat(:,11) = -0.25.*(x.^2 + 3.*y.^2 - 4.*z.^2);
transMat(:,12) = -y.*z;%
transMat(:,13) = -0.5.*x.*y;%
```

```
transMat(:,14) = -2.*y.*z;%
transMat(:,15) = -2.*x.*y;%
transMat(:,16) = x.^3 - 3.*x.*y.^2;%
transMat(:,17) = 3.*((x.^2).*z - (y.^2).*z);%
transMat(:,18) = -0.5.*(x.^3 + 3.*x.*(y.^2) - 6.*x.*(z.^2));%
transMat(:,19) = -0.25.*(3.*(x.^2).*z + 9.*(y.^2).*z - 4.*z.^3);%
transMat(:,20) = (3/8).*((x.^2).*y + y.^3 - 4.*y.*(z.^2));%
transMat(:,21) = -1.5.*x.*y.*z;%
transMat(:,22) = -3.*y.*(z.^2) + y.^3;%
transMat(:,23) = -6.*x.*y.*z;%
transMat(:,24) = -3.*(x.^2).*y + y.^3;%
transMat(:,25) = y.^4 - 6.*(x.^2).*(y.^2) + x.^4;%
transMat(:,26) = 4.*(x.^3).*z - 12.*x.*(y.^2).*z;%
transMat(:,27) = 6.*(x.^2).*(z.^2) - 0.75.*(x.^4) - 1.5.*(x.^2).*(y.^2)...
    - 6.*(y.^2).*(z.^2) + (5/4).*(y.^4);%
transMat(:,28) = 2.*x.*z.*(2.*(z.^2) - x.^2 - 3.*(y.^2));%
transMat(:,29) = z.^4 - (3/2).*(x.^2).*(z.^2) - (9/2).*(y.^2).*(z.^2) + ...
    0.125.*(x.^4) + 0.75.*(x.^2).*(y.^2) + (5/8).*(y.^4);%
transMat(:,30) = y.*z.*(1.5.*(x.^2 + y.^2) - 2.*(z.^2));%
transMat(:,31) = x.*y.*(0.5.*(x.^2 + y.^2) - 3.*(z.^2));%
transMat(:,32) = 4.*y.*z.*(y.^2 - z.^2);%
transMat(:,33) = -12.*x.*y.*(z.^2) + (x.^3).*y + 3.*x.*(y.^3);%
transMat(:,34) = 4.*(y.^3).*z - 12.*(x.^2).*y.*z;%
transMat(:,35) = 4.*x.*y.*(y.^2 - x.^2);%
transMat(:,36) = x.^5 - 10.*(x.^3).*(y.^2) + 5.*x.*y.^4;%
transMat(:,37) = 5.*z.*(y.^4 + x.^4 - 6.*(x.^2).*(y.^2));%
```

```
transMat(:,38) = 10.*(x.^3).*(z.^2) - 30.*x.*(y.^2).*(z.^2) +...
    5.*x.*(y.^4) - x.^5;
transMat(:,39) = 10.*(x.^2).*(z.^3) - (15/4).*(x.^4).*z - ...
    (15/2).*(x.^2).*(y.^2).*z - 10.*(y.^2).*(z.^3) + (25/4).*(y.^4).*z;%
transMat(:,40) = 5.*x.*(z.^4) - 5.*(x.^3).*(z.^2) - ...
    15.*x.*(y.^2).*(z.^2) + (5/16).*(x.^5) + (25/16).*x.*(y.^4) + ...
    (15/8).*(x.^3).*(y.^2);%
transMat(:,41) = z.^5 - 2.5.*(x.^2).*(z.^3) - (15/2).*(y.^2).*(z.^3) + ...
    (5/8).*(x.^4).*z + (25/8).*(y.^4).*z + (15/4).*(x.^2).*(y.^2).*z;%
transMat(:,42) = -2.5.*y.*(z.^4) + (15/4).*(y.^3).*(z.^2) + ...
    (15/4).*(x.^2).*y.*(z.^2) - (5/16).*(x.^4).*y - ...
    (5/8).*(x.^2).*(y.^3) - (5/16).*(y.^5);%
transMat(:,43) = -5.*x.*y.*(z.^3) + (5/2).*x.*(y.^3).*z + ...
    (5/2).*(x.^3).*y.*z;%
transMat(:,44) = -(5/8).*(x.^2).*(y.^3) + (5/16).*(x.^4).*y - ...
    5.*y.*(z.^4) + 10.*(y.^3).*(z.^2) - (15/16).*(y.^5);%
transMat(:,45) = 5.*x.*y.*z.*(x.^2 + 3.*(y.^2) - 4.*(z.^2));%
transMat(:,46) = 10.*(y.^3).*(z.^2) + 5.*(x.^2).*(y.^3) + ...
    (5/2).*(x.^4).*y - 1.5.*(y.^5) - 30.*(x.^2).*y.*(z.^2);%
transMat(:,47) = 20.*x.*y.*z.*(y.^2 - x.^2);%
transMat(:,48) = -y.^5 - 5.*y.*(x.^4) + 10.*(y.^3).*(x.^2);%
end
```

```
function transMat = calcTransMatZFifth(pos)
%calcTransMat takes in a 3-by-numPos matrix of positions, and calculates
%the trans. matrix between the Bz field space and the gradient space.
%This version calculates up to fifth order.
x = pos(:,1);
y = pos(:,2);
z = pos(:,3);
transMat = zeros(length(pos),24);
transMat(:,1) = 0;%
transMat(:,2) = 1;%
transMat(:,3) = 0;%
transMat(:,4) = 0;%
transMat(:,5) = y;%
transMat(:,6) = z;%
transMat(:,7) = x;%
transMat(:,8) = 0;%
transMat(:,9) = 0;%
transMat(:,10) = 2.*x.*y;%
transMat(:,11) = 2.*y.*z;%
transMat(:,12) = z.^2 - 0.5.*(x.^2 + y.^2);%
transMat(:,13) = 2.*x.*z;%
transMat(:,14) = x.^2 - y.^2;%
transMat(:,15) = 0;%
transMat(:,16) = 0;%
transMat(:,17) = 3.*x.^2.*y - y.^3;%
```

```
transMat(:,18) = 6.*x.*y.*z;%
transMat(:,19) = 3.*y.*z.^2 - 0.75.*(x.^2.*y + y.^3);%
transMat(:,20) = z.^3 - 1.5.*z.*(x.^2 + y.^2);%
transMat(:,21) = 3.*x.*z.^2 - 0.75.*(x.^3 + x.*y.^2);%
transMat(:,22) = 3.*z.*(x.^2 - y.^2);%
transMat(:,23) = x.^3 - 3.*x.*y.^2;%
transMat(:,24) = 0;%
transMat(:,25) = 0;%
transMat(:,26) = 4.*(x.^3).*y - 4.*x.*(y.^3);%
transMat(:,27) = 12.*(x.^2).*y.*z - 4.*(y.^3).*z;%
transMat(:,28) = 2.*x.*y.*(6.*(z.^2) - x.^2 - y.^2);%
transMat(:,29) = 4.*y.*(z.^3) - 3.*(x.^2).*y.*z - 3.*(y.^3).*z;%
transMat(:,30) = z.^4 - 3.*(z.^2).*(x.^2 + y.^2) + ...
    (3/8).*(x.^4 + y.^4) + 0.75.*(x.^2).*(y.^2);%
transMat(:,31) = 4.*x.*z.^3 - 3.*x.^3.*z - 3.*x.*y.^2.*z;%
transMat(:,32) = 6.*(z.^2).*(x.^2 - y.^2) + y.^4 - x.^4;%
transMat(:,33) = 4.*(x.^3).*z - 12.*x.*(y.^2).*z;%
transMat(:,34) = y.^4 + x.^4 - 6.*(x.^2).*(y.^2);%
transMat(:,35) = 0;%
transMat(:,36) = 0;%
transMat(:,37) = y.^5 + 5.*(x.^4).*y - 10.*(x.^2).*(y.^3);%
transMat(:,38) = 20.*x.*y.*z.*(x.^2 - y.^2);%
transMat(:,39) = 30.*(x.^2).*y.*(z.^2) - (15/4).*(x.^4).*y - ...
    (5/2).*(x.^2).*(y.^3) - 10.*(y.^3).*(z.^2) + (5/4).*(y.^5);%
transMat(:,40) = 10.*x.*y.*z.*(2.*(z.^2) - x.^2 - y.^2);%
transMat(:,41) = 5.*y.*(z.^4) - (15/2).*(x.^2).*y.*(z.^2) - ...
```

```
    (15/2).*(y.^3).*(z.^2) + (5/8).*(x.^4).*y + (5/8).*(y.^5) + ...
    (5/4).*(x.^2).*(y.^3);%
transMat(:,42) = z.^5 - 5.*(x.^2).*(z.^3) - 5.*(y.^2).*(z.^3) + ...
    (15/8).*(x.^4).*z + (15/8).*(y.^4).*z + (15/4).*(x.^2).*(y.^2).*z;%
transMat(:,43) = 5.*x.*(z.^4) - (15/2).*(x.^3).*(z.^2) - ...
    (15/2).*x.*(y.^2).*(z.^2) + (5/8).*(x.^5) + (5/8).*x.*(y.^4) + ...
    (5/4).*(x.^3).*(y.^2);%
transMat(:,44) = 10.*(z.^3).*(x.^2 - y.^2) + 5.*z.*(y.^4 - x.^4);%
transMat(:,45) = 10.*(x.^3).*(z.^2) - (5/4).*(x.^5) + ...
    2.5.*(x.^3).*(y.^2) - 30.*x.*(y.^2).*(z.^2) + (15/4).*x.*(y.^4);%
transMat(:,46) = 5.*z.*(y.^4 + x.^4 - 6.*(x.^2).*(y.^2));%
transMat(:,47) = x.^5 - 10.*(x.^3).*(y.^2) + 5.*x.*(y.^4);%
transMat(:,48) = 0;%
end
```

```
function Bmod = calcBfield(transMat,g)
%calcBfieldErrors calculates Bx, By, and Bz using their various
%transformation matrices.  Then it calculates Bmod, which is then reported
%as the output.  This value is later used as Bz for the purposes of fitting
%to the harmonic functions. transMat is a vector of 3 transformation
%matrices, one for each dimension
Bx = transMat(:,:,1)*g;
By = transMat(:,:,2)*g;
Bz = transMat(:,:,3)*g;
Bmod = sqrt(Bx.^2 + By.^2 + Bz.^2);
end
```

```
function g_fit = calcGrad(B,transMat)
%calcGrad is essentially a wrapper around the "pinv" function, to
%make my other code more readable.  This also allows modifications to be
%made in the future to how this is done.
g_fit = pinv(transMat)*B;
end
```

```
function dFalse = calcdFalseThird(R,h1,h2,g)
% calcdFalse calulates the mercury contribution to the false EDM signal,
% given a precession volume with radius R in cm, height h1 in cm above the
%origin, and total height (h2-h1) in cm, and given the gradient vector g.
%This calculation assumes the gradient vector is given in units of
%microtesla/cm^{ell}, where ell is the degree of the polynomial associated
%with the gradient term.  This version calculates up to third order, and
%expects the shorter G vector, where G(3) = G_10
dFalse = 8e-30*(R^2)*(g(3)*1e6 + g(7)*1e6*(h2+h1) - ...
    (g(13)*1e6/2)*(R^2 - 2*h1^2 - 2*h1*h2 - 2*h2^2));
end
```

C.2 Data collection and analysis code

Here is the code used to set up experimental equipment and execute measurements. The comments are intended to be detailed enough to explain the functions. I do not include the visualization function "showData.m" or the utility "savefast.m" although neither are built in Matlab functions. These functions do not impact the data being gathered.

```
function collectData()
%% %%%%%%%%%%%%%%%%%%%%Wolfgang Klassen, August 2018%%%%%%%%%%%%%%%%%%%%
%
%This function sets up, executes, and analyses a 100 second magnetic field
%measurement with the Cs atomic magnetometer installed at the UofW.
%
%setup() establishes a connection with the instruments required for the
%measurent, and applies the neccesary settings.  The program prompts the
%user to enter various settings used for the measurement, such as the pump
%frequency
%%%%%%%%%%%%%%%%%%%%%%%%%%%%%%%%%%%%%%%%%%%%%%%%%%%%%%%%%%%%%%%%%%%%%%%%
%% %%%%%%%%%%%%%%%%%%%%%%%%%%%%%%%setup%%%%%%%%%%%%%%%%%%%%%%%%%%%%%%%%%
extPar = setup();
%% %%%%%%%%%%%%%%%%%%%%%%%%%%%%%collect data%%%%%%%%%%%%%%%%%%%%%%%%%%%%%
data = getData(extPar);
%% %%%%%%%%%%%%%%%%%%%%%%%%%%%%%%fit data%%%%%%%%%%%%%%%%%%%%%%%%%%%%%%%%
[data,fitPar] = fitData(extPar,data);
%% %%%%%%%%%%%%%%%%%%%%%%%%%%%%%%show data%%%%%%%%%%%%%%%%%%%%%%%%%%%%%%%
showData(extPar,data,fitPar); %for visualization only
%% %%%%%%%%%%%%%%%%%%%%%%%%%%%%%Save and finish%%%%%%%%%%%%%%%%%%%%%%%%%%
```

```
saveFolder = [pwd '\Data\' extPar.month{1} '\' num2str(extPar.day) '\'];
if ~exist(saveFolder, 'dir')
    mkdir(saveFolder)
end
disp('Saving external parameters...');
savefast([saveFolder extPar.saveName '_extPar.mat'],'extPar');
disp('Saving data...');
savefast([saveFolder extPar.saveName '_data.mat'],'data');
disp('Saving fit parameters...');
savefast([saveFolder extPar.saveName '_fitPar.mat'],'fitPar');
fclose(extPar.GPIB1);
clear extPar;
clear data;
clear fitPar;
end
```

```
function extPar = setup()
%%%%%%%%%%%%%%%%%%%%%%%%%%%%%%%%%%%%%%%%%%%%%%%%%%%%%%%%%%%%%%%%%%%%%%%%%%%%%%%
%%                        Wolfgang Klassen, May 2019
%
%This function sets up the lock-in amplifier, the function generator, the
%power supply, the Keithley multimeter, and the Tektronix DPO 4054
%Oscilloscope to do Free Induction Decay measurements.
%
%%%%%%%%%%%%%%%%%%%%%%%%%%%%%%%%%%%%%%%%%%%%%%%%%%%%%%%%%%%%%%%%%%%%%%%%%%%%%%%
%% %%%%%%%%%%%%%%%%%%%%%%Set up GPIB controller%%%%%%%%%%%%%%%%%%%%%%%%%%%%%%%
```

```
disp('**************setting up instruments**************');
extPar = load('GPIB_controller.mat','GPIB1');
fopen(extPar.GPIB1);%open serial port
fprintf(extPar.GPIB1,'++mode 1');%sets GPIB converter to controller mode
pause(0.1)
fprintf(extPar.GPIB1,'++auto 1');%sets GPIB to ask for response
   automatically
pause(0.1)
fprintf(extPar.GPIB1,'++ver');
pause(0.1)
txt = fgets(extPar.GPIB1);
disp(['Controlling GPIB interface with ' txt])
disp('Press any key to continue if GPIB controller was identified.')
pause;
disp('Continuing setup...')
%% %%%%%%%%%%%%%%%%%%%%%%%%%%set in code%%%%%%%%%%%%%%%%%%%%%%%%%%%%%%
configLockin = 0;
configAWG = 1;
configDMM = 0;
configPS = 0;
extPar.pump.AOMamplitude = 0.4;
extPar.coilCurr = 10;
extPar.month = month(datetime,'name');
extPar.day = day(datetime);
%% %%%%%%%%%%%%%%%%%%%%%%%%%%user inputs%%%%%%%%%%%%%%%%%%%%%%%%%%%%%%%
extPar.lockin.sens = 'N/A';
```

```
extPar.lockin.tConst = 'N/A';
extPar.lockin.center = 'N/A';
extPar.lockin.offset = 'N/A';
if configLockin
    prompt = 'Lock-in sensitivity: ';
    extPar.lockin.sens = input(prompt);
    prompt = 'Lock-in time constant: ';
    extPar.lockin.tConst = input(prompt);
    prompt = 'Demodulation offset (Hz): ';
    extPar.lockin.offset = input(prompt);
end
prompt = 'Center of NMOR signal (Hz): ';
extPar.pump.center = input(prompt);
if configAWG
    prompt = 'AOM duty cycle (%): ';
    extPar.pump.dCycle = input(prompt);
    prompt = 'Rate of FIDs (Multiple of 5 Hz): ';
    extPar.pump.FIDrate = input(prompt);
    extPar.pump.triggertime = 1./extPar.pump.FIDrate;
    prompt = 'Number of cycles in the burst: ';
    extPar.pump.nCycles = input(prompt);
end
if configPS
    prompt = 'Coil current (mA): ';
    extPar.coilCurr = input(prompt);
end
```

```
extPar.numFIDs = extPar.pump.FIDrate.*100;
prompt = 'Degauss: y/n? ';
degauss = input(prompt,'s');
prompt = 'Please check the laser tune in mA: ';
extPar.tune = input(prompt);
prompt = 'Choose a name for this run : ';
extPar.saveName = input(prompt,'s');
%% %%%%%%%%%%%%%%%%%%%%Set up VISA communication%%%%%%%%%%%%%%%%%%%%%%%%
%create the serial interface object to communicate with the scope
extPar.scopeVisa = visa('TEK', 'USB::0x0699::0x0401::C011321::INSTR');
% Disconnect from instrument object, just to make sure
fclose(extPar.scopeVisa);
%create the scope onject that uses the MATLAB driver for the scope
extPar.scope = icdevice('DPO4054.mdd', extPar.scopeVisa);
%This step has to be done AFTER creating the instrument object, apparently
%it resets the buffer size.  Size has to be twice as large as the amount of
%data you're getting (for x and y) plus a small amount for overhead.
set(extPar.scopeVisa, 'InputBufferSize', 20050000);
%This is enough to read 10000000 points
set(extPar.scopeVisa, 'OutputBufferSize', 5000);
connect(extPar.scope);
%% %%%%%%%%%%%%%%%%%%%%setup the SR830 DSP Lock-in%%%%%%%%%%%%%%%%%%%%%%%%
if configLockin
    fprintf(extPar.GPIB1, '++addr 2');%sets address to talk to the SRS
    pause(0.2)
    fprintf(extPar.GPIB1, '*CLS');%clears buffer
```

```
88      pause(0.2)
89      fprintf(extPar.GPIB1, '*RST');%resets instrument
90      pause(0.5)
91      fprintf(extPar.GPIB1, '*IDN?');%Queries instrument ID
92      pause(0.5)
93      txt = fgets(extPar.GPIB1);
94      disp(['Setting up ' txt])
95      fprintf(extPar.GPIB1, ['SENS ' num2str(sens)]);%sets sensitivity to user
            input
96      pause(0.2)
97      fprintf(extPar.GPIB1, ['OFLT ' num2str(tConst)]);%sets time constant to
           user input
98      pause(0.2)
99      fprintf(extPar.GPIB1, 'OFSL 2');%sets filter 18dB/oct
100     pause(0.2)
101     fprintf(extPar.GPIB1, 'ISRC 0');%sets input to A
102     pause(0.2)
103     fprintf(extPar.GPIB1, 'IGND 1');%sets ground to internal reference
104     pause(0.2)
105     fprintf(extPar.GPIB1, 'ICPL 1');%sets AC coupling
106     pause(0.2)
107     fprintf(extPar.GPIB1, 'FMOD 1');%sets frequency reference to internal
108     pause(0.2)
109     fprintf(extPar.GPIB1, 'RMOD 1');%sets signal reserve to normal
110     pause(0.2)
111     fprintf(extPar.GPIB1, ['FREQ ' num2str(center+offset)]);%sets frequency
```

```
        reference ~100 Hz away from resonance
    pause(0.2)
    fprintf(extPar.GPIB1, 'PHAS -40');%sets lock-in to force a certain phase
    % relationship between X and Y, if desired.
end
%% %%%%%%%%%%setup the Agilent 33522A AWG%%%%%%%%%%%%%%%%%%%%%%%%%%%%%%%%
if configAWG
    fprintf(extPar.GPIB1, '++addr 3');%sets address to talk to the Agilent
    pause(0.2)
    fprintf(extPar.GPIB1, '*CLS');%clears cuurent buffer
    pause(0.2)
    fprintf(extPar.GPIB1, '*RST');%resets instrument
    pause(0.2)
    fprintf(extPar.GPIB1, '*IDN?');
    pause(0.2)
    txt = fgets(extPar.GPIB1);
    pause(0.2)
    disp(['Setting up ' txt])
    %%%%sets CH2 to provide the AOM modulation signal%%%%%%%
    fprintf(extPar.GPIB1, 'SYSTEM:BEEP:STATE OFF');%deactivates beep
    pause(0.2)
    fprintf(extPar.GPIB1, 'SOURCE2:FUNC SQUARE');
    pause(0.2)
    fprintf(extPar.GPIB1, ['SOURCE2:FREQ ' num2str(extPar.pump.center)]);
    pause(0.2)
    fprintf(extPar.GPIB1, 'SOURCE2:VOLT:UNIT VPP');
```

```
137     pause(0.2)
138     fprintf(extPar.GPIB1, ['SOURCE2:VOLT ' num2str(extPar.pump.AOMamplitude)
            ]);
139     pause(0.2)
140     fprintf(extPar.GPIB1, ['SOURCE2:VOLT:OFFSET ' num2str(extPar.pump.
            AOMamplitude./2)]);
141     pause(0.2)
142     fprintf(extPar.GPIB1, ['SOURCE2:FUNC:SQUARE:DCYCLE ' num2str(extPar.pump
            .dCycle)]);%DCYCLE -> Duty CYCLE
143     pause(0.2)
144     fprintf(extPar.GPIB1, 'SOURCE2:FUNC:PHASE 0');
145     pause(0.2)
146     fprintf(extPar.GPIB1, 'OUTPUT2:LOAD 50');%sets load to 50 ohms
147     pause(0.2)
148     fprintf(extPar.GPIB1, 'OUTPUT2 ON');%turns on CH2
149     pause(0.2)
150     fprintf(extPar.GPIB1, 'OUTPUT:SYNC:SOURCE CH2');%changes sync source to
            ch2 for lock-in
151     pause(0.2)
152     fprintf(extPar.GPIB1, 'OUTPUT:SYNC ON');%turns sync on
153     pause(0.2)
154     fprintf(extPar.GPIB1, 'SOURCE2:BURST:STATE ON');%turns on burst mode
155     pause(0.2)
156     fprintf(extPar.GPIB1, 'SOURCE2:BURST:MODE TRIG');%sets burst to start on
             trigger
157     pause(0.2)
```

```
158     fprintf(extPar.GPIB1, 'TRIG2:SOUR TIM');%sets trigger to bus, a *TRIG
            command will trigger a burst
159     pause(0.2)
160     fprintf(extPar.GPIB1, ['TRIG2:TIM ' num2str(extPar.pump.triggertime)]);
161     pause(0.2)
162     fprintf(extPar.GPIB1, ['SOURCE2:BURST:NCYCLES ' num2str(extPar.pump.
            nCycles)]);%sets burst to last a certain number of cycles
163     pause(0.2)
164 end
165 %% %%%%%%%%%%%%%%%%%%%%%%setup the Keithley 2002 Multimeter%%%%%%%%%%%%%%%%
166 if configDMM
167     fprintf(extPar.GPIB1, '++addr 1');%sets address to talk to the Keithley
168     pause(0.2)
169     fprintf(extPar.GPIB1, '*CLS');%clears current buffer
170     pause(0.2)
171     fprintf(extPar.GPIB1, '*RST');%resets instrument
172     pause(0.2)
173     fprintf(extPar.GPIB1, '*IDN?');%resets instrument
174     pause(0.2)
175     txt = fgets(extPar.GPIB1);
176     disp(['Setting up ' txt])
177     pause(0.2)
178     fprintf(extPar.GPIB1, 'SENSE1:VOLT:DC:RANGE:UPPER 2');%sets measurment
            range to
179     %200 mV.
180     pause(0.2)
```

```
181     fprintf(extPar.GPIB1, 'SENSE1:VOLT:DC:NPLC 10');
182     %sets the number of power line cycles
183     pause(0.2)
184     fprintf(extPar.GPIB1, 'SENSE1:VOLT:DC:DIGITS 8.5');
185 end
186 %% %%%%%%%%%%%%%%%%%%%%%setup the Agilent power supply%%%%%%%%%%%%%%%%%%%%%
187 if configPS
188     fprintf(extPar.GPIB1, '++addr 4');%sets address to talk to the Power
            supply
189     pause(0.2)
190     fprintf(extPar.GPIB1, '*IDN?');
191     pause(0.2)
192     txt = fgets(extPar.GPIB1);
193     disp(['Setting up ' txt])
194     pause(0.2)
195     fprintf(extPar.GPIB1, ':SOUR1:FUNC:MODE CURR');%sets CH1 to output
            constant current
196     pause(0.2)
197     fprintf(extPar.GPIB1,':SENS1:VOLT:DC:PROT:POS 3');
198     pause(0.2)
199     fprintf(extPar.GPIB1, [':SOUR1:CURR ' num2str(extPar.coilCurr) 'E-3']);%
            sets current to provide ~1 uT
200     pause(0.5)
201     fprintf(extPar.GPIB1, ':OUTP1 ON');%turns on CH1
202     pause(0.2)
203     fprintf(extPar.GPIB1,'SOUR2:FUNC:MODE CURR');%sets CH2 to output
```

```
        constant current
    pause(0.2)
    fprintf(extPar.GPIB1,'SOUR2:CURR 0');%sets output to 0 amps
    pause(0.2)
    fprintf(extPar.GPIB1,':OUTP2 ON');%turns on CH2
    pause(0.2)
    fprintf(extPar.GPIB1,':SENS2:VOLT:DC:PROT:POS 6');%sets voltage
        protection to 6V.
end
%% %%%%%%%%%%%%%%%%%%%%%%%%%%%%%Setup the Scope%%%%%%%%%%%%%%%%%%%%%%%%%%%%
pause(0.1)
fprintf(extPar.scopeVisa, 'HORizontal:RECordlength 10000000');
pause(0.1)
set(extPar.scope.Acquisition(1), 'Timebase', 10);
set(extPar.scope.Acquisition(1), 'Delay', 50);
set(extPar.scope.Acquisition(1), 'Mode', 'hires');
%set(extPar.scope.Channel(2), 'BandwidthLimit', 'twenty');
set(extPar.scope.Acquisition, 'Control', 'single');
set(extPar.scope.Acquisition(1), 'State', 'stop');
set(extPar.scope.Channel(1), 'Coupling', 'ac');
set(extPar.scope.Channel(2), 'Coupling', 'ac');
set(extPar.scope.Channel(4), 'Coupling', 'dc');
set(extPar.scope.Trigger(1), 'Holdoff', 0.005);
set(extPar.scope.Trigger(1), 'TriggerType', 'edge');
set(extPar.scope.Trigger(1), 'Slope', 'rising');
set(extPar.scope.Trigger(1), 'Mode', 'normal');
```

```
228 set(extPar.scope.Trigger(1), 'Source', 'channel3');
229 set(extPar.scope.Trigger(1), 'Coupling', 'dc');
230 set(extPar.scope.Trigger(1), 'Level', 2);
231 extPar.numPoints = get(extPar.scope.Waveform(1), 'MaxNumberPoint');
232 extPar.timebase = get(extPar.scope.Acquisition(1), 'Timebase');
233 extPar.endPoint = get(extPar.scope.Waveform(1), 'EndingPoint');
234 extPar.firstPoint = get(extPar.scope.Waveform(1), 'FirstPoint');
235 extPar.fSample = 100000;
236 extPar.tSample = 1./100000;
237 %% %%%%%%%%%%%%%%%%%%%%%%%%%Finalization%%%%%%%%%%%%%%%%%%%%%%%%%%%%%%%%
238 if strcmp('y',degauss)
239     disp('Degaussing sequence will start in 10 seconds...')
240     fprintf(extPar.GPIB1, '++addr 3');%sets address to talk to the Agilent
241     pause(0.2)
242     fprintf(extPar.GPIB1, 'MMEM:LOAD:DATA1 "INT:\DG2.ARB"');%loads file DG2.
          arb from the
243     %internal directory into volatile memory, "arb memory catalog".  Note
244     %that DG2.arb is not located in INT:\BUILTIN\, it is in the top level
245     %directory.  The Agilent 32500 series programmers guide doesn't seem to
246     %exist anywhere on the internet, but the "E725D" model programmers
247     %guide seemed to be similar enough to help, as it is also from Agilent.
248     pause(3)
249     fprintf(extPar.GPIB1, 'FUNC:ARB "INT:\DG2.ARB"');%assigns the "arb"
          button to the
250     %file "INT:\DG2.ARB", which is now in memory.  If this isn't working,
251     %check the arb memory catalog by using the front panel to navigate to
```

```
252     %"arbs" and "arbs in memory".  The built-in exponential should be there
253     %as well as DG.arb.  This should show the full file path and extension
254     %to use.`
255     pause(0.5)
256     fprintf(extPar.GPIB1, 'FUNC:ARB:SRATE 4000');%SRATE -> Sample RATE
257     pause(0.2)
258     fprintf(extPar.GPIB1, ':SOURce1:FUNC SIN');%SOURCE1 sets up CH1 with a
            sin wave
259     %as the carrier wave
260     pause(0.2)
261     fprintf(extPar.GPIB1, 'SOURCE1:VOLT:UNIT VPP');
262     pause(0.2)
263     fprintf(extPar.GPIB1, 'SOURCE1:VOLT 7');
264     pause(0.2)
265     fprintf(extPar.GPIB1, 'SOURCE1:FREQ 10');
266     pause(0.2)
267     fprintf(extPar.GPIB1, 'SOURCE1:AM:DSSC ON');%turns on modulation in non-
            DSSC mode
268     pause(0.2)
269     fprintf(extPar.GPIB1, 'SOURCE1:AM:SOURCE INT');
270     pause(0.2)
271     fprintf(extPar.GPIB1, 'SOURCE1:AM:INT:FUNC ARB');%assigns whatever
            function "arb"
272     %is to be the modulating signal
273     pause(4.7)
274     fprintf(extPar.GPIB1, 'SOURCE1:AM:STATE ON');%activates modulation
```

```
275     pause(0.2)
276     fprintf(extPar.GPIB1, 'OUTPUT1 ON');%activates degaussing signal
277     disp('Please degauss the shields.  Waiting for button press.')
278     pause;
279     fprintf(extPar.GPIB1, 'OUTPUT1 OFF');%deactivates degaussing signal
280 end
281 fprintf(extPar.GPIB1, '++addr 1');%sets GPIB controller to talk to the
       Keithley
282 %before finishing setup.  This should make taking the coil voltage faster.
283 test = getVoltage(extPar.GPIB1);
284 disp(['test voltage: ' num2str(test)]);
285 fclose(extPar.GPIB1);
286 end
```

```
1  function data = getData(extPar)
2  fopen(extPar.GPIB1);%open serial port
3  V = zeros(1,5*extPar.numFIDs/extPar.pump.FIDrate);
4  time = zeros(1,5.*extPar.numFIDs/extPar.pump.FIDrate);
5  set(extPar.scope.Acquisition(1), 'State', 'run');
6  tStart = tic;
7  for i = 1:(5*extPar.numFIDs)/extPar.pump.FIDrate
8      while abs(mod(toc(tStart),0.2))>0.002
9          %wait until the time is an even multiple of the sample rate
10     end
11     V(i) = getVoltage(extPar.GPIB1);
12     time(i) = toc(tStart);
```

```
end
pause(5);
waveObj = get(extPar.scope, 'Waveform');
pause(0.1);
[y1,x1,yu1,xu1] = invoke(waveObj, 'readwaveform', 'channel1');
pause(0.1);
[y2,x2,yu2,xu2] = invoke(waveObj, 'readwaveform', 'channel2');
pause(0.1);
[y3,x3,yu3,xu3] = invoke(waveObj, 'readwaveform', 'channel3');
pause(0.1);
[y4,x4,yu4,yu4] = invoke(waveObj, 'readwaveform', 'channel4');
data.scopeData = [y1;y2;y3;y4;x2];%(CH1,CH2,CH4,time)
data.bMeas = [V;time];
fclose(extPar.GPIB1);
end
```

```
function voltage = getVoltage(GPIB1)
%%%%%%%%%%%%%%%%%%%%%%%%%%%%%%%%%%%%%%%%%%%%%%%%%%%%%%%%%%%%%%%%%%%%%%%%%%%%
%getVoltage sets the GPIB controller to talk to the Keithley at address 1,
%then gets the voltage and stores it as the output of the function.  It
%takes in the serial object as a parameter so it can check if the port is
%open.  This function (and all of my functions so far) assumes '++auto 1' is
%activated.  Runtime is ~0.2 seconds.
if strcmp('closed',GPIB1.Status)
    fopen(GPIB1)
end
```

```
fprintf(GPIB1, '++addr 1');
fprintf(GPIB1, ':MEAS?');
voltage = str2num(fgets(GPIB1));
end
```

```
function [data,fitPar] = fitData(extPar,data)
%% %%%%%%%%%%%%%%%%%%%%%%%%find and separate FIDs%%%%%%%%%%%%%%%%%%%%%%%%
data.trigger = data.scopeData(3,:);
data.scopeTime = data.scopeData(5,:);
data.rawFIDs = data.scopeData(1,:);
data.coilTime = data.bMeas(2,:);
data.coilVolt = data.bMeas(1,:);
indices = round(findFIDs(extPar,data.trigger));
indices(1,:) = indices(1,:) + 19;
for i = 1:extPar.numFIDs
    data.FIDs(i).x = data.rawFIDs(indices(1,i):indices(2,i));
    data.FIDs(i).x = data.FIDs(i).x - mean(data.FIDs(i).x);
    data.FIDs(i).t = data.scopeTime(indices(1,i):indices(2,i));
    data.FIDs(i).timestamp = mean(data.FIDs(i).t);
    data.FIDs(i).t = data.FIDs(i).t - min(data.FIDs(i).t);
end
%% %%%%%%%%%%%%%%%%%%%%%%%%time domain fit%%%%%%%%%%%%%%%%%%%%%%%%%%%%%%%%
opts = optimset(...
    'TolFun',1e-21,...
    'MaxFunEvals',20000,...
    'Display','off',...
```

```
    'TolX',1e-21);
ampGuess = abs(max(data.FIDs(1).x) - min(data.FIDs(1).x))./2;
tConstGuess = 60;
wGuess = abs(2.*pi.*extPar.pump.center);
phaseGuess = pi./4;
offsetGuess = mean(data.FIDs(1).x);
par0 = [ampGuess,tConstGuess,wGuess,phaseGuess,offsetGuess];
FID = @(par,x)...
    par(1).*exp(-par(2).*(x)).*sin(par(3).*(x)+par(4))+par(5);
for i = 1:extPar.numFIDs
    try
        [par,resnorm,residual,~,~,~,jacobian] = ...
            lsqcurvefit(FID,par0,data.FIDs(i).t,data.FIDs(i).x,[0,0,0,-4.*pi
                ,-1],[],opts);
        s2=resnorm/(length(residual) - length(par));
        [~,R]=qr(jacobian,0);
        Rinv=inv(R);
        sigmaest=(Rinv*Rinv')*s2;
        pErr=sqrt(diag(sigmaest));
        par = full([par;pErr']);
        if full(pErr(3,1))>1
            fitPar.time(i).fitPar = [[NaN NaN NaN NaN NaN;NaN NaN NaN NaN
                NaN],[data.FIDs(i).timestamp;0]];
        else
            fitPar.time(i).fitPar = [par,[data.FIDs(i).timestamp;0]];
        end
```

```
    catch
        disp(['Fit ' num2str(i) ' failed, filling with NaN']);
        fitPar.time(i).fitPar = [[NaN NaN NaN NaN NaN;NaN NaN NaN NaN NaN],[
            data.FIDs(i).timestamp;0]];
    end
    if mod(i,extPar.numFIDs./100)==0
        disp(['fitting time domain signal: ' num2str(i./(extPar.numFIDs
            ./100)) '% done']);
    end
end
end
```

```
function indices = findFIDs(extPar,trigger)
%% %%%%%%%%%%%%%%%%%%Wolfgang Klassen, August 2019%%%%%%%%%%%%%%%%%%%%%%%%
%
%This function takes in the trigger signal from the AWG as recorded by the
%scope.  This is a square wave signal that is only non-zero when pumping
%is active.  By looking for the transitions between zero and non-zero
%portions of this signal, we can identify the bounds of the FIDs.  Output
%is a 2-by-numFIDs array of index values.  The first row is the begginning
%of all the FIDs, the second is the end of those FIDs.
%
%%%%%%%%%%%%%%%%%%%%%%%%%%%%%%%%%%%%%%%%%%%%%%%%%%%%%%%%%%%%%%%%%%%%%%%%%%%
%find low-to-high transitions
[~,P] = islocalmax(trigger(2:end) - trigger(1:end-1));
ihi = find(P>1);
```

```
ihi((ihi(2:end)-ihi(1:end-1))<5) = [];%check for double peaks, in case the
%low-to-high transition was sampled twice by the scope.
%find high-to-low transitions
[~,P] = islocalmax(trigger(1:end-1) - trigger(2:end));
ilo = find(P>1);
ilo((ilo(2:end)-ilo(1:end-1))<5) = [];
%clean up beginning, making sure that the lowest index value is contained
%in ilo
if ihi(1)<ilo(1)
    ihi = ihi(2:end);
    %if the lowest index value isn't in ilo, delete the first point in ihi.
    %This would correspond to the second index of the FID happening before
    %the trigger, which shouldn't be in our dataset.
end
%clean up the end, making sure that the highest index value is contained in
%ihi
if ihi(end)<ilo(end)
    ihi(end+1) = extPar.endPoint;
    %if the highest index isn't contained in ihi, add the last index of the
    %dataset to the end of ihi, since it should have the second index of
    %the last FID in it.
end
indices = [ilo;ihi];
end
```

Appendix D

Publications

D.1 Authors contribution to published work

The following paper has been published in Nuclear Instruments and Methods in Physics Research A. The author was responsible for checking calculations in sections 2 and 3, and carrying out the calculations in sections 4 and 5. The author was selected for lead authorship. In particular section 5 discusses potential experimental configurations for an nEDM experiment that follow from the calculations.

Wigner-Eckart Theorem and the False EDM of ^{199}Hg

W. Klassen[a], J.W. Martin[b,a], G. Pignol[c]

[a] *Physics and Astronomy, University of Manitoba, Winnipeg, MB, Canada*
[b] *Department of Physics, The University of Winnipeg, Winnipeg, MB, Canada*
[c] *Université Grenoble Alpes, CNRS, Grenoble INP, LPSC-IN2P3, Grenoble, France*

Abstract

In neutron electric dipole moment (EDM) experiments, ^{199}Hg is used as a comagnetometer. The comagnetometer suffers from a false EDM arising in leading order from a gradient $\partial B_z/\partial z$ in the magnetic field. Our work concerns higher-order multipole corrections to the false EDM of ^{199}Hg. We show that for spherical traps, all higher-order multipoles are identically zero. We further show that for the usual cylindrical traps used in EDM experiments, selection of quasi-spherical dimensions for the trap can reduce the higher-order contributions. The results are another indication that trap geometry is an important consideration for experiments desiring to control this systematic effect.

Keywords: false electric dipole moment, trapped particles, neutron electric dipole moment

1. False electric dipole moments for particles in traps

In the most precise neutron electric dipole moment (EDM) experiments, ultracold neutrons are stored in a bottle in either parallel or antiparallel electric E and magnetic B fields. Their spin precession frequency $\omega_\pm$ is measured

$$\omega_\pm = (2\mu_n B \pm 2d_n E)/\hbar \tag{1}$$

for each of the parallel (+) and antiparallel (−) configurations, leading to a determination of the neutron electric dipole moment d_n. Here μ_n is the neutron magnetic moment.

A crucial aspect of the experiment is that the magnetic field be continuously monitored so that any drifts can be corrected. To monitor the field, a second "comagnetometer" atomic species is stored in the cell and its spin

precession frequency is measured optically. Normally ^{199}Hg is used for this purpose [1, 2, 3], in part because its true EDM has been constrained to be small [4, 5].

Ideally, the magnetic field B should be uniform so that long free-precession times can be achieved for both the neutrons and Hg atoms. In the previous most precise nEDM experiment [6, 7] it was found that a vertical gradient $\partial B_z/\partial z$ in the magnetic field induced false EDM's for the neutrons and Hg atoms. The frequency shift can be considered as a Ramsey-Bloch-Siegert shift for particles traveling in orbits within the trap [8, 9]. The ultracold neutrons traverse the measurement volume slowly enough that their accrued phase can be thought of as a geometric phase which accrues adiabatically [8].

The false EDM's can also be calculated by correlation function techniques [10, 11]. This led to the realization that false EDM for the Hg atoms could be written in the form

$$d_{f,\mathrm{Hg}} = -\frac{\hbar\gamma^2}{2c^2}\langle xB_x + yB_y\rangle \tag{2}$$

using integration by parts [12]. Here, $\gamma = 2\mu/\hbar$ is the gyromagnetic ratio of Hg with μ being its magnetic moment, and the average is over the storage volume. This form is valid to high precision in the low-frequency (field) limit, even reproducing higher-order effects first studied using Monte Carlo techniques in Ref. [9].

The false EDM of Hg is also well-understood experimentally, having been characterized using surrounding Cs magnetometers [13] and to higher orders [14].

The work presented here concerns higher-order corrections beyond the first-order vertical gradient $\partial B_z/\partial z$. We show that for spherical traps, all higher-order terms contributing to Eq. (2) are identically zero. We further show that for the usual cylindrical traps used in EDM experiments, selection of quasi-spherical dimensions for the trap can reduce the higher-order contributions to false EDM of the Hg atoms.

2. Harmonic Decomposition of the Magnetic Field

Within the measurement region of EDM experiments, nonmagnetic components are used so that the field can be measured and controlled precisely. Since bound and free currents are absent from this region, the magnetic field can be written as

$$\vec{B} = -\nabla\Phi_M \tag{3}$$

where Φ_M is the magnetic scalar potential. Since $\nabla \cdot \vec{B} = 0$, Φ_M obeys Laplace's equation:

$$\nabla^2 \Phi_M = 0. \tag{4}$$

The general solution for a boundary-value problem can be written in spherical coordinates (r, θ, ϕ) in terms of spherical harmonics $Y_{\ell m}(\theta, \phi)$ as [15]

$$\Phi_M(r, \theta, \phi) = \sum_{\ell=0}^{\infty} \sum_{m=-\ell}^{\ell} \left[A_{\ell m} r^{\ell} + B_{\ell m} r^{-(\ell+1)} \right] Y_{\ell m}(\theta, \phi) \tag{5}$$

where $A_{\ell m}$ and $B_{\ell m}$ are sets of constants determined by the boundary conditions. If we define $r = 0$ to be the center of the trap, the requirement that $\vec{B}$ remain finite enforces $B_{\ell m} = 0$. The spherical harmonics can be written as

$$Y_{\ell m}(\theta, \phi) = \sqrt{\frac{2\ell + 1}{4\pi} \frac{(\ell - m)!}{(\ell + m)!}} P_{\ell}^{m}(\cos\theta) e^{im\phi}, \tag{6}$$

where P_{ℓ}^{m} are the associated Legendre polynomials.

The average appearing in Eq. (2) can be recast in terms of the scalar potential as

$$\langle x B_x + y B_y \rangle = - \left\langle \left(x \frac{\partial}{\partial x} + y \frac{\partial}{\partial y} \right) \Phi_M \right\rangle \tag{7}$$

which in terms of the spherical harmonics becomes

$$\langle x B_x + y B_y \rangle = - \sum_{\ell=0}^{\infty} \sum_{m=-\ell}^{\ell} A_{\ell m} \left\langle \left(x \frac{\partial}{\partial x} + y \frac{\partial}{\partial y} \right) r^{\ell} Y_{\ell m} \right\rangle \tag{8}$$

where again the average is conducted over the measurement cell.

3. Application of the Wigner-Eckart Theorem

We can apply the Wigner-Eckart Theorem to this system by making an analogy to matrix elements in quantum mechanics. The differential operator in Eq. (8) $\left(x \frac{\partial}{\partial x} + y \frac{\partial}{\partial y} \right)$ can be analogized to the operator $(x p_x + y p_y)$ in quantum mechanics.

For a particle in a spherically symmetric potential, the stationary states may be written as eigenstates of the angular momentum operators

$$L^2 |n\ell m\rangle = \hbar^2 \ell(\ell + 1) |n\ell m\rangle \tag{9}$$

$$L_z |n\ell m\rangle = \hbar m |n\ell m\rangle \tag{10}$$

where $|n\ell m\rangle$ represents the stationary state and ℓ and m are quantum numbers. The quantum number n would count energy levels. In the position representation, the states factorize in spherical coordinates as

$$\langle \vec{r}|n\ell m\rangle = R_{n\ell}(r)Y_{\ell m}(\theta,\phi) \tag{11}$$

and thus the states are related to the spherical harmonics.

Eq. (8) therefore has a number of elements which bear a strong similarity with calculations in quantum mechanics. The average in Eq. (8) is over the EDM measurement cell volume. In order to use the Wigner-Eckart theorem, we want to make an analogy to quantum mechanical matrix elements. In order for this analogy be valid, the cell would have to be a spherical cell. In this circumstance, the term under the average is proportional to a quantum mechanical matrix element as

$$\left\langle \left(x\frac{\partial}{\partial x} + y\frac{\partial}{\partial y} \right) r^{\ell} Y_{\ell m} \right\rangle \sim \langle n'00|(xp_x + yp_y)|n\ell m\rangle \tag{12}$$

where we have inserted a spherically symmetric state with $\ell' = m' = 0$. Being constructed from products of vector operators, we will show that the operator $(xp_x + yp_y)$ can be written as an admixture of spherical tensors of rank 0 and 2.

The Wigner-Eckart theorem relates matrix elements of spherical tensors involving these states to Clebsch-Gordan coefficients [16]. Applied to two states $|n'\ell'm'\rangle$ and $|n\ell m\rangle$, it would read

$$\langle n'\ell'm'|T^{(k)}_q|n\ell m\rangle = \langle \ell k; mq|\ell k; \ell' m'\rangle \frac{\langle n'\ell'||T^{(k)}||n\ell\rangle}{\sqrt{2j+1}} \tag{13}$$

where $T^{(k)}_q$ is a spherical tensor of rank k with magnetic quantum number q. The double-bar matrix element is a reduced matrix element that does not depend on m, m', or q.

The Clebsch-Gordan coefficient $\langle \ell k; mq|\ell k; \ell' m'\rangle$ can be thought of in the following more familiar way. Imagine two angular momentum operators $\vec{L}$ and $\vec{K}$ with simultaneous eigenstates $|\ell k; mq\rangle$ s.t.

$$L^2|\ell k; mq\rangle = \hbar^2 \ell(\ell+1)|\ell k; mq\rangle \tag{14}$$

$$L_z|\ell k; mq\rangle = \hbar m|\ell k; mq\rangle \tag{15}$$

$$K^2|\ell k; mq\rangle = \hbar^2 k(k+1)|\ell k; mq\rangle \tag{16}$$

$$K_z|\ell k; mq\rangle = \hbar q|\ell k; mq\rangle. \tag{17}$$

If we now define a new operator $\vec{L}' = \vec{L} + \vec{K}$, the Clebsch-Gordan coefficients represent the coefficients transforming to the new basis $|\ell k; \ell' m'\rangle$ where

$$L^2|\ell k; mq\rangle = \hbar^2 \ell(\ell+1)|\ell k; \ell' m'\rangle \tag{18}$$
$$K^2|\ell k; mq\rangle = \hbar^2 k(k+1)|\ell k; \ell' m'\rangle \tag{19}$$
$$L'^2|\ell k; mq\rangle = \hbar^2 \ell'(\ell'+1)|\ell k; \ell' m'\rangle \tag{20}$$
$$L'_z|\ell k; mq\rangle = \hbar m'|\ell k; \ell' m'\rangle. \tag{21}$$

In this way, the Clebsch-Gordan coefficient is related to the addition of angular momentum of the state $|n\ell m\rangle$ to that of the spherical tensor $T_q^{(k)}$ and reaching the state $|n'\ell' m'\rangle$.

The Clebsch-Gordan coefficient is only non-zero if

$$m + q = m' \tag{22}$$

and

$$|\ell - k| \leq \ell' \leq \ell + k \tag{23}$$

As mentioned earlier the operator $(xp_x + yp_y)$ can be written as an admixture of spherical tensors of rank 0 and 2. The following two spherical tensors may be constructed from the Cartesian components of the vector operators $\vec{r}$ and $\vec{p}$:

$$T_0^{(0)} = -\frac{\vec{r}\cdot\vec{p}}{3} = \frac{-xp_x - yp_y - zp_z}{3} \tag{24}$$

and

$$T_0^{(2)} = \frac{3zp_z - \vec{r}\cdot\vec{p}}{\sqrt{6}} = \frac{-xp_x - yp_y + 2zp_z}{\sqrt{6}}. \tag{25}$$

The operator of interest can then be written as

$$xp_x + yp_y = -2T_0^{(0)} - \sqrt{\frac{2}{3}}T_0^{(2)} \tag{26}$$

which are spherical tensors of rank 0 and 2 with magnetic quantum number $q = 0$.

Finally we note that because these operators are even under the parity transformation, they may only link states of the same parity.

We can now apply Eqs. (22) and (23) to Eq. (8) to find that only terms in the sums with $m = 0$ and $\ell = 0, 1, 2$ will contribute. Since the operator in Eq. (8) is a differential operator, the term with $\ell = 0$ also cannot contribute.

The term with $\ell = 1$ is ruled out by the parity selection rule. We are then left with only one non-zero term arising from the harmonic decomposition of the field:

$$\langle xB_x + yB_y \rangle = -A_{20} \left\langle \left(x\frac{\partial}{\partial x} + y\frac{\partial}{\partial y} \right) r^2 Y_{20} \right\rangle \tag{27}$$

where the average can be readily carried out since $r^2 Y_{20}$ is a polynomial of degree 2 in Cartesian coordinates.

The suppression of the higher-order terms can be derived in a number of different ways, for example, by the commutation relations of the operators, by integration by parts, and/or by using the known properties of the spherical harmonics/Legendre polynomials. We used this to check the result in a number of ways. This included (a) explicit integration of the $m = 0$ terms for particular higher ℓ, demonstrating they were all zero, and (b) integration by parts (shifting the derivatives to the left) and then using the orthogonality of the Legendre polynomials to demonstrate that only $\ell = 2$ is permitted.

4. Cylindrical Trap and Suppression of Higher Orders

A requirement of the calculation of the preceding section is that the EDM cell be spherical, which is not an attractive option for EDM experiments. A more typical geometry is a cylindrically symmetric geometry. In this case, it can still readily be demonstrated that only $m = 0$ terms contribute in the second sum in Eq. (8). Switching to cylindrical (ρ, ϕ, z) coordinates, the differential operator becomes $x\frac{\partial}{\partial x} + y\frac{\partial}{\partial y} = \rho\frac{\partial}{\partial \rho}$ and since $Y_{\ell m} \sim e^{im\phi}$ these terms would average to zero unless $m = 0$. Furthermore, terms with $\ell =$ odd are odd in z. Thus if the cylindrical cell is centered on $z = 0$, these terms will also average to zero. We are then left with

$$\langle xB_x + yB_y \rangle = -\sum_{\ell=2,4,6,\ldots}^{\infty} A_{\ell 0} \left\langle \left(\rho\frac{\partial}{\partial \rho} \right) r^\ell Y_{\ell 0} \right\rangle \tag{28}$$

The purpose of this section is to demonstrate that $\ell = 2$ dominates, that for a certain choice of cell dimensions the $\ell = 4$ term can be zeroed, and that for this selection the $\ell = 6$ term can be reduced compared to the typical cell geometry used for the ILL nEDM experiment.

In order to more easily compare to Ref. [12], we introduce a more convenient normalization based on the Legendre polynomials $P_\ell(\cos\theta)$ as

$$\langle xB_x + yB_y \rangle = + \sum_{\ell=2,4,6\ldots}^{\infty} \frac{g_{(\ell-1)0}}{\ell} \left\langle \left(\rho \frac{\partial}{\partial \rho} \right) r^\ell P_\ell(\cos\theta) \right\rangle , \tag{29}$$

where the $g_{(\ell-1)0}$ are related by constants (and a sign change) to the $A_{\ell 0}$ in Eq. (28). This normalization is preferred because it ensures that the $m = 0$ components of $B_z = -\frac{\partial \Phi_M}{\partial z}$ are polynomials which contain $g_{\ell 0} z^\ell$ with $\ell =$ odd. This guarantees, for example, that the leading-order term in the vertical gradient is $\frac{\partial B_z}{\partial z} = g_{10}$, allowing us to easily identify g_{10} itself as the first-order uniform gradient term of Ref. [12].

In general $\frac{1}{\ell} r^\ell P_\ell(\cos\theta)$, when expressed in cylindrical coordinates, is a polynomial in ρ and z. For the terms of interest, the polynomials are

$$\frac{1}{2} r^2 P_2(\cos\theta) = \frac{1}{4} \left(2z^2 - \rho^2 \right) \tag{30}$$

$$\frac{1}{4} r^4 P_4(\cos\theta) = \frac{1}{32} \left(8z^4 - 24 z^2 \rho^2 + 3\rho^4 \right) , \text{ and} \tag{31}$$

$$\frac{1}{6} r^6 P_6(\cos\theta) = \frac{1}{96} \left(16 z^6 - 120 z^4 \rho^2 + 90 z^2 \rho^4 - 5\rho^6 \right) . \tag{32}$$

We define the origin of coordinates to lie at the center of a measurement cell with height H and radius R. Carrying out the average over the cell, the first three non-zero terms of Eq. (29) become

$$\langle xB_x + yB_y \rangle = -\frac{R^2}{4} \left[g_{10} + g_{30} \left(\frac{H^2}{4} - \frac{R^2}{2} \right) + g_{50} \left(\frac{H^4}{16} - \frac{5R^2 H^2}{12} + \frac{5R^4}{16} \right) \right] . \tag{33}$$

The expression for $d_{f,\mathrm{Hg}}$ then becomes

$$d_{f,\mathrm{Hg}} = \frac{\hbar \gamma^2 R^2}{8c^2} \left[g_{10} + g_{30} \left(\frac{H^2}{4} - \frac{R^2}{2} \right) + g_{50} \left(\frac{H^4}{16} - \frac{5R^2 H^2}{12} + \frac{5R^4}{16} \right) \right] . \tag{34}$$

The g_{10} term is in agreement with Ref. [12], and the other two terms have also been derived previously [17]. We now analyze these next two terms.

An immediate observation is that the g_{30} term can be set to zero if the measurement volume is quasi-spherical *i.e.* for

$$H = \sqrt{2}R \tag{35}$$

If this selection is made, then the factor in the g_{50} term becomes

$$\frac{H^4}{16} - \frac{5R^2H^2}{12} + \frac{5R^4}{16} = -\frac{13}{48}R^4 \tag{36}$$

The question now becomes whether this is a reasonable geometry for an nEDM experiment.

5. Discussion and Caveats

5.1. ILL/PSI nEDM experiment geometry

For the ILL/PSI nEDM experiment, the cell dimensions are $R = 23.5$ cm and $H = 12$ cm, and so Eq. (35) is clearly not obeyed. Using the ILL/PSI geometry, the g_{30} term is

$$\frac{H^2}{4} - \frac{R^2}{2} = -240 \text{ cm}^2 \tag{37}$$

and the g_{50} term is

$$\frac{H^4}{16} - \frac{5R^2H^2}{12} + \frac{5R^4}{16} = 6.35 \times 10^4 \text{ cm}^4 \tag{38}$$

The false EDM then becomes

$$d_{f,\text{Hg}} = 1.15 \times 10^{-27} \left(g_{10} - g_{30} \cdot 240 + g_{50} \cdot 6.35 \times 10^4\right) \text{e} \cdot \text{cm} \tag{39}$$

where the $g_{\ell 0}$ are expressed in units of pT/cm$^\ell$. The g_{30} term was analyzed and measured experimentally in Ref. [14] and found to be in agreement with expectation.

5.2. Quasi-spherical geometry

In order to compare this result for a realistic experimental geometry to our suggestion of a quasi-spherical cell, we considered several possibilities. One possibility was to keep the radius of the cell the same as for the ILL experiment. This would mean that the size of the pre-factor in Eq. (39) would

be equal. In this case, the height of the cell would necessarily be increased to $H = \sqrt{2}{\cdot}23.5$ cm ≈ 33 cm. The negative aspect of this suggestion is that a high-voltage nearly a factor of three larger would need to be sustained across the electrodes in order to keep the electric field in the experiment the same. Since the electric field is strongly related to the statistical precision of the experiment, it is not clear that this is a realistic compromise.

Another possibility was to keep the height of the cell the same, which would alleviate any high-voltage issues. In this case the cell radius would need to shrink to $R = 12$ cm$/\sqrt{2} \approx 8.5$ cm. The negative aspect here is that the volume of the experiment would shrink by a factor of almost eight. In general, the statistical precision of neutron EDM experiments is driven by the neutron density achievable in the cell, and this choice would mean that the number of neutrons loaded into the cell would be reduced by the same factor.

We therefore decided to suggest keeping approximately the same EDM cell volume, setting $R = 17$ cm and $H = \sqrt{2}{\cdot}17$ cm ≈ 24 cm. For this choice, the $\ell = 4$ term is zero and the expression for the false EDM becomes

$$d_{f,\mathrm{Hg}} = 6.1 \times 10^{-28} \left(g_{10} - g_{50} \cdot 2.26 \times 10^{4}\right) \mathrm{e} \cdot \mathrm{cm}. \tag{40}$$

For this particular choice, the overall false EDM is smaller, and furthermore the g_{50} term is reduced relative to the g_{10} when compared to the usual ILL/PSI geometry.

5.3. Further notes

It is unclear whether this geometry would be realizable experimentally. The main point of the discussion is that the geometry affects the size of the g_{30} term for the Hg comagnetometer false EDM, and the closer to spherical the less the higher-order terms tend to contribute.

It is also important to consider the overall false-EDM correction scheme used in these experiments. While the false EDM of the mercury comagnetometer tends to dominate the correction, it is by no means the only quantity affected by the higher multipoles of the magnetic field. The neutrons' false EDM, the spin relaxation times of the species, and the electric field independent spin-precession frequencies are also affected by the inhomogeneity.

In particular, the spin-precession frequency ratio (neutrons to Hg) was used in the ILL nEDM experiment to sense the vertical gradient g_{10} and hence to correct the leading terms in the false EDM's [6, 7]. This works because

the ultracold neutrons tend to preferentially sample the bottom of the cell, resulting in an average height difference against gravity. When considered to higher order, other terms contribute to this correction scheme. So while the false EDM of the Hg atoms could be suppressed by a quasi-spherical cell, it is unclear that this is the most important factor in experiment design. Even if the EDM cell could be made spherical, the neutrons still preferentially sample the lower portion of the sphere.

6. Conclusion

We have demonstrated that a spherical EDM measurement cell would reduce the false EDM of Hg to depend on a single multipole of the magnetic field. A cylindrical cell that is quasi-spherical with $H = \sqrt{2}R$ also tends to reduce the higher multipole contributions. Both suggestions are rather difficult to realize experimentally, and do not capture the full correction scheme used in the ILL/PSI nEDM experiment, which must take more into account than simply the false EDM of the Hg comagnetometer. Nonetheless, we think this is an interesting result which points out the dependence of the false EDM contributions on the measurement cell geometry.

Acknowledgements

This work was undertaken, in part, thanks to funding from the Natural Sciences and Engineering Research Council Canada, the Canada Research Chairs program, and the Canada Foundation for Innovation. G.P. is supported by the ERC grant 716651-NEDM.

References

[1] K. Green, P. G. Harris, P. Iaydjiev, D. J. R. May, J. M. Pendlebury, K. F. Smith, M. van der Grinten, P. Geltenbort, S. Ivanov, Performance of an atomic mercury magnetometer in the neutron EDM experiment, Nucl. Instrum. Meth. A404 (1998) 381–393.

[2] C. A. Baker, et al., Apparatus for Measurement of the Electric Dipole Moment of the Neutron using a Cohabiting Atomic-Mercury Magnetometer, Nucl. Instrum. Meth. A736 (2014) 184–203.

[3] G. Ban, et al., Demonstration of sensitivity increase in mercury free-spin-precession magnetometers due to laser-based readout for neutron electric dipole moment searches, Nucl. Instrum. Meth. A896 (2018) 129–138.

[4] W. C. Griffith, M. D. Swallows, T. H. Loftus, M. V. Romalis, B. R. Heckel, E. N. Fortson, Improved Limit on the Permanent Electric Dipole Moment of Hg-199, Phys. Rev. Lett. 102 (2009) 101601.

[5] B. Graner, Y. Chen, E. G. Lindahl, B. R. Heckel, Reduced Limit on the Permanent Electric Dipole Moment of Hg199, Phys. Rev. Lett. 116 (2016) 161601. [Erratum: Phys. Rev. Lett.119,no.11,119901(2017)].

[6] C. A. Baker, et al., An Improved experimental limit on the electric dipole moment of the neutron, Phys. Rev. Lett. 97 (2006) 131801.

[7] J. M. Pendlebury, et al., Revised experimental upper limit on the electric dipole moment of the neutron, Phys. Rev. D92 (2015) 092003.

[8] J. M. Pendlebury, et al., Geometric-phase-induced false electric dipole moment signals for particles in traps, Phys. Rev. A70 (2004) 032102.

[9] P. G. Harris, J. M. Pendlebury, Dipole-field contributions to geometric-phase-induced false electric-dipole-moment signals for particles in traps, Phys. Rev. A73 (2006) 014101.

[10] S. K. Lamoreaux, R. Golub, Detailed discussion of a linear electric field frequency shift induced in confined gases by a magnetic field gradient: Implications for neutron electric-dipole-moment experiments, Phys. Rev. A71 (2005) 032104.

[11] A. L. Barabanov, R. Golub, S. K. Lamoreaux, Linear electric field frequency shift (important for next generation electric dipole moment searches) induced in confined gases by a magnetic field gradient, Phys. Rev. A74 (2006) 052115.

[12] G. Pignol, S. Roccia, Electric dipole moment searches: Reexamination of frequency shifts for particles in traps, Phys. Rev. A85 (2012) 042105.

[13] S. Afach, et al., Measurement of a false electric dipole moment signal from ^{199}Hg atoms exposed to an inhomogeneous magnetic field, Eur. Phys. J. D69 (2015) 225.

[14] S. Komposch, Realization of a high-performance laser-based mercury magnetometer for neutron EDM experiments, Ph.D. thesis, ETH Zürich, 2017.

[15] J. D. Jackson, Classical Electrodynamics, 2nd ed., Wiley, New York, NY, 1975.

[16] J. J. Sakurai, Modern Quantum Mechanics, rev. ed., Addison-Wesley, Reading, MA, 1994.

[17] C. Abel, et al., Magnetic field uniformity in neutron electric dipole moment experiments, arXiv:1811.06085 [physics.ins-det], 2018.

Bibliography

[1] C. Abel, S. Afach, N. J. Ayres, G. Ban, G. Bison, K. Bodek, V. Bondar, E. Chanel, P. J. Chiu, C. B. Crawford, Z. Chowdhuri, M. Daum, S. Emmenegger, L. Ferraris-Bouchez, M. Fertl, B. Franke, W. C. Griffith, Z. D. Grujić, L. Hayen, V. Hélaine, N. Hild, M. Kasprzak, Y. Kermaidic, K. Kirch, P. Knowles, H. C. Koch, S. Komposch, P. A. Koss, A. Kozela, J. Krempel, B. Lauss, T. Lefort, Y. Lemière, A. Leredde, A. Mtchedlishvili, P. Mohanmurthy, M. Musgrave, O. Naviliat-Cuncic, D. Pais, A. Pazgalev, F. M. Piegsa, E. Pierre, G. Pignol, P. N. Prashanth, G. Quéméner, M. Rawlik, D. Rebreyend, D. Ries, S. Roccia, D. Rozpedzik, P. Schmidt-Wellenburg, A. Schnabel, N. Severijns, R. Tavakoli Dinani, J. Thorne, A. Weis, E. Wursten, G. Wyszynski, J. Zejma, and G. Zsigmond. Optically pumped cs magnetometers enabling a high-sensitivity search for the neutron electric dipole moment, 2019.

[2] C. Abel, S. Afach, N. J. Ayres, G. Ban, G. Bison, K. Bodek, V. Bondar, E. Chanel, P. J. Chiu, C. B. Crawford, Z. Chowdhuri, M. Daum, S. Emmenegger, L. Ferraris-Bouchez, M. Fertl, B. Franke, W. C. Griffith, Z. D. Grujić, L. Hayen, V. Hélaine, N. Hild, M. Kasprzak, Y. Kermaidic, K. Kirch, P. Knowles, H. C. Koch, S. Komposch, P. A. Koss, A. Kozela, J. Krempel, B. Lauss, T. Lefort, Y. Lemière, A. Leredde, A. Mtchedlishvili, P. Mohanmurthy, M. Musgrave, O. Naviliat-Cuncic, D. Pais, A. Pazgalev, F. M. Piegsa, E. Pierre, G. Pignol, P. N. Prashanth, G. Quéméner, M. Rawlik, D. Rebreyend, D. Ries, S. Roccia, D. Rozpedzik, P. Schmidt-Wellenburg, A. Schnabel, N. Severijns, R. Tavakoli Dinani, J. Thorne, A. Weis, E. Wursten, G. Wyszynski, J. Zejma, and G. Zsigmond. Optically pumped cs magnetometers enabling a high-sensitivity search for the neutron electric dipole moment, 2019.

[3] C. Abel, N. J. Ayres, T. Baker, G. Ban, G. Bison, K. Bodek, V. Bondar, C. B. Crawford, P.-J. Chiu, E. Chanel, Z. Chowdhuri, M. Daum, B. Dechenaux, S. Emmenegger, L. Ferraris-Bouchez, P. Flaux, P. Geltenbort, K. Green, W. C. Griffith, M. van der Grinten, P. G. Harris, R. Henneck, N. Hild, P. Iaydjiev, S. N. Ivanov, M. Kasprzak, Y. Kermaidic, K. Kirch, H.-C. Koch, S. Komposch, P. A. Koss, A. Kozela, J. Krempel, B. Lauss, T. Lefort, Y. Lemiere, A. Leredde, P. Mohanmurthy, D. Pais, F. M. Piegsa, G. Pignol, G. Quéméner, M. Rawlik, D. Rebreyend, D. Ries, S. Roccia, D. Rozpedzik, P. Schmidt-Wellenburg, A. Schnabel, N. Severijns, R. Virot, A. Weis, E. Wursten, G. Wyszynski, J. Zejma, and G. Zsigmond. Magnetic-field uniformity in neutron electric-dipole-moment experiments. *Phys. Rev. A*, 99:042112, Apr 2019.

[4] S. Afach, C. A. Baker, G. Ban, G. Bison, K. Bodek, Z. Chowdhuri, M. Daum, M. Fertl, B. Franke, P. Geltenbort, K. Green, M. G. D. van der Grinten, Z. Grujic, P. G. Harris, W. Heil, V. Hélaine, R. Henneck, M. Horras, P. Iaydjiev, S. N. Ivanov, M. Kasprzak, Y. Kermaïdic, K. Kirch, P. Knowles, H.-C. Koch, S. Komposch, A. Kozela, J. Krempel, B. Lauss, T. Lefort, Y. Lemière, A. Mtchedlishvili, O. Naviliat-Cuncic, J. M. Pendlebury, F. M. Piegsa, G. Pignol, P. N. Prashant, G. Quéméner, D. Rebreyend, D. Ries, S. Roccia, P. Schmidt-Wellenburg, N. Severijns, A. Weis, E. Wursten, G. Wyszynski, J. Zejma, J. Zenner, and G. Zsigmond. Measurement of a false electric dipole moment signal from 199hg atoms exposed to an inhomogeneous magnetic field. *The European Physical Journal D*, 69(10):225, Oct 2015.

[5] Shomi Ahmed. Active magnetic compensation prototype for a neutron electric dipole moment experiment. Master's thesis, University of Manitoba, Department of Physics and Astronomy, June-August 2019.

[6] M. Auzinsh, D. Budker, and S. Rochester. *Optically Polarized Atoms: Understanding Light-atom Interactions*. OUP Oxford, 2010.

[7] C. A. Baker, D. D. Doyle, P. Geltenbort, K. Green, M. G. D. van der Grinten, P. G. Harris, P. Iaydjiev, S. N. Ivanov, D. J. R. May, J. M. Pendlebury, J. D. Richardson, D. Shiers, and K. F. Smith. Improved experimental limit on the electric dipole moment of the neutron. *Phys. Rev. Lett.*, 97:131801, Sep 2006.

[8] D. Budker and D.F.J. Kimball. *Optical Magnetometry*. Optical Magnetometry. Cambridge University Press, 2013.

[9] J. H. Christenson, J. W. Cronin, V. L. Fitch, and R. Turlay. Evidence for the 2π Decay of the K20 Meson. *Physical Review Letters*, 13:138–140, July 1964.

[10] Moushumi Das. Highly Sensitive Rb Magnetometer for Neutron Electric Dipole Moment Experiments. Master's thesis, University of Manitoba, Department of Physics and Astronomy, June-August 2019.

[11] Dawei Ding, Hongjin Wang, and Gang Wang. Evolutionary computation of multiband antenna using multi-objective evolutionary algorithm based on decomposition. In Baoxiang Liu and Chunlai Chai, editors, *Information Computing and Applications*, pages 383–390, Berlin, Heidelberg, 2011. Springer Berlin Heidelberg.

[12] M. Faraday, T. Martin, and Royal Institution of Great Britain. *Faraday's diary: being the various philosophical notes of experimental investigation made by Michael Faraday, during the years 1820-1862 and bequeathed by him to the Royal institution of Great Britain*. Faraday's Diary: Being the Various Philosophical Notes of Experimental Investigation. G. Bell and sons, ltd., 1933.

[13] Jason D. Fiege. *Qubist User's Guide: Optimization, Data-Modeling, and Visualization with the Qubist Global Optimization Toolbox for MATLAB*. nQube Technical Computing

Corporation, 75 Craigmohr Dr., Winnipeg, MB, Canada, R3T 6B9, first edition, March 2010.

[14] The Winnipeg Institute for Theoretical Physics. The winnipeg institute for theoretical physics annual report. `http://www2.physics.umanitoba.ca/u/witp/documents/witp13.pdf`, August 2013. Retrieved Nov 01 2019.

[15] Peter A. Fridman. Optimal array configuration search using genetic algorithm. In Andrew G. Tescher, editor, *Applications of Digital Image Processing XXIV*, volume 4472, pages 518 – 527. International Society for Optics and Photonics, SPIE, 2001.

[16] M. T. Graf, D. F. Kimball, S. M. Rochester, K. Kerner, C. Wong, D. Budker, E. B. Alexandrov, M. V. Balabas, and V. V. Yashchuk. Relaxation of atomic polarization in paraffin-coated cesium vapor cells. *Phys. Rev. A*, 72:023401, Aug 2005.

[17] Zoran D. Grujić, Peter A. Koss, Georg Bison, and Antoine Weis. A sensitive and accurate atomic magnetometer based on free spin precession. *The European Physical Journal D*, 69(5):135, May 2015.

[18] Greg Hornby, Al Globus, Derek Linden, and Jason Lohn. Automated antenna design with evolutionary algorithms. *Collection of Technical Papers - Space 2006 Conference*, 1, 09 2006.

[19] J.D. Jackson. *Classical electrodynamics*. Wiley, 1975.

[20] I.B. Khriplovich and S.K. Lamoreaux. *CP Violation Without Strangeness: Electric Dipole Moments of Particles, Atoms, and Molecules*. Theoretical and Mathematical Physics. Springer Berlin Heidelberg, 2012.

[21] Ken D. Kihm and Donald P. Lyons. Optical tomography using a genetic algorithm. *Opt. Lett.*, 21(17):1327–1329, Sep 1996.

[22] Jihn E. Kim and Gianpaolo Carosi. Axions and the strong *cp* problem. *Rev. Mod. Phys.*, 82:557–601, Mar 2010.

[23] W. Klassen, J.W. Martin, and G. Pignol. Wigner–eckart theorem and the false edm of 199hg. *Nuclear Instruments and Methods in Physics Research Section A: Accelerators, Spectrometers, Detectors and Associated Equipment*, 922:322 – 325, 2019.

[24] Makoto Kobayashi and Toshihide Maskawa. CP-Violation in the Renormalizable Theory of Weak Interaction. *Progress of Theoretical Physics*, 49(2):652–657, 02 1973.

[25] J.W. Martin, R.R. Mammei, W. Klassen, C. Cerasani, T. Andalib, C.P. Bidinosti, M. Lang, and D. Ostapchuk. Large magnetic shielding factor measured by nonlinear magneto-optical rotation. *Nuclear Instruments and Methods in Physics Research Section A: Accelerators, Spectrometers, Detectors and Associated Equipment*, 778:61 – 66, 2015.

[26] G. Moruzzi and F. Strumia. *The Hanle Effect and Level-Crossing Spectroscopy*. Physics of Atoms and Molecules. Springer US, 1992.

[27] J. M. Pendlebury, S. Afach, N. J. Ayres, C. A. Baker, G. Ban, G. Bison, K. Bodek, M. Burghoff, P. Geltenbort, K. Green, W. C. Griffith, M. van der Grinten, Z. D. Grujić, P. G. Harris, V. Hélaine, P. Iaydjiev, S. N. Ivanov, M. Kasprzak, Y. Kermaidic, K. Kirch, H.-C. Koch, S. Komposch, A. Kozela, J. Krempel, B. Lauss, T. Lefort, Y. Lemière, D. J. R. May, M. Musgrave, O. Naviliat-Cuncic, F. M. Piegsa, G. Pignol, P. N. Prashanth, G. Quéméner, M. Rawlik, D. Rebreyend, J. D. Richardson, D. Ries, S. Roccia, D. Rozpedzik, A. Schnabel, P. Schmidt-Wellenburg, N. Severijns, D. Shiers, J. A. Thorne, A. Weis, O. J. Winston, E. Wursten, J. Zejma, and G. Zsigmond. Revised experimental upper limit on the electric dipole moment of the neutron. *Phys. Rev. D*, 92:092003, Nov 2015.

[28] J. M. Pendlebury, W. Heil, Yu. Sobolev, P. G. Harris, J. D. Richardson, R. J. Baskin, D. D. Doyle, P. Geltenbort, K. Green, M. G. D. van der Grinten, P. S. Iaydjiev, S. N. Ivanov, D. J. R. May, and K. F. Smith. Geometric-phase-induced false electric dipole moment signals for particles in traps. *Phys. Rev. A*, 70:032102, Sep 2004.

[29] R. Penrose. On best approximate solutions of linear matrix equations. *Mathematical Proceedings of the Cambridge Philosophical Society*, 52(1):17–19, 1956.

[30] Guillaume Pignol and Stéphanie Roccia. Electric-dipole-moment searches: Reexamination of frequency shifts for particles in traps. *Phys. Rev. A*, 85:042105, Apr 2012.

[31] S. S. Raghuwanshi and G. M. Saxena. A generalized approach to determination of magnetic shielding factor for physics package of rb atomic clock, 2009.

[32] Andrei D Sakharov. Violation ofCPin variance,casymmetry, and baryon asymmetry of the universe. *Soviet Physics Uspekhi*, 34(5):392–393, may 1991.

[33] W.R. Smythe. *Static and Dynamic Electricity*. International series in pure and applied physics. McGraw-Hill, 1950.

[34] Igor I. Sobelman. *Atomic Spectra and Radiative Transitions*. Springer series on Atoms and Plasma. Springer, Berlin, Heidelberg, second edition, 1992.

[35] M. D. Swallows, T. H. Loftus, W. C. Griffith, B. R. Heckel, E. N. Fortson, and M. V. Romalis. Techniques used to search for a permanent electric dipole moment of the ^{199}hg atom and the implications for *CP* violation. *Phys. Rev. A*, 87:012102, Jan 2013.

[36] P. A. Vikhar. Evolutionary algorithms: A critical review and its future prospects. In *2016 International Conference on Global Trends in Signal Processing, Information Computing and Communication (ICGTSPICC)*, pages 261–265, Dec 2016.